

①

AFIT/GEO/ENP/93D-03

**AD-A273 884**



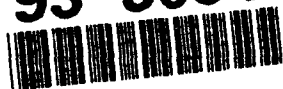
**DTIC**  
**S ELECTED D**  
E  
DEC 17 1993

**IMPROVED QUALITY OF RECONSTRUCTED  
IMAGES THROUGH SIFTING OF DATA IN  
STATISTICAL IMAGE RECONSTRUCTION**

**THESIS**  
**Craig A. Stoudt**  
**Captain, USAF**

AFIT/GEO/ENP/93D-03

**93-30517**



Approved for public release; distribution unlimited

**93 12 1 51 15**

**Best  
Available  
Copy**

AFIT/GEO/ENP/93D-03

IMPROVED QUALITY OF RECONSTRUCTED  
IMAGES THROUGH SIFTING OF DATA IN  
STATISTICAL IMAGE RECONSTRUCTION

THESIS

Presented to the Faculty of the School of Engineering  
of the Air Force Institute of Technology  
Air University  
In Partial Fulfillment of the  
Requirements for the Degree of  
Master of Science in Electrical Engineering

Craig A. Stoudt, B.S.E.E.  
Captain, USAF

December 1993

Approved for public release; distribution unlimited

## Preface

This thesis presents the results of an initial investigation into the feasibility of using frame selection as a post-processing technique for Air Force adaptive optics systems. The key result is a frame selection algorithm that can be immediately implemented at Air Force space surveillance sites to improve their mission effectiveness. I hope that this research effort will contribute to our nation's defense by enhancing the Air Force's space surveillance capabilities. Furthermore, I hope that this thesis will inspire future AFIT students to pursue research in this challenging and vital area.

I'd like to thank my faculty advisor, Captain Michael C. Roggeman, for his assistance and encouragement throughout this project. His enthusiasm and his keen interest in this subject area were constant sources of inspiration.

I'd also like to thank my thesis committee members, Dr. Byron M. Welsh, and Dr. Theodore E. Luke, for their many suggestions and comments, which greatly contributed to the quality of this thesis.

Finally, I'd like to thank my fellow AFIT students. Their irreverent sense of humor is the part of my AFIT experience that I will cherish the most.

Craig A. Stoudt

**DTIC QUALITY INSPECTED 1**

Accession For	
NTIS CRA&I	<input checked="" type="checkbox"/>
DTIC TAB	<input type="checkbox"/>
Unannounced	<input type="checkbox"/>
Justification .....	
By .....	
Distribution /	
Availability Codes	
Dist	Avail and/or Special
A-1	

## *Table of Contents*

	Page
Preface . . . . .	ii
List of Figures . . . . .	vii
List of Tables . . . . .	xii
Abstract . . . . .	xiii
I. Introduction . . . . .	1-1
1.1 Motivation . . . . .	1-1
1.2 Problem Statement . . . . .	1-2
1.3 Approach . . . . .	1-2
1.4 Scope . . . . .	1-3
1.5 Chapter Outlines . . . . .	1-4
1.5.1 Chapter 2 . . . . .	1-4
1.5.2 Chapter 3 . . . . .	1-4
1.5.3 Chapter 4 . . . . .	1-5
1.5.4 Chapter 5 . . . . .	1-5
1.5.5 Appendix A . . . . .	1-5
1.5.6 Appendix B . . . . .	1-5
1.6 Summary of Key Results . . . . .	1-5
1.7 Conclusion . . . . .	1-6
II. Background . . . . .	2-1
2.1 Introduction . . . . .	2-1
2.2 Atmospheric Turbulence . . . . .	2-1

	Page
2.3 Adaptive Optics . . . . .	2-2
2.4 Frame Selection . . . . .	2-3
2.4.1 Effects of Exposure Time on Image Resolution	2-4
2.4.2 Statistics of Image Quality . . . . .	2-5
2.4.3 Strehl Ratio and the Marechal Approximation	2-7
2.4.4 Improved Image Quality Through Frame Selection . . . . .	2-9
2.4.5 Quality Metrics for Frame Selection . . . . .	2-9
2.4.6 Frame Selection Implementations . . . . .	2-12
2.5 Limits of Current Knowledge . . . . .	2-13
2.6 Summary . . . . .	2-14
 III. Methodology . . . . .	 3-1
3.1 Introduction . . . . .	3-1
3.2 Terminology . . . . .	3-2
3.3 Sharpness Functions as Quality Metrics . . . . .	3-3
3.3.1 A New Quality Metric . . . . .	3-3
3.4 Computer Simulation of the Problem . . . . .	3-5
3.5 Statistical Definitions . . . . .	3-7
3.5.1 Image Spectrum Signal to Noise Ratio (SNR)	3-7
3.5.2 Improved SNR through Averaging . . . . .	3-7
3.6 SNR Performance Metrics . . . . .	3-8
3.6.1 Radially Averaged SNR . . . . .	3-8
3.6.2 Noise Equivalent Frequency Cutoff . . . . .	3-8
3.6.3 SNR Gain . . . . .	3-9
3.6.4 Integrated Gain . . . . .	3-9
3.7 Independent Variables . . . . .	3-10
3.7.1 Number of Short Exposure Images, $N$ , $M$ . .	3-11

	Page
3.7.2 Average Photo events, $K$ . . . . .	3-11
3.7.3 $E_{SE} [H(u, v)]$ and $var [H(u, v)]$ . . . . .	3-12
3.7.4 Object Spectrum . . . . .	3-12
3.7.5 CCD Camera Noise . . . . .	3-13
3.8 Summary . . . . .	3-13
IV. Analysis Results . . . . .	4-1
4.1 Introduction . . . . .	4-1
4.1.1 System Parameters . . . . .	4-2
4.2 Experiment One . . . . .	4-3
4.2.1 Simulation Parameters . . . . .	4-3
4.2.2 Statistical Implications . . . . .	4-3
4.2.3 Frame Selection and Image SNR . . . . .	4-5
4.2.4 Signal to Noise Ratio and Image Resolution . . . . .	4-7
4.2.5 Quality Metric Performance . . . . .	4-8
4.2.6 Conclusions . . . . .	4-9
4.3 Experiment Two . . . . .	4-23
4.3.1 Simulation Parameters . . . . .	4-23
4.3.2 Simulation Results . . . . .	4-23
4.3.3 Quality Metric Performance . . . . .	4-25
4.3.4 Conclusions . . . . .	4-25
4.4 Experiment Three . . . . .	4-32
4.4.1 Simulation Parameters . . . . .	4-32
4.4.2 Quality Metric Performance . . . . .	4-33
4.4.3 Conclusions . . . . .	4-34
4.5 Experiment Four . . . . .	4-42
4.5.1 Simulation Parameters . . . . .	4-42
4.5.2 Simulation Results . . . . .	4-42

	Page
4.5.3 Conclusions . . . . .	4-43
4.6 Experiment Five . . . . .	4-52
4.6.1 Simulation Parameters . . . . .	4-52
4.6.2 Simulation Results . . . . .	4-52
4.6.3 Quality Metric Performance . . . . .	4-52
4.6.4 Conclusions . . . . .	4-52
4.7 Summary . . . . .	4-58
 V. Conclusions and Recommendations . . . . .	 5-1
5.1 Introduction . . . . .	5-1
5.2 Conclusions . . . . .	5-1
5.3 Recommendations to the User . . . . .	5-2
5.4 Recommendations for Further Research . . . . .	5-3
 Appendix A. CCD Camera Model . . . . .	 A-1
A.1 Introduction . . . . .	A-1
A.2 Pixel Array Size . . . . .	A-1
A.3 Sample Noise Variance . . . . .	A-3
A.4 Model Validation . . . . .	A-4
 Appendix B. Simulation Results . . . . .	 B-1
B.1 Experiment One . . . . .	B-1
B.2 Experiment Two . . . . .	B-5
B.3 Experiment Three . . . . .	B-8
B.4 Experiment Four . . . . .	B-15
B.5 Experiment Five . . . . .	B-21
 Bibliography . . . . .	 BIB-1
 Vita . . . . .	 VITA-1

## List of Figures

Figure		Page
4.1.	Mean Image Spectrum vs Frequency, Point Source, $m_v=-1$ , $r_o=10\text{cm}$	4-11
4.2.	Fidelity Defect vs Selection Rate, Point Source, $m_v=-1$ , $r_o=10\text{cm}$	4-12
4.3.	Strehl Ratio vs Selection Rate, Point Source, $m_v=-1$ , $r_o=10\text{cm}$	4-13
4.4.	Point Spread Function, Point Source, $m_v=-1$ , $r_o=10\text{cm}$	4-14
4.5.	Image Spectrum Variance vs Frequency, Point Source, $m_v=-1$ , $r_o=10\text{cm}$	4-15
4.6.	$\eta$ vs Selection Rate, Point Source, $m_v=-1$ , $r_o=10\text{cm}$	4-16
4.7.	$A_G$ vs Selection Rate, Point Source, $m_v=-1$ , $r_o=10\text{cm}$	4-17
4.8.	Gain Curves, 60%, 25%, 10% Selection Rates, Point Source, $m_v=-1$ , $r_o=10\text{cm}$	4-18
4.9.	$\eta$ vs Selection Rate, Different Quality Metrics, Point Source, $m_v=-1$ , $r_o=10\text{cm}$	4-19
4.10.	$A_G$ vs Selection Rate, Different Quality Metrics, Point Source, $m_v=-1$ , $r_o=10\text{cm}$	4-20
4.11.	Gain Curves for $S_{S1}$ , Point Source, $m_v=-1$ , $r_o=10\text{cm}$	4-21
4.12.	Comparison of Gain Curves, 75% Selection Rate, Point Source, $m_v=-1$ , $r_o=10\text{cm}$	4-22
4.13.	Typical Space Object	4-26
4.14.	$\eta$ vs Selection Rate, Extended Object and Point Source, $m_v=-1$ , $r_o=10\text{cm}$	4-27
4.15.	$A_G$ vs Selection Rate, Extended Object and Point Source, $m_v=-1$ , $r_o=10\text{cm}$	4-28
4.16.	Object Spectrum and Average OTF, $m_v=-1$ , $r_o=10\text{cm}$	4-29
4.17.	Gain Curves, Extended Object, $m_v=-1$ , $r_o=10\text{cm}$	4-30
4.18.	Comparison of Gain Curves, Extended Object, $m_v=-1$ , $r_o=10\text{cm}$	4-31
4.19.	$\eta$ vs Selection Rate for Different Seeing Conditions, Extended Object, $m_v=-1$	4-35

Figure	Page
4.20. $A_G$ vs Selection Rate for Different Seeing Conditions, Extended Object, $m_v=-1$ . . . . .	4-36
4.21. Gain Curves for Extended Object, $r_o=7\text{cm}$ , $m_v=-1$ . . . . .	4-37
4.22. Gain Curves for Extended Object, $r_o=13\text{cm}$ , $m_v=-1$ . . . . .	4-38
4.23. SNR at 40% Selection Rate for Different Seeing Conditions, Extended Object, $m_v=-1$ . . . . .	4-39
4.24. Comparison of Gain Curves at 60% Frame Selection Rate, Extended Object, $m_v=-1$ , $r_o=7\text{cm}$ . . . . .	4-40
4.25. Comparison of Gain Curves at 80% Frame Selection Rate, Extended Object, $m_v=-1$ , $r_o=13\text{cm}$ . . . . .	4-41
4.26. $\eta$ vs Frequency, Point Source, $m_v=-1,+3$ , $r_o=10\text{cm}$ . . . . .	4-45
4.27. $A_G$ vs Frequency, Point Source, $m_v =-1,+3$ , $r_o=10\text{cm}$ . . . . .	4-46
4.28. Gain Curves, Point Source, $m_v=+3$ , $r_o=10\text{cm}$ . . . . .	4-47
4.29. $\eta$ vs Selection Rate, Extended Object, $m_v=-1,+3$ , $r_o=10\text{cm}$ . . . . .	4-48
4.30. $A_G$ vs Selection Rate, Extended Object, $m_v=-1,+3$ , $r_o=10\text{cm}$ . . . . .	4-49
4.31. Gain Curves, Extended Object, $m_v=-1,+3$ , $r_o=10\text{cm}$ . . . . .	4-50
4.32. $A_G$ vs $m_v$ , Extended Object, $r_o=10\text{cm}$ . . . . .	4-51
4.33. $\eta$ vs Frequency, CCD Noise Case, Point Source, $m_v=+3$ , $r_o=10\text{cm}$ . . . . .	4-54
4.34. $A_G$ vs Frequency, CCD Noise Case, Point Source, $m_v=+3$ , $r_o=10\text{cm}$ . . . . .	4-55
4.35. Gain Curves, CCD Noise Case, Point Source, $m_v=+3$ , $r_o=10\text{cm}$ . . . . .	4-56
4.36. Comparison of Gain Curves, CCD Noise Case, Point Source, $m_v=+3$ , $r_o=10\text{cm}$ . . . . .	4-57
A.1. Comparison of Theoretical and Simulation Results, CCD Camera Model . . . . .	A-5
B.1. Gain Curves, Experiment 1: Point source, $r_o = 10\text{cm}$ , $m_v = -1$ , Photon limited, Selection rate = 90% . . . . .	B-2
B.2. Gain Curves, Experiment 1: Point source, $r_o = 10\text{cm}$ , $m_v = -1$ , Photon limited, Selection rate = 80% . . . . .	B-2

Figure	Page
B.3. Gain Curves, Experiment 1: Point source, $r_o = 10\text{cm}$ , $m_v = -1$ , Photon limited, Selection rate = 70% . . . . .	B-3
B.4. Gain Curves, Experiment 1: Point source, $r_o = 10\text{cm}$ , $m_v = -1$ , Photon limited, Selection rate = 60% . . . . .	B-3
B.5. Gain Curves, Experiment 1: Point source, $r_o = 10\text{cm}$ , $m_v = -1$ , Photon limited, Selection rate = 40% . . . . .	B-4
B.6. Gain Curves, Experiment 1: Point source, $r_o = 10\text{cm}$ , $m_v = -1$ , Photon Limited, Selection rate = 20% . . . . .	B-4
B.7. Gain Curves, Experiment 2: Extended object, $r_o = 10\text{cm}$ , $m_v =$ $-1$ , Photon limited, Selection rate = 90% . . . . .	B-5
B.8. Gain Curves, Experiment 2: Extended object, $r_o = 10\text{cm}$ , $m_v =$ $-1$ , Photon limited, Selection rate = 80% . . . . .	B-6
B.9. Gain Curves, Experiment 2: Extended object, $r_o = 10\text{cm}$ , $m_v =$ $-1$ , Photon limited, Selection rate = 70% . . . . .	B-6
B.10. Gain Curves, Experiment 2: Extended object, $r_o = 10\text{cm}$ , $m_v =$ $-1$ , Photon limited, Selection rate = 60% . . . . .	B-7
B.11. Gain Curves, Experiment 2: Extended object, $r_o = 10\text{cm}$ , $m_v =$ $-1$ , Photon limited, Selection rate = 40% . . . . .	B-7
B.12. Gain Curves, Experiment 2: Extended object, $r_o = 10\text{cm}$ , $m_v =$ $-1$ , Photon limited, Selection rate = 20% . . . . .	B-8
B.13. Gain Curves, Experiment 3: Extended object, $r_o = 7\text{cm}$ , $m_v = -1$ , Photon limited, Selection rate = 90% . . . . .	B-9
B.14. Gain Curves, Experiment 3: Extended object, $r_o = 7\text{cm}$ , $m_v = -1$ , Photon limited, Selection rate = 80% . . . . .	B-9
B.15. Gain Curves, Experiment 3: Extended object, $r_o = 7\text{cm}$ , $m_v = -1$ , Photon limited, Selection rate = 70% . . . . .	B-10
B.16. Gain Curves, Experiment 3: Extended object, $r_o = 7\text{cm}$ , $m_v = -1$ , Photon limited, Selection rate = 60% . . . . .	B-10
B.17. Gain Curves, Experiment 3: Extended object, $r_o = 7\text{cm}$ , $m_v = -1$ , Photon limited, Selection rate = 40% . . . . .	B-11

Figure	Page
B.18. Gain Curves, Experiment 3: Extended object, $r_o = 7\text{cm}$ , $m_v = -1$ , Photon limited, Selection rate = 20% . . . . .	B-11
B.19. Gain Curves, Experiment 3: Extended object, $r_o = 13\text{cm}$ , $m_v =$ $-1$ , Photon limited, Selection rate = 90% . . . . .	B-12
B.20. Gain Curves, Experiment 3: Extended object, $r_o = 13\text{cm}$ , $m_v =$ $-1$ , Photon limited, Selection rate = 80% . . . . .	B-12
B.21. Gain Curves, Experiment 3: Extended object, $r_o = 13\text{cm}$ , $m_v =$ $-1$ , Photon limited, Selection rate = 70% . . . . .	B-13
B.22. Gain Curves, Experiment 3: Extended object, $r_o = 13\text{cm}$ , $m_v =$ $-1$ , Photon limited, Selection rate = 60% . . . . .	B-13
B.23. Gain Curves, Experiment 3: Extended object, $r_o = 13\text{cm}$ , $m_v =$ $-1$ , Photon limited, Selection rate = 40% . . . . .	B-14
B.24. Gain Curves, Experiment 3: Extended object, $r_o = 13\text{cm}$ , $m_v =$ $-1$ , Photon limited, Selection rate = 20% . . . . .	B-14
B.25. Gain Curves, Experiment 4: Point source, $r_o = 10\text{cm}$ , $m_v = +3$ , Photon limited, Selection rate = 90% . . . . .	B-15
B.26. Gain Curves, Experiment 4: Point source, $r_o = 10\text{cm}$ , $m_v = +3$ , Photon limited, Selection rate = 80% . . . . .	B-16
B.27. Gain Curves, Experiment 4: Point source, $r_o = 10\text{cm}$ , $m_v = +3$ , Photon limited, Selection rate = 70% . . . . .	B-16
B.28. Gain Curves, Experiment 4: Point source, $r_o = 10\text{cm}$ , $m_v = +3$ , Photon limited, Selection rate = 60% . . . . .	B-17
B.29. Gain Curves, Experiment 4: Point source, $r_o = 10\text{cm}$ , $m_v = +3$ , Photon limited, Selection rate = 40% . . . . .	B-17
B.30. Gain Curves, Experiment 4: Point source, $r_o = 10\text{cm}$ , $m_v = +3$ , Photon limited, Selection rate = 20% . . . . .	B-18
B.31. Gain Curves, Experiment 4: Extended object, $r_o = 10\text{cm}$ , $m_v =$ $+3$ , Photon limited, Selection rate = 90% . . . . .	B-18
B.32. Gain Curves, Experiment 4: Extended object, $r_o = 10\text{cm}$ , $m_v =$ $+3$ , Photon limited, Selection rate = 80% . . . . .	B-19

Figure	Page
B.33. Gain Curves, Experiment 4: Extended object, $r_o = 10\text{cm}$ , $m_v = +3$ , Photon limited, Selection rate = 70% . . . . .	B-19
B.34. Gain Curves, Experiment 4: Extended object, $r_o = 10\text{cm}$ , $m_v = +3$ , Photon limited, Selection rate = 60% . . . . .	B-20
B.35. Gain Curves, Experiment 4: Extended object, $r_o = 10\text{cm}$ , $m_v = +3$ , Photon limited, Selection rate = 40% . . . . .	B-20
B.36. Gain Curves, Experiment 4: Extended object, $r_o = 10\text{cm}$ , $m_v = +3$ , Photon limited, Selection rate = 20% . . . . .	B-21
B.37. Gain Curves, Experiment 5: Point source, $r_o = 10\text{cm}$ , $m_v = +3$ , $\sigma^2 = 15$ , Selection rate = 90% . . . . .	B-22
B.38. Gain Curves, Experiment 5: Point source, $r_o = 10\text{cm}$ , $m_v = +3$ , $\sigma^2 = 15$ , Selection rate = 80% . . . . .	B-22
B.39. Gain Curves, Experiment 5: Point source, $r_o = 10\text{cm}$ , $m_v = +3$ , $\sigma^2 = 15$ , Selection rate = 70% . . . . .	B-23
B.40. Gain Curves, Experiment 5: Point source, $r_o = 10\text{cm}$ , $m_v = +3$ , $\sigma^2 = 15$ , Selection rate = 60% . . . . .	B-23
B.41. Gain Curves, Experiment 5: Point source, $r_o = 10\text{cm}$ , $m_v = +3$ , $\sigma^2 = 15$ , Selection rate = 20% . . . . .	B-24
B.42. Gain Curves, Experiment 5: Point source, $r_o = 10\text{cm}$ , $m_v = +3$ , $\sigma^2 = 30$ , Selection rate = 90% . . . . .	B-24
B.43. Gain Curves, Experiment 5: Point source, $r_o = 10\text{cm}$ , $m_v = +3$ , $\sigma^2 = 30$ , Selection rate = 80% . . . . .	B-25
B.44. Gain Curves, Experiment 5: Point source, $r_o = 10\text{cm}$ , $m_v = +3$ , $\sigma^2 = 30$ , Selection rate = 70% . . . . .	B-25
B.45. Gain Curves, Experiment 5: Point source, $r_o = 10\text{cm}$ , $m_v = +3$ , $\sigma^2 = 30$ , Selection rate = 60% . . . . .	B-26
B.46. Gain Curves, Experiment 5: Point source, $r_o = 10\text{cm}$ , $m_v = +3$ , $\sigma^2 = 30$ , Selection rate = 40% . . . . .	B-26
B.47. Gain Curves, Experiment 5: Point source, $r_o = 10\text{cm}$ , $m_v = +3$ , $\sigma^2 = 30$ , Selection rate = 20% . . . . .	B-27

*List of Tables*

Table	<i>List of Tables</i>	Page
3.1.	Visual Magnitude and Photo events for Common Sky Objects .	3-12

*Abstract*

The U.S. Air Force employs adaptive optics systems to produce images of exo-atmospheric objects. Such systems employ wavefront sensing systems and deformable mirrors to correct the aberrations induced by atmospheric turbulence. The images measured by an adaptive optics system are much better than images collected by conventional imaging systems, however, adaptive optics systems are unable to completely compensate for the effects of atmospheric turbulence, so post-processing techniques are employed to improve image quality. Typically, a large set of short exposure images are collected, re-centered to compensate for random image motion, averaged together to improve the signal to noise ratio, and then processed to form a reconstructed image. It is known that some short exposure images will be better than others, so some researchers have suggested that image quality can be improved by selecting a subset of the short exposure images according to some quality criterion, and then processing the average of this subset to form a single, high quality image. This thesis investigates the statistical implications of using frame selection as a post-processing technique to enhance images of exo-atmospheric objects measured by Air Force adaptive optics systems. Through computer simulation, the performance of frame selection in terms of signal to noise ratio in response to changes in atmospheric seeing conditions, image intensity levels, and detector noise is investigated. The results demonstrate that frame selection narrows the optical system point spread function, which reduces image blurring, and increases the accuracy of the image estimate and decreases the variance of that estimate, resulting in an increase in frequency spectrum signal to noise ratio, particularly in the mid-frequency range. For extended objects, the technique is light level dependent: for a 1 meter adaptive optics telescope, frame selection will yield an increase in signal to noise ratio for objects brighter than visual magnitude +2.3.

# IMPROVED QUALITY OF RECONSTRUCTED IMAGES THROUGH SIFTING OF DATA IN STATISTICAL IMAGE RECONSTRUCTION

## *I. Introduction*

### *1.1 Motivation*

Since the earliest days of the telescope, astronomers have realized that atmospheric turbulence imposes a severe limit on our ability to observe the universe beyond the confines of planet Earth. As early as 1704 Isaac Newton surmised that the magnified images he observed through his handmade telescope were severely degraded by what he termed "tremors" in the atmosphere [27]. For many years this problem only concerned lonely astronomers toiling on remote mountain peaks. However, after the Soviet Union's surprise launch of the Sputnik satellite in 1957, space surveillance became a critical component of our national defense strategy. As the ability to launch satellites into orbit comes within the reach of many Third World nations, our ability to quickly and accurately ascertain a potential adversary's space order of battle becomes crucial.

The Air Force Maui Optical Station (AMOS) is one of the US Air Force's space surveillance sites [1]. AMOS uses a 1.6 meter telescope to obtain high resolution images of space objects. This telescope uses an adaptive optics system to partially compensate for the effects of atmospheric turbulence. However, the adaptive optics system cannot fully correct turbulence-induced aberrations, so AMOS also uses image reconstruction processing to improve image quality. The reconstruction process produces images which have vastly better resolution than raw images, however, the reconstruction process also introduces artifacts.

The AMOS system collects a large set of short exposure images to "freeze" the effects of atmospheric turbulence. The short exposure images are re-centered to compensate for random image motion, and then the entire set is averaged to improve the signal to noise ratio. Reconstruction processing, such as inverse filtering [37], or bispectrum processing [35], is then performed on the output of the averaging process to produce a single, high quality image. The image reconstruction process is purely statistical in nature - that is, the underlying statistical behavior of the random process governing image formation determines the limits of performance for the technique. Experience has shown that some short exposure images are much better than others. The question is then: "Is there some means to select the best members of the set - or exclude the worst members - to improve the quality of the reconstructed image?"

### *1.2 Problem Statement*

This thesis develops a means to automatically determine which members of a large set of measured images are the best to use in the image reconstruction process, and then evaluates the degree of improvement in the reconstructed images.

### *1.3 Approach*

This thesis attacks the problem statement by investigating the statistical implications of applying a frame selection rule to a set of measured images. Specifically, this thesis investigates how the application of a frame selection rule changes the underlying statistics of a set of images, quantifies those changes, and then relates those changes to overall image quality. To achieve this goal, the following research questions are addressed:

1. Does there exist a subset of the short exposure images which yields a superior image compared to the entire set?
2. Which selection rules can be employed to identify a suitable subset?

3. How do the statistics of a subset identified by a frame selection rule differ from the statistics of the entire set?

4. What are the relevant optical parameters which affect the statistics of a large set of images collected by an adaptive optics system?

5. How do changes in subset statistic relate to overall image quality?

6. Which metrics can be employed to evaluate and compare the changes in subset statistics?

7. Is it possible to implement a frame selection rule in an operational setting?

This research effort employs computer simulation as the primary research tool in this investigation. Michael C. Roggeman has developed and provided a software simulation package known HYSIM [36]. The HYSIM simulation code models the effects of atmospheric turbulence as a series of random phase screens, and contains models for each component of an adaptive optics imaging system. To provide a more realistic assessment of the performance of an adaptive optics system in an operational setting, this research effort develops a charge-coupled device (CCD) camera model to account for the effects of detector noise. Frame selection rules are implemented in FORTRAN and incorporated into the existing simulation code. Also, the simulation code will be modified to calculate the statistics of the subsets identified by the frame selection rules.

#### *1.4 Scope*

This thesis analyzes the performance of frame selection rules employed as a post-processing technique for an adaptive optics system. The primary parameters are the adaptive optics system configuration, the atmospheric seeing conditions, the specific frame selection rule employed, and the frame selection rate expressed as a percentage of the entire set of short exposure images. As a final product, this thesis will contrast image quality between post-processed images produced from subsets

identified by specific frame selection rules and the image produced from the entire set. The performance metrics to be used in this comparison will be developed in chapter 3.

This thesis focuses on image processing techniques. Specifically, this thesis addresses the post-processing of a large set of short exposure images collected by an adaptive optics system similar to the one at the AMOS site. This thesis does not address the design of such an adaptive optics system. Optical design issues - such as the properties of optical materials - are not addressed. This thesis specifically addresses the post-processing of short exposure images. Real time processing considerations are not addressed.

### *1.5 Chapter Outlines*

The following is a brief synopsis of the information found in each chapter of the thesis.

*1.5.1 Chapter 2.* This chapter presents a brief overview of the problem of atmospheric turbulence, the use of adaptive optics to compensate for the effects of atmospheric turbulence, and the limitations of adaptive optics systems. The theory of frame selection - a technique developed by astronomers to improve the quality of images degraded by atmospheric turbulence - is described in detail. The concepts presented in this chapter provide a framework for the methodology developed in chapter 3.

*1.5.2 Chapter 3.* This chapter develops a detailed methodology for conducting the investigation, based on the background knowledge presented in Chapter 2. Basic terminology is defined, an approach based on computer simulation is justified, and specific performance metrics for evaluating changes in subset statistics are developed.

*1.5.3 Chapter 4.* This chapter presents the results five simulation experiments designed to explore the implications of frame selection. The experiments and the results are discussed in detail.

*1.5.4 Chapter 5.* This chapter states the conclusions based upon the results presented in chapter 4. Chapter 5 concludes with recommendations to the user concerning the implementation of frame selection, and recommendations for areas of future inquiry.

*1.5.5 Appendix A.* This appendix describes the implementation of the CCD camera model.

*1.5.6 Appendix B.* This appendix contains plots of the data collected in the experiment.

## *1.6 Summary of Key Results*

This investigation demonstrates that frame selection has two primary effects on image quality. First, frame selection narrows the optical system point spread function, which results in less image blurring. Second, frame selection increases the accuracy of the image estimate and decreases the variance of that estimate, resulting in an increase in frequency spectrum signal to noise ratio, particularly in the mid-frequency range. The point spread function steadily becomes narrower as a function of the frame selection rate, however, the signal to noise ratio reaches a peak - typically at a selection rate of 60-75%, and then decreases. Thus, there is a trade-off between image blurring and signal to noise ratio at low selection rates. For extended objects, the technique is light level dependent: for a 1 meter adaptive optics telescope, frame selection will yield an increase in signal to noise ratio for objects brighter than visual magnitude +2.3.

### *1.7 Conclusion*

Atmospheric turbulence presents a major obstacle to the Air Force's space surveillance mission. Adaptive optics systems are incapable of fully compensating for the effects of turbulence, so additional post-processing techniques are required to improve image quality. The next chapter presents a detailed discussion of the problem, and a solution based on frame selection.

## *II. Background*

### *2.1 Introduction*

This chapter provides the background necessary to understand the fundamental problem of atmospheric turbulence, its effect on Air Force adaptive optics systems, and the need for post-processing techniques to improve image quality. The theory and history of frame selection - the post-processing technique this thesis investigates - is presented in detail.

### *2.2 Atmospheric Turbulence*

Atmospheric turbulence is the major source of image degradation in a ground-based optical system. According to the "turbulent eddy" model, this degradation is due to random inhomogeneities in the refractive index of air [13]. This phenomenon is the result of differential heating of the Earth's surface, which results in large scale temperature inhomogeneities. Convection and turbulent wind flow break up these large scale inhomogeneities into smaller scale "eddies". Each turbulent eddy has its own individual refractive index, which temporally and spatially modulates the amplitude and phase of a propagating wavefront. Amplitude modulation results in scintillation or the twinkling of stars. Phase modulation results in random image motion (tilt) and phase aberration. For the case of ground-based imaging of exo-atmospheric objects, the effects of phase modulation are generally more severe than amplitude modulation [7].

Astronomers and others concerned with the propagation of light waves through turbulence have developed various parameters for characterizing the severity of image degradation due to turbulence. Astronomers typically use such parameters to compare the relative seeing quality of candidate sites for new observatories. One of the most convenient and widely used measures of seeing quality was introduced by Fried [8] and is denoted  $r_0$ . It is defined as the effective diameter of a telescope for

which the integral of the telescope's optical transfer function is equal to the ensemble averaged atmospheric optical transfer function [33].  $r_o$  is a function of the zenith angle of the path of propagation, the wavelength, and the effects of turbulence on optical propagation [33]. Since the effects of turbulence on optical propagation are random in nature,  $r_o$  is also random. Typical values for  $r_o$  at a good observatory range from 5cm for moderately poor seeing to 20cm for exceptional seeing [13]. In addition to its practical use as a measure of relative seeing quality,  $r_o$  is widely used in expressions for the atmospheric optical transfer function to simplify the forms of these expressions, and to aid in understanding their behavior [13].

Over the past three decades, numerous techniques for compensating the effects of atmospheric turbulence have been proposed. These techniques can be divided into two broad categories: pre-detection techniques where wavefront aberrations are sensed and canceled in real time, and post-detection techniques where an estimate of the object is recovered by processing a large number of frames of the distorted image. The former category encompasses the field of adaptive optics [14], while the latter encompasses techniques such as speckle imaging [19], bispectrum imaging [21], and frame selection [33]. Pre-detection and post-detection techniques are not mutually exclusive: hybrid techniques where pre-detection compensation is combined with post-detection bispectrum image processing have been reported [35]. This thesis represents the first investigation into the feasibility of combining pre-detection compensation with a post-detection processing technique known as frame selection. The following sections present a brief overview of adaptive optics systems, followed by a detailed examination of the frame selection technique.

### *2.3 Adaptive Optics*

Adaptive optics systems provide real-time compensation for the effects of random phase modulation. To accomplish this, the adaptive optics system must sense, reconstruct, and compensate for phase aberrations [14]. Wavefront sensing is accom-

plished by sampling the incoming wavefront at intervals known as subapertures, and then detecting the localized slope deviation of the incoming wavefront. Wavefront reconstruction is accomplished by combining the slope deviation measurements in such a way as to yield an estimate of the aberrations across the optical entrance pupil. Compensation is accomplished by applying an estimate of the conjugate of the wavefront phase aberration with a device known as a deformable mirror.

The fundamental limitations of an adaptive optics system are the accuracy of the wavefront sensors, the finite number of wavefront sensors employed across the wavefront surface, the finite number of degrees of freedom in the deformable mirror's response, and the finite system response time [40]. Photon noise imposes a fundamental limit on the accuracy of the wavefront sensors. At low light levels, shot noise and measurement noise effects in the wavefront sensor impose an additional limitation on sensor accuracy and seriously degrade the reconstruction process. The finite number of sensors employed by an adaptive optics system also limits the accuracy of the wavefront measurement. The finite number of degrees of freedom in the deformable mirror limits the device's response, which means that it cannot correct higher-order wavefront aberrations. The rapidity of fluctuations in phase aberrations - and control system stability requirements - demand that the reconstruction computations be performed at a rate of approximately one frame per millisecond. Because of these limitations, residual phase errors exist in the wavefront propagating from the deformable mirror, and these phase errors degrade the resulting image by scattering a fraction of the incident power through various random angles [39]. Hence, adaptive optics systems are incapable of fully compensating for phase aberrations, and post-processing techniques are needed to produce high quality images.

#### *2.4 Frame Selection*

Frame selection is a processing technique where image quality is improved by collecting a large set of short exposure images, selecting a subset of these images

according to some quality criterion, re-centering each image in this subset to compensate for the effects of random image motion, and then averaging the members of the re-centered subset to extract an estimate of the object [33]. Research into the effects of image exposure time on resolution, and the statistics of image quality provide the theoretical basis for the technique. To select the correct frames for processing, the technique requires a quality metric that is accurate and easy to compute. This section concludes with a discussion of several successful implementations of frame selection reported in the literature.

*2.4.1 Effects of Exposure Time on Image Resolution.* In 1966 Fried [8] developed expressions for the atmospheric optical transfer function for both short and long exposure images. Fried found that in the long exposure case, random image motion (tilt) smears the image observed in the image plane. As a result, tilt broadens the point spread function and narrows the optical transfer function in the long exposure case. However, for a sufficiently short exposure time (10 milliseconds or less), Fried found that tilt had a negligible effect on image quality. When comparing a series of short exposure images taken in succession, the image would appear to randomly move about the image plane from one exposure to the next, but smearing due to image shift would be negligible. Since it is a simple matter to re-center an image, the effects of tilt can be eliminated in post-processing. However, image degradation due to phase aberration still remains. Fried then compared the performance of an optical system for both the short and long exposure cases in terms of the performance metric  $\mathcal{R}$ , defined as:

$$\mathcal{R} = \int \tau(f) df \quad (2.1)$$

where  $\tau$  is the combined optical transfer function of the atmosphere and telescope, and  $f$  is a spatial frequency.  $\mathcal{R}$  is analogous to the bandwidth of an electrical system, and is sometimes referred to as optical resolution. For the long exposure case,  $\mathcal{R}$

approaches a limit determined by the diffraction limit of the aperture when the telescope diameter  $D$  is much less than the parameter  $r_o$ , and approaches a limit identical to the diffraction-limited performance of a telescope with diameter  $r_o$  when  $r_o$  is much greater than  $D$ . Therefore, atmospheric turbulence imposes a fundamental limit on the performance of an optical system, and this limit is expressed by the parameter  $r_o$ . For the short exposure case, the peak short exposure  $\mathcal{R}$  occurs when the ratio of the telescope diameter  $D$  and the parameter  $r_o$  is approximately 3.8, and this peak  $\mathcal{R}$  is approximately four times the  $\mathcal{R}$  measured in the long exposure case. This indicates that considerable improvement in image quality can be achieved by collecting short exposure images. However, limiting the exposure time also limits the total number of photo events that can be collected by the recording device. For dim objects, this can result in a serious degradation in signal to noise ratio. This problem can be overcome by collecting a large number of short exposure images, re-centering them to eliminate the effects of random image motion, and then averaging these short exposure images to produce a better estimate of the image. Finally, it is important to remember that atmospheric turbulence - and therefore  $\mathcal{R}$  - varies randomly with respect to time. Thus, a more complete understanding of image quality requires a statistical approach.

*2.4.2 Statistics of Image Quality.* In 1977 Fried [9] investigated the possibility that for short exposure images there is a finite probability that an image will be diffraction limited because the wavefront distortion over the aperture was negligible during the exposure. Fried defined a good image as one for which the mean square phase distortion  $\Delta^2$  over the aperture is  $1 \text{ rad}^2$  or less. Using Monte Carlo simulation techniques, Fried modeled the probability of getting a good short exposure,  $P_r$ , as:

$$P_r \cong 5.6 \exp \left[ -0.1557 \left( \frac{D}{r_o} \right)^2 \right], \quad \left( \text{for } \frac{D}{r_o} \geq 3.5 \right) \quad (2.2)$$

This result is significant because it demonstrates that the probability of capturing a single, diffraction limited image decreases as the aperture diameter increases. For example, a probability on the order of  $10^{-3}$  dictates a telescope diameter no greater than  $8r_o$ , and a probability on the order of  $10^{-6}$  dictates a diameter no greater than  $10r_o$ . Thus, at a site with a typical  $r_o$  of 10cm, the telescope aperture must be no greater than 80-100cm, and one would have to collect 1,000-1,000,000 short exposure images to have a high probability of capturing a single, diffraction limited image. The limitation on the aperture size is unacceptable when imaging dim objects, and the requirement to collect such a large number of short exposure images imposes severe data collection and storage requirements. Furthermore, Fried assumed that  $r_o$  was constant during the period of data collection, and this assumption is only reasonable for a very short period of time. Therefore, the probability of capturing a diffraction-limited image may be even more pessimistic than predicted by Fried's result. In addition, Fried's probability expression is limited because it is only valid for fairly large apertures, and the quality criterion is inflexible. Nevertheless, Fried's results are important because they demonstrate that a judicious choice of aperture size and careful selection of short exposure images can yield results which are significantly better than the typical limitation on image quality imposed by atmospheric turbulence [9].

In 1981 Corteggiani [4] extended Fried's results and developed the following expression:

$$\log \Pr \left[ \left( \frac{D}{r_o} \right), 1 \right] = \frac{-0.1557 \left( \frac{D}{r_o} \right)^2}{\exp \left[ \frac{11.014}{\left( \frac{D}{r_o} \right)^2} + \frac{35.35}{18.907 + \left( \frac{D}{r_o} \right)^2} \right]} \quad (2.3)$$

where the notation  $\Pr \left[ \left( \frac{D}{r_o} \right), 1 \right]$  denotes the probability - at a given ratio  $\frac{D}{r_o}$  - of capturing an image with unity mean square phase distortion. Eq.(2.3) removes the requirement that  $\frac{D}{r_o} \geq 3.5$ . Corteggiani also developed an expression which relates

probability of getting an image with wavefront mean square phase distortion  $\Delta^2$  to the probability of getting an image with unity mean square phase distortion:

$$\Pr\left(\frac{D}{r_o}, \Delta^2\right) = \Pr\left(\frac{D}{r_o \Delta^{\frac{6}{5}}}, 1\right) \quad (2.4)$$

According to Corteggiani's model, relaxing the quality criterion for a good exposure image is equivalent to increasing the value of  $r_o$ . Using these results, the probability of capturing a short exposure image with any arbitrary value of  $\Delta^2$  can be determined.

It should be noted that neither Corteggiani's nor Fried's model takes into account the effects of photon noise or detector shot noise. Hence, these models are only valid for relatively bright objects where the signal to noise ratio is sufficiently large to minimize the effects of noise. Furthermore, these models are not necessarily valid for an adaptive optics system, since the performance of such a system is not a simple function of the deformable mirror - the number of subapertures across the deformable mirror also affects performance. Finally, it is important to note that  $\Delta^2$  is not easily determined in an operational setting. Hence, it is necessary to relate  $\Delta^2$  to a more readily accessible quality metric.

*2.4.3 Strehl Ratio and the Marechal Approximation.* One quality metric commonly used to evaluate the performance of optical systems is the Strehl ratio [30],  $S$ :

$$S = \frac{\int \tau(f) df}{\int \tau_o(f) df} \quad (2.5)$$

where  $\tau$  is the optical transfer function of the atmosphere and the telescope and  $\tau_o$  is the optical transfer function of the telescope in the absence of atmospheric turbulence.  $S$  is a normalized version of Fried's quality metric  $\mathcal{R}$ . Marechal [24] derived the following approximation, which relates  $S$  to  $\Delta^2$ :

$$S \approx \left(1 - \frac{1}{2}\Delta^2\right)^2 \quad (2.6)$$

Mahajan [22] determined that Marechal's relation approximates  $S$  with less than 10% error as long as  $S \geq 0.6$  or  $\Delta^2 \leq 0.5 \text{ rad}^2$ . Mahajan also investigated a second approximation:

$$S \approx \exp(\Delta^{-2}) \quad (2.7)$$

and found that this relation approximates  $S$  with less than 10% error as long as  $S \geq 0.3$  or  $\Delta^2 \leq 1.2 \text{ rad}^2$ .

It should be noted that there is an important drawback associated with using  $S$  as a quality metric: one usually measures the image spectrum, not the optical transfer function. The image spectrum is related to the object spectrum by the relation:

$$I(f) = \tau(f)O(f) \quad (2.8)$$

where  $I$  is the image spectrum,  $\tau$  is the optical transfer function, and  $O$  is the object spectrum. To derive the optical transfer function from the image spectrum, it is necessary to divide  $I$  by  $O$ . In the case of a distant point source - such as a star - this isn't a problem because the object spectrum of a distant point source is a constant for all frequencies. However, for any object other than a point source, perfect knowledge of the object spectrum is required to extract the optical transfer function from the image spectrum, and this can only be done at those frequencies where the object spectrum is nonzero. Despite this drawback, these approximations - used in conjunction with Corteggiani's model - make it possible to express image quality in terms of a statistical distribution.

*2.4.4 Improved Image Quality Through Frame Selection.* In 1985 Hequet and Coupinout [16] investigated the feasibility of improving the Strehl ratio  $S$  of an image by collecting a large set of short exposure images, selecting a subset of images according to a quality metric, re-centering each image in this subset to compensate for the effects of random image motion, and then averaging the members of the re-centered subset to extract an estimate of the object. Hequet and Coupinout used the Strehl ratio as their quality metric. Using Eq.(2.7) and Corteggiani's model, Hequet and Coupinout simulated the performance of frame selection as a function of the statistical distribution of  $S$  of the set of short exposure images. Their results indicate that the Strehl ratio  $S$  of an image can be improved by a factor of two by selecting 10% of the re-centered short exposure images. This result is valid as long as  $\frac{D}{r_o} \leq 15$ . Since Hequet and Coupinout's model depends only upon the ratio  $\frac{D}{r_o}$ , it neglects the effects of photon noise and detector shot noise. Imaging wavelength is only indirectly accounted for in this model, since  $r_o$  is proportional to the  $\frac{6}{5}$  power of the imaging wavelength [28]. Despite these limitations, Hequet and Coupinout's paper is a seminal work in this field, because it provides a theoretical validation of the concept of frame selection.

As mentioned earlier, one must know the object spectrum to compute the Strehl ratio from the image spectrum. This is a major drawback for imaging objects other than stars. Hence, finding a quality metric that is easy to compute and does not require prior knowledge of the object spectrum is the key to implementing the frame selection technique in an operational setting.

*2.4.5 Quality Metrics for Frame Selection.* O'Neill [30] provided one of the earliest discussions of quality metrics for rating optical systems. O'Neill listed the following factors:

- (a) Relative Structural Content,  $T$ :

$$T = \frac{\overline{i^2(x,y)}}{\overline{o^2(x,y)}} \quad (2.9)$$

(b) Correlation Quality,  $Q$ :

$$Q = \frac{\overline{i(x,y)o(x,y)}}{\overline{o^2(x,y)}} \quad (2.10)$$

(c) Fidelity Defect,  $F$ :

$$F = 1 - D, \quad (2.11)$$

$$D = \frac{\overline{[o(x,y) - i(x,y)]^2}}{\overline{o^2(x,y)}} \quad (2.12)$$

where  $(x, y)$  represents a spatial coordinate,  $i(x, y)$  represents the measured image,  $o(x, y)$  is the undistorted true image, and the bar operator denotes averaging. All three factors are related through the equation:

$$Q = \frac{1}{2}(T + F) \quad (2.13)$$

The fidelity defect metric is a normalized measure of the mean square error between the true image and the image captured by an optical system. The mean square error metric has been used extensively in testing optical components and in image processing. Some researchers have noted that this metric does not correlate well with subjective human quality assessments [23]. The reasons for this discrepancy are not well understood, but some researchers suggest that the mean square error metric does not adequately mimic what the human visual system does in assessing image quality [29].

Like the Strehl ratio, O'Neill's quality factors are useful in simulation, but they are of limited use in an operational setting because they require prior knowledge of the object. In 1974 Muller and Buffington [26] proposed a set of eight quality metrics they called "sharpness functions", the first seven of which do not require prior knowledge of the object. They defined sharpness functions as functions which reach a maximum value when the phase distortion of the incoming light wave is zero. The Muller and Buffington quality metrics are, in the order they were presented:

$$S_1 = \iint i^2(x, y) dx dy \quad (2.14)$$

$$S_2 = i(0, 0) \quad (2.15)$$

$$S_3 = \iint m(x, y) i(x, y) dx dy \quad (2.16)$$

$$S_4 = \iint \left| \frac{\partial^{m+n} i(x, y)}{\partial x^m \partial y^n} \right|^2 dx dy \quad (2.17)$$

$$S_5 = \iint i^n(x, y) dx dy \quad (2.18)$$

$$S_6 = - \iint i(x, y) r^2 dx dy, \quad (2.19)$$

$$r^2 = x^2 + y^2$$

$$S_7 = - \iint \ln [i(x, y)] i(x, y) dx dy \quad (2.20)$$

$$S_8 = - \int \int |i(x,y) - o(x,y)|^2 dx dy \quad (2.21)$$

$S_1$  and  $S_8$  are unnormalized versions of relative structural content  $T$  and fidelity defect  $F$ .  $S_3$  is an unnormalized version of correlation quality  $Q$  when  $m(x,y)$  - known as the mask function - is equivalent to the true image.  $S_7$  is the equation for entropy, a measure of information content [31]. Muller and Buffington provided mathematical proofs that  $S_1$ ,  $S_3$ ,  $S_4$ ,  $S_5$ , and  $S_8$  reach maximum values for an undistorted image, and hypothesized that  $S_2$ ,  $S_6$ , and  $S_7$  might do the same under typical imaging conditions. Since  $S_1$  through  $S_7$  are easily computed and do not require prior knowledge of the object, they are excellent candidates for use as quality metrics in the frame selection technique. The next section describes implementations of the frame selection technique which employ Muller and Buffington's sharpness functions as quality metrics.

*2.4.6 Frame Selection Implementations.* In 1987 Nieto and others [28] implemented a frame selection technique which uses Muller and Buffington's  $S_3$  metric as the quality metric. They used the long exposure image as the mask function  $m(x,y)$ , and evaluated the improvement in image quality in terms of the full width, half maximum (FWHM) value of the system point spread function. Using a 4m telescope to image the binary stars 48Vir and HRS10, they demonstrated that the FWHM can be improved by a factor of 2.18 by selecting 10% of the re-centered short exposure images.

In 1988 Fuensalida and others [10] implemented a frame selection technique which uses the  $S_3$  metric and the long exposure autocorrelation function as the mask function. They processed a series of short exposure images measured with a 2.5m telescope to produce high resolution images of the symbiotic star AG Peg. They did not state their selection rate, nor did they make a quantitative assessment of

the improvement in image quality, but they did report that the technique uncovered fine, nebular structures that were not visible in the unprocessed data.

Also in 1988, Devaney and others [5] implemented a frame selection technique which uses the  $S_3$  metric and a Gaussian function of width equal to the diffraction limit of the telescope as the mask function. Using a 50cm telescope to image the triple star system ADS6650, they demonstrated that the FWHM can be improved by a factor of 1.9 by selecting 50% of the re-centered short exposure images.

The quantitative assessments of the improvement in image quality reported by these researchers agree very well with the degree of improvement predicted by Hequet and Coupinot. Since Muller and Buffington's quality metrics reach their maxima when phase distortion is zero, frame selection based on the use of these quality metrics is a promising post-processing technique for minimizing the effects of residual phase errors in Air Force adaptive optics systems. In order to fully assess the potential of this technique, the following limitations in our current level of understanding must be overcome.

### *2.5 Limits of Current Knowledge*

The performance of all previous implementations of frame selection has been evaluated in terms of the the point spread function or the Strehl ratio. The statistical implications of frame selection - in particular, the behavior of the signal to noise ratio as a function of the frame selection rate - have not been addressed. This is a key point that must be addressed, because the signal to noise ratio imposes a limit on our ability to image dim objects. Put another way, the performance of the frame selection technique will determine the minimum number of short exposure frames that must be collected to extract a single, high resolution estimate of the object.

As noted previously, the performance of an adaptive optics system cannot be characterized as a simple function of the aperture diameter. Hence, the improvement

in the Strehl ratio predicted by Hequet and Coupinout's model is not necessarily valid for an adaptive optics system.

The results reported in the literature describe attempts to improve the images of single or binary star systems. The Air Force is interested in imaging objects such as satellites, which are extended objects. The performance of the frame selection technique for such objects has yet to be addressed.

## *2.6 Summary*

Atmospheric turbulence imposes a fundamental limit on the performance of any optics system. Adaptive optics systems are unable to fully compensate for the effects of atmospheric turbulence, and this results in residual phase errors which degrade image quality. This thesis will investigate the use of frame selection as a post-processing technique for improving the quality of images measured by Air Force adaptive optics systems. The next chapter develops the methodology for conducting this investigation.

### *III. Methodology*

#### *3.1 Introduction*

Chapter two provided an overview of the problem of imaging through the turbulent atmosphere. The Air Force employs adaptive optics systems to compensate for the random phase fluctuations which result from atmospheric turbulence. Earlier research [40] established that adaptive optics systems cannot fully compensate for these phase aberrations, which means that residual phase errors exist in the wavefront leaving the deformable mirror. These residual phase errors significantly degrade the images measured by an adaptive optics system, so additional processing is needed to improve image quality. Astronomers have successfully employed frame selection as a technique for minimizing the effects of atmospheric turbulence on the performance of passive optical systems, so it is reasonable to hypothesize that frame selection can be employed as a post-processing technique to minimize the effects of residual phase errors in adaptive optics systems. This chapter develops a methodology for testing this hypothesis. Section 3.2 defines the basic terminology that will be used throughout the remainder of this investigation. Section 3.3 justifies the use of Muller and Buffington's sharpness functions as quality metrics in the frame selection process, and identifies the specific sharpness functions implemented in the course of this investigation. Section 3.4 justifies the use of computer simulation in this investigation. Section 3.5 justifies the use of a statistical characterization of the imaging process in the frequency domain as the primary means to evaluate the degree of improvement in image quality realized through application of frame selection, and develops a set of specific performance metrics that are used to express this characterization. Section 3.6 identifies the independent variables which affect the statistics of image formation.

### 3.2 Terminology

Defining the basic terms and concepts is the first step in developing a methodology. The following terms will be used throughout the remainder of this investigation.

*Quality metric:* an equation or algorithm which produces a single numerical value when it is applied to an image. The magnitude of the output of a quality metric is directly proportional to some desired quality or attribute in the image.

*Frame selection rule:* a three-step procedure for identifying a subset of images for processing. First, a specified quality metric is computed for each short exposure image (frame) in the original set. The images are sorted from highest to lowest according to the numerical values of the quality metric, and then those images with the highest values are selected to form the subset.

*Frame selection rate (fsr):* the ratio of the number of frames  $M$  in the subset and the number of frames  $N$  in the original set. Hence:

$$fsr = \frac{M}{N}, \quad M < N \quad (3.1)$$

The frame selection rate is expressed as a percentage of the number of frames in the original set. A frame selection rate of 10% means that the subset identified by the frame selection rule consists of those 10% of the images in the original set which have the highest computed values for the specified quality metric.

*Composite Image:* the image produced by re-centering and averaging a set of short exposure images. The image set used in the averaging process can consist of all the short exposure images collected during an experiment, or a subset of this collection identified by the frame selection rule.

Clearly, the subset identified by the frame selection rule is determined by the quality metric. The next section identifies the specific quality metrics which will be investigated in this thesis.

### 3.3 Sharpness Functions as Quality Metrics

In Chapter two, the set of sharpness functions introduced by Muller and Buffington [26] were discussed. These functions reach their maxima when the phase distortion of the incoming light wave is zero. Since our objective is to minimize the effects of residual phase errors in an adaptive optics system, it is reasonable to propose using sharpness functions as quality metrics. This thesis investigates the following sharpness functions:

$$S_1 = \iint i^2(x, y) dx dy \quad (3.2)$$

$$S_4 = \iint \left| \frac{\partial^2 i(x, y)}{\partial x \partial y} \right|^2 dx dy \quad (3.3)$$

$$S_8 = - \iint |i(x, y) - o(x, y)|^2 dx dy \quad (3.4)$$

These sharpness functions were chosen because they are easy to implement and simple to evaluate. The double integrals can be easily evaluated by using the two dimensional trapezoid rule [6], and the partial derivatives in  $S_4$  can be evaluated by using finite difference approximations [18].  $S_8$  cannot be implemented in an operational setting because it requires prior knowledge of the object. Nevertheless,  $S_8$  was implemented to provide a standard for comparing the performance of  $S_1$  and  $S_4$ . In addition, this thesis proposes and investigates a modified version of  $S_1$ , denoted  $S_{S1}$ .

**3.3.1 A New Quality Metric.** By Parseval's theorem, the integral of the square of the image intensity can be expressed as [20]:

$$\iint i^2(x, y) dx dy = \iint |I(u, v)|^2 du dv, \quad (3.5)$$

where  $I$  represents the Fourier spectrum of the measured image. The image spectrum is related to the object spectrum by the relationship:

$$I(u, v) = H(u, v) O(u, v), \quad (3.6)$$

or in polar coordinates:

$$I(\rho, \theta) = H(\rho, \theta) O(\rho, \theta), \quad (3.7)$$

where  $H$  represents the optical transfer function (OTF) of the optical system, and  $O$  represents the object spectrum. For a diffraction-limited circular aperture unimpeded by atmospheric turbulence, the OTF is given by [12]:

$$H(\rho) = \begin{cases} \frac{2}{\pi} \left[ \cos^{-1} \left( \frac{\rho}{\rho_0} \right) - \frac{\rho}{\rho_0} \left[ 1 - \left( \frac{\rho}{\rho_0} \right)^2 \right]^{\frac{1}{2}} \right] & \text{if } \rho \leq \rho_0 \\ 0 & \text{otherwise} \end{cases} \quad (3.8)$$

where  $\rho_0$  is known as the OTF radius or OTF cutoff frequency, and is given by the relation:

$$\rho_0 = \frac{D}{\lambda d_i}, \quad (3.9)$$

where  $D$  is aperture diameter,  $\lambda$  is the imaging wavelength, and  $d_i$  is the distance from the aperture to the image plane.

Clearly, frequency components present in  $I$  beyond  $\rho_0$  are manifestations of noise. Hence, the quality metric  $S_{S1}$  is defined as:

$$S_{S1} = \int_0^{2\pi} \int_0^{\rho_0} |I(\rho, \theta)|^2 d\rho d\theta \quad (3.10)$$

$S_{S1}$  rejects high frequency components which are the result of photon noise, read noise, and quantization errors, thereby minimizing their effects on the frame selection process.

Now that specific quality metrics have been identified, it is necessary to devise a strategy for evaluating the effects of frame selection on image quality.

### *3.4 Computer Simulation of the Problem*

Computer simulation is the primary tool used to conduct this investigation. This approach was chosen because the frame selection rule is nonlinear, which means that a closed form expression which describes the improvement in image quality resulting from the application of frame selection does not exist. Even if a linear model which approximates this nonlinear process could be developed, the mathematical form of such a model would probably be quite complicated and unwieldy because of the many factors which affect the image formation process. Finally, it is enlightening to note that the probability "laws" developed by Fried [9] and Cortegiani [4] are themselves based on computer simulation.

The simulation code used in this investigation was developed by Michael C. Roggeman [36]. The code consists of an atmospheric turbulence model, and an adaptive optics model which in turn consists of a wavefront sensor model, an adaptive mirror model, and a tilt correction system model. In order to more accurately simulate the performance of an adaptive optics system in an operational setting, this thesis developed a realistic charge-coupled device (CCD) camera model and incorporated it into the original simulation code. Appendix one provides a description of the CCD camera model.

$S_1$ ,  $S_4$ ,  $S_8$ , and  $S_{S1}$  were implemented as subroutines, and incorporated into the original simulation code. To conserve computer disk space, it was necessary to implement the frame selection rule as two separate computer runs. The first run computes the values of the sharpness functions for each short exposure image gen-

erated by the simulation and stores these values in a file. The second run reads the file containing the values of the sharpness functions, sorts them from highest to lowest, and determines the minimum acceptable value according to a frame selection rate specified by the user. Then, the second run exactly recreates the short exposure images generated by the simulation in the first computer run, and computes the statistics of the subset formed by those images whose computed values for the sharpness function are greater than or equal to the minimum acceptable value.

In many ways, a computer simulation is akin to a laboratory experiment, and requires much of the same planning and forethought to ensure success. Before conducting any experiment, the following issues must be addressed:

What is the objective of the experiment?

What phenomena shall be observed during the experiment?

How will the observations be quantified?

What are the independent variables affecting the phenomena?

The objective of the experiments conducted in this investigation is to determine how a composite image formed by averaging a subset of short exposure images identified by the frame selection rule differs from a composite image formed by averaging the entire set of images. The frequency domain statistics of the subset identified by a frame selection rule is the phenomena that will be observed and quantified. This statistical approach was chosen because many of the processes which degrade image formation - photon noise, shot noise effects in the detector, random phase aberrations due to turbulence - are random in nature. A statistical analysis of the frequency domain characterization of the imaging process allows us to determine the maximum limit on image quality imposed by these random processes. The next section explores this statistical analysis in detail. Section 3.6 will identify the independent variables which affect the statistics of image formation.

### 3.5 Statistical Definitions

This thesis examines how the statistics of a subset of short exposure images identified by the frame selection rule differ from the statistics of the entire set. Therefore, it is necessary to define the specific statistical functions that will be observed, quantified and recorded during the experiment.

*3.5.1 Image Spectrum Signal to Noise Ratio (SNR).* For a set of images degraded by a random process, the expected single frame image spectrum Signal to Noise Ratio  $SNR_1$  is defined as:

$$SNR_1(u, v) = \frac{|E[I(u, v)]|}{\{var[I(u, v)]\}^{\frac{1}{2}}}, \quad (3.11)$$

where  $E$  is the expectation operator,  $var$  is the variance operator, and  $I$  is the image Fourier spectrum [17]. In this definition of SNR, any random fluctuation in the image spectrum is manifested as noise.  $SNR_1$  is a measure of the precision of image information at a particular spatial frequency.

*3.5.2 Improved SNR through Averaging.* A standard practice for making a precise determination of a signal level in the presence of noise is to average together a large number of independent measurements of the quantity to be determined [3]. In general, averaging will improve the SNR by a factor  $\sqrt{N}$  where  $N$  is the number of measurements used in the averaging process. Hence, the SNR of a composite image created by averaging  $N$  short exposure realizations is given by:

$$SNR_N(u, v) = \sqrt{N} SNR_1(u, v), \quad (3.12)$$

where the subscript  $N$  denotes the number of short exposure images used to create the composite image.

### 3.6 SNR Performance Metrics

Both  $SNR_1$  and  $SNR_N$  are positive, real, 2-dimensional functions. Since it is rather difficult to directly compare two such functions, it is necessary to define a set of performance metrics which permit us to make such comparisons.

**3.6.1 Radially Averaged SNR.** Fourier image spectra generally exhibit a large degree of radial symmetry. Therefore, the analysis of the  $SNR_1$  and  $SNR_N$  functions can be simplified by employing the radially averaged SNR functions:

$$\overline{SNR_1}(\rho) = \frac{1}{2\pi\rho} \int_0^{2\pi} SNR_1(\rho, \theta) d\theta \quad (3.13)$$

$$\overline{SNR_N}(\rho) = \frac{1}{2\pi\rho} \int_0^{2\pi} SNR_N(\rho, \theta) d\theta \quad (3.14)$$

**3.6.2 Noise Equivalent Frequency Cutoff.** As noted previously, the Fourier spectrum of an image formed by passing through a diffraction-limited circular aperture reaches zero at the OTF radius. Noise, however, generally exhibits a broad frequency spectrum that usually exceeds the OTF radius. Hence, there generally exists a frequency where the magnitude of the noise spectrum and the magnitude of the signal spectrum are equal. This point is known as the noise equivalent frequency cutoff  $\eta$  and is defined as

$$\eta = \rho \text{ such that } \overline{SNR_1}(\rho) = 1.0 \quad (3.15)$$

$\eta$  is measure of the highest spatial frequency where the signal is known with a minimum acceptable degree of certainty. Thus,  $\eta$  permits us to compare the overall signal quality of different subsets at high frequencies.

**3.6.3 SNR Gain.**  $SNR_N$  is a function of the number of short exposure images used in the averaging process. Clearly, applying the selection rule will result in the use of a smaller number of short exposure frames in the averaging process. To compare  $SNR_N$  of the entire set of  $N$  frames to  $SNR_M$  of a subset consisting of  $M$  frames, the SNR Gain function  $G$  is defined as:

$$G(\rho) = \frac{\overline{SNR_M(\rho)}}{\overline{SNR_N(\rho)}}, \quad M < N \quad (3.16)$$

$G$  permits us to compare the relative gain or loss in the composite image signal to noise ratio that results from applying the frame selection rule. Any value above 1.0 at a particular radial frequency constitutes a gain in SNR while any value below 1.0 constitutes a loss.

**3.6.4 Integrated Gain.**  $G$  is still a 1-dimensional function. To compare the relative improvement or degradation of composite image signal to noise ratio that results from applying the frame selection rule, we desire a simpler quality metric. If  $SNR_M$  improves as the result of applying the frame selection rule, then the area under  $G$  will be greater than the case where there is no overall improvement - or perhaps a degradation - of  $SNR_M$ . Hence, the quality metric  $A_G$  is defined as:

$$A_G = \int_0^{\rho_0} G(\rho) d\rho, \quad (3.17)$$

where  $\rho_0$  is the OTF radius. Now consider the hypothetical case where:

$$\overline{SNR_M(\rho)} = \overline{SNR_N(\rho)} \quad \forall \rho \leq \rho_0 \quad (3.18)$$

$A_G$  then becomes:

$$A_G = \int_0^{\rho_0} d\rho \quad (3.19)$$

If we normalize the radial frequency  $\rho$  such that  $\rho_o = 1.0$ , then  $A_G = 1.0$  when there is no overall improvement in composite image signal to noise ratio. Any value for  $A_G$  above 1.0 indicates an overall improvement while any value less than one indicates an overall degradation in SNR.

Now that the phenomena to be observed during the experiment has been identified and three quality metrics -  $\eta$ ,  $G$ , and  $A_G$  - have been defined, it is necessary to identify those independent variables which affect the phenomena.

### 3.7 Independent Variables

Eq.(3.12) states that the signal to noise ratio of a composite image formed by averaging a set of  $N$  short exposure images is equal to the expected single frame  $SNR$  for the set multiplied by  $\sqrt{N}$ . If we let  $SNR_{SE}$  denote the expected single frame  $SNR$  for a set of short exposure images measured by an adaptive optics system free of residual tilt error, using a charge-coupled device (CCD) camera, the  $SNR$  for the average image would be given by:

$$SNR_N(u, v) = \sqrt{N} SNR_{SE}(u, v) \quad (3.20)$$

Hence, if we had an expression for  $SNR_{SE}$ , we could identify the relevant independent variables. Fortunately, an expression for  $SNR_{SE}$  has been derived [34] and has the form:

$$SNR_{SE}(u, v) = \frac{K |E_{SE}[H(u, v)] O(u, v)|}{\{K + K^2 |O(u, v)|^2 var[H(u, v)] + P \sigma^2\}^{\frac{1}{2}}} \quad (3.21)$$

where  $K$  is the average number of photo events per integration time,  $E_{SE}$  is the expectation operator,  $O$  is the object spectrum,  $H$  is the system OTF,  $P$  is the number of pixels employed by the CCD camera and  $\sigma^2$  is the camera read noise

variance. By examining Eqs.(3.20-3.21), the relevant independent variables can be found.

*3.7.1 Number of Short Exposure Images,  $N$ ,  $M$ .* The number of short exposure images that can be captured in a single data collection run is determined by the apparent speed of the object and any rotational or translational object motion. The faster the object moves in relation to the celestial vault, the more difficult tracking becomes. Most astronomical objects appear stationary with respect to the celestial vault, which means that the number of frames that can be collected may number several tens of thousands. However, an artificial satellite may transverse the night sky in a matter of minutes, which limits the number of frames to a few hundred to a few thousand. Obviously, applying the frame selection rule will result in a subset of  $M$  images which is smaller than the original set. Thus, the number of images  $M$  in a subset used to produce a composite image will affect the SNR of that image.

*3.7.2 Average Photo events,  $K$ .* The average number of photo events per integration time recorded in a short exposure image is a function of the visual magnitude of the object, the image exposure time, the mean imaging wavelength, and the light gathering capacity of the optical device. Apparent visual magnitude  $m_v$  is a system employed by astronomers to compare the relative brightness of objects in the night sky [32]. Each step in visual magnitude corresponds to a factor 2.5 increase in apparent brightness, and smaller values indicate brighter objects. The light gathering capacity of an optical device is governed by the area of the aperture, minus the area of any obstructions.

Terry M. Gray of the Kirtland AFB Phillips Lab passive imaging department has developed a computer program named VMAG which calculates the average photon flux of an image based on the visual magnitude of the object, the imaging wavelength and the light gathering capacity of the optical device. Table 3.1 tab-

ulates the average photo events  $K$  and apparent visual magnitude  $m_v$  for several sky objects, based on a 1 meter aperture, an imaging wavelength of 500 nm, and a 1.8-ms integration time.

Table 3.1 Visual Magnitude and Photo events for Common Sky Objects

OBJECT	$m_v$	$K$
Venus	-4.4	$2.35 \cdot 10^7$
Jupiter	-2.5	$4.11 \cdot 10^6$
Sirius	-1.5	$1.59 \cdot 10^6$
Artificial Satellite ( <i>typical</i> )	-.96	$1.00 \cdot 10^6$
Polaris	+2.2	$5.54 \cdot 10^4$

3.7.3  $E_{SE}[H(u, v)]$  and  $var[H(u, v)]$ . The mean and variance of the system OTF are not independent variables, since they depend on the seeing conditions, and the performance of the adaptive optics system. The performance of an adaptive optics system depends on the wavefront sensor subaperture size and the deformable mirror actuator spacing. The performance of the adaptive optics system is also a function of the average number of photo events. Therefore, for the purposes of this experiment, the relative seeing conditions - characterized by the parameter  $r_0$  - will be treated as the primary independent variable relating to the mean and variance of the system OTF.

3.7.4 *Object Spectrum*. The fact that the SNR is object dependent presents a major complication in analyzing the results of the experiment. The results obtained from the experiment are specific to the particular object used in the experiment, and great care must be taken when attempting to apply these results to another, dissimilar object. Results for star images often appear in the literature [5, 10, 28], however, it should be remembered that the Air Force is primarily interested in imaging extended objects.

*3.7.5 CCD Camera Noise.* The Gaussian additive read noise introduced by a CCD camera is a function of the number of pixels  $P$  and the noise variance per pixel  $\sigma^2$ . The quantity  $\sigma^2$  is hardware dependent; typical values for high quality, commercially available CCD cameras are in the range of 10-15 electrons per pixel. The total number of pixels is also a factor, therefore oversampling should be avoided to minimize the effects of CCD noise.

### *3.8 Summary*

This chapter defined the basic terminology used in frame selection, identified the specific quality metrics to be investigated, and presented a mathematical definition of the phenomena - signal to noise ratio - that will be observed during the experiment. Three performance metrics which facilitate comparisons of the signal to noise ratio between different short exposure image sets have been developed, and the independent variables affecting the signal to noise ratio have been identified. Chapter four will present the results of the experiment.

## IV. Analysis Results

### 4.1 Introduction

This chapter explores the hypothesis that frame selection based on Muller and Buffington's sharpness functions can be employed to enhance images produced by an adaptive optics system. Chapter three developed a methodology for conducting this investigation. The frame selection rule was defined as a three-step procedure where a specified quality metric is computed for each short exposure image (frame) in the set, the images are sorted from highest to lowest according to the numerical value of the quality metric, and then those images with the highest values are selected according to an arbitrary frame selection rate to form the image subset. The frame selection rate was defined as the ratio of the number of frames selected and the total number of frames in the set. Four quality metrics which can be employed in frame selection were identified:

$$S_1 = \int \int i^2(x, y) dx dy \quad (4.1)$$

$$S_4 = \int \int \left| \frac{\partial^2 i(x, y)}{\partial x \partial y} \right|^2 dx dy \quad (4.2)$$

$$S_8 = - \int \int |i(x, y) - o(x, y)|^2 dx dy \quad (4.3)$$

$$S_{S1} = \int_0^{2\pi} \int_0^{\rho_0} |I(\rho, \theta)|^2 d\rho d\theta \quad (4.4)$$

$S_1$ ,  $S_4$ , and  $S_8$  are sharpness functions proposed by Muller and Buffington [26].  $S_{S1}$  is a variant of  $S_1$  that was developed in Chapter three. Three performance metrics - noise equivalent frequency cutoff ( $\eta$ ), SNR gain ( $G$ ), and integrated gain ( $A_G$ ) -

were developed to quantify changes in image signal to noise ratio. The following independent variables which affect the statistics of a set of short exposure images were identified: the number of images in the set ( $N$ ), the number of images in the subset identified by a frame selection rule ( $M$ ), the average number of photo events per image ( $K$ ), the image spectrum ( $I$ ), atmospheric seeing conditions ( $r_o$ ), and the noise characteristics of the detector ( $P, \sigma^2$ ). To address the effect of each of these factors on image quality, and to determine which of the four quality metrics performs the best, five simulation experiments were performed.

Experiment one establishes a baseline for comparison by demonstrating the performance of the quality metrics for an arbitrarily chosen set of "average" conditions. The performance of the different selection rules are compared using the  $\eta$ ,  $G$ , and  $A_G$  performance metrics. Experiment two duplicates the conditions of experiment one, with an extended object substituted for the point source. Experiment three investigates the performance of the different quality metrics for different seeing conditions. Experiment four investigates the effects of different light levels, and experiment five investigates the effects of detector noise.

*4.1.1 System Parameters.* Common optical system parameters were used for all simulations. The simulated system was a 1 meter adaptive optics telescope with no central obstruction. The density of the wavefront sensors was ten across the diameter of the aperture, and the actuator separation on the deformable mirror was 11cm. The imaging and wavefront sensing wavelength was 500nm. The image sets generated by the simulation consisted of 500 frames. It should be noted that the size of the telescope aperture and the size of the image set were dictated by limitations in the available computational resources, rather than operational considerations.

## 4.2 Experiment One

This experiment is the initial investigation into the implications of frame selection. First, the statistical implications of frame selection are examined in detail. Then the performance of frame selection with respect to image signal to noise ratio is examined. Finally, the performance of the four different quality metrics is compared. This experiment establishes a baseline for comparing the results of later experiments.

**4.2.1 Simulation Parameters.** The object was a point source of apparent brightness  $m_v$  equal to -1.0. The parameter  $r_o$  was set to 10cm to simulate "average" seeing conditions at a good observatory. Photon limited conditions (no CCD noise) were simulated.

**4.2.2 Statistical Implications.** As discussed in Chapter three, the expected single frame image spectrum Signal to Noise Ratio  $SNR_1$  is given by [17]:

$$SNR_1(u, v) = \frac{|E[I(u, v)]|}{\{\text{var}[I(u, v)]\}^{\frac{1}{2}}} \quad (4.5)$$

To gain insight into the implications of frame selection, the mean and variance of the image spectrum  $I$  shall be examined. For this portion of the experiment, we will limit the discussion to the performance of the  $S_8$  quality metric. The performance of the other quality metrics will be addressed later. Figure 4.1 illustrates how the estimate of the image spectrum changes as a function of the selection rate. Frame selection changes the estimate of the image spectrum over 75% of the diffraction-limited frequency range. At a 10% selection rate, there is a 50% increase in the estimate at 35% of the diffraction limit.

To determine whether this estimate is a more accurate estimate of the true image spectrum, the mean square error of the estimate and the true image were computed, using the the fidelity defect metric  $F$  discussed in Chapter two:

$$F = 1 - D, \quad (4.6)$$

$$D = \frac{|I_e(u, v) - I_d(u, v)|^2}{I_d^2(u, v)} \quad (4.7)$$

where  $I_d$  is the diffraction limited true image spectrum and  $I_e$  is the estimate.  $F$  is a convenient way to express mean square error, because its range is  $[-1, +1]$ , where  $+1$  indicates perfect fidelity [30].

Figure 4.2 illustrates the relation between  $F$  and frame selection rate. The estimate produced by averaging the subset identified at a 5% selection rate is 30% better - in a mean square error sense - than the estimate obtained by averaging the entire image set. Hence, frame selection significantly improves the accuracy of the estimate of the image spectrum.

Since the image spectrum of a distant point source is a scaled version of the optical transfer function (OTF), the curves in Figure 4.1 represent the average OTF, realized over many short exposure images. As noted in Chapter three, the Strehl ratio  $S$  is a common quality metric used to evaluate the performance of optical systems [30].  $S$  is given by:

$$S = \frac{\int \tau(f) df}{\int \tau_o(f) df} \quad (4.8)$$

where  $\tau$  is the optical transfer function of the atmosphere and the telescope and  $\tau_o$  is the optical transfer function of the telescope in the absence of atmospheric turbulence. Figure 4.3 illustrates the relation between  $S$  and frame selection rate. A 10% selection rate yields a value of  $S$  that is 27% better than that obtained by averaging the entire image set. The image domain counterpart of the OTF is the point spread function (PSF). The amount of blurring that results from diffraction is inversely proportional to the width of the PSF [11]. Hence, narrowing the PSF

decreases image blurring. Figure 4.4 demonstrates that frame selection narrows the average PSF, which translates into less image blurring.

Figure 4.5 illustrates how frame selection changes the variance of the image spectrum. Frame selection decreases the variance over 85% of the diffraction-limited frequency range. At 35% of the diffraction limit, image variance is decreased by a factor of 5.6. This translates into an increase in the precision of the estimate of the object. Hence, frame selection results in a net increase in  $SNR_1$  over approximately 85% of the diffraction-limited frequency range. This increase is the result of an increase in the estimate of the image spectrum and a corresponding decrease in the variance. The next section explores the effect of these statistical changes on image signal to noise ratio.

**4.2.3 Frame Selection and Image SNR.** Chapter three developed a set of performance metrics for evaluating changes in signal to noise ratio. These performance metrics are noise equivalent frequency cutoff  $\eta$ , SNR gain  $G$ , and integrated gain  $A_G$ , and are defined as:

$$\eta = \rho \text{ such that } \overline{SNR_1}(\rho) = 1.0 \quad (4.9)$$

$$G(\rho) = \frac{\overline{SNR_M}(\rho)}{\overline{SNR_N}(\rho)}, \quad M < N \quad (4.10)$$

$$A_G = \int_0^{\rho_0} G(\rho) d\rho \quad (4.11)$$

$\eta$  is a single frame performance metric which permits us to compare different subsets in terms of the maximum usable frequency.  $G$  is a composite image metric which indicates gain or loss of signal to noise ratio at different radial frequencies.  $A_G$  describes overall changes in composite image signal to noise ratio.

Figure 4.6 illustrates the relation between  $\eta$  and frame selection rate.  $\eta$  improves from approximately 85% of the diffraction limit for the entire set to 91% at a 5% selection rate, for a net increase of 7%. Hence, frame selection changes the subset statistics by discarding the poorer images in the original set. As the frame selection rate increases, only the best images remain, and this translates into an increase in the highest usable radial frequency. It is important to remember that  $\eta$  is a single frame metric. It describes the maximum usable radial frequency of the expected value of the image spectrum.

Figure 4.7 illustrates the changes in the signal to noise ratio of a composite image formed by averaging a set of short exposure images. At the 60% selection rate,  $A_G$  reaches a maximum value of 1.15, then steadily decreases as the selection rate decreases. This curve illustrates a key implication of frame selection: as the frame selection rate decreases, the subset statistics improve as the poorer images are discarded, however, the size of the subset decreases which means that there is less noise reduction achieved through averaging. At higher selection rates, the improvement in set statistics is the dominant factor affecting the composite image signal to noise ratio. However, there is a point where additional improvement in the subset statistics is insufficient to compensate for the loss in noise reduction due to averaging a smaller number of images. Hence, at low selection rates the size of the subset is the dominant factor affecting signal to noise ratio.

The integrated gain curve depicted in Figure 4.7 is very useful because it can be used to identify the performance limit in terms of frame selection rate. Since  $A_G$  is at a maximum at the 60% selection rate, this is the selection rate where the maximum gain in composite image signal to noise ratio can be expected. When  $A_G$  is equal to one, the area under the  $G$  corresponding to a subset of  $M$  images is equivalent to the area under  $G$  corresponding to the original set of  $N$  images, indicating that the average gain in signal to noise ratio for the diffraction-limited frequency range is equivalent for both cases. Hence, there will be an overall improvement in signal to

noise ratio for those selection rates where  $A_G$  is greater than one. The point where  $A_G$  drops to one establishes the limit of performance in terms of frame selection rate. Figure 4.8 demonstrates this point. The gain curve at the 60% selection rate corresponds to the point of maximum gain indicated by Figure 4.7, the 25% selection rate corresponds to the point where  $A_G$  is equal to one, and the 10% selection rate corresponds to a point where  $A_G$  is below one. At the 60% selection rate, there is an improvement in signal to noise ratio for 65% of the diffraction-limited frequency range. The maximum gain occurs at 40% of the diffraction limit and represents a 35% improvement in SNR. There is a 15% loss in SNR at lower frequencies and a 5% loss at high frequencies. At the 30% selection rate, the frequency range where improvement occurs is 30% smaller than the equivalent range at the 60% selection rate. There is a 50% loss of SNR at lower frequencies and a 35% loss at high frequencies. At the 10% selection rate, the frequency range where improvement occurs is 55% smaller than the equivalent range at the 60% selection rate and the loss in SNR approaches 50% at high frequencies. The steady loss in SNR at high frequencies as the frame selection rate decreases is due to less noise reduction through averaging. At high frequencies, the effects of photon noise are dominant, hence, more frames are required to minimize these effects.

*4.2.4 Signal to Noise Ratio and Image Resolution.* Figures 4.3 and 4.7 illustrate another important implication of frame selection: there is an optimal frame selection rate beyond which the composite image signal to noise ratio degrades, however, optical resolution as measured by the Strehl ratio continues to improve as the selection rate decreases. Since a higher Strehl ratio corresponds to a narrower point spread function, this means that image blurring due to diffraction decreases as the frame selection rate decreases. However, signal to noise ratio will degrade beyond a certain frame selection rate, and this degradation is most pronounced at the higher frequencies. This means that at low frame selection rates, there is a trade-off between resolution and signal to noise ratio. At low frame selection rates,

one can minimize the effects of blurring due to diffraction at the expense of more pronounced noise effects at higher frequencies.

**4.2.5 Quality Metric Performance.** All of the results presented up to this point were generated with the  $S_8$  quality metric. It was noted in Chapter three that this quality metric cannot be implemented in an operational setting, because it requires prior knowledge of the object. This section analyzes the performance of the  $S_1$ ,  $S_4$ , and  $S_{S1}$  quality metrics in relation to the results analyzed previously for  $S_8$ . Figure 4.9 illustrates the performance of the different quality metrics as measured by  $\eta$ . There is very little difference in performance between the different metrics.  $\eta$  improves from approximately 85% of the diffraction limit for the entire set to 91% at a 5% selection rate, for a net increase of 7%.

Figure 4.10 illustrates the performance of the different quality metrics as measured by  $A_G$ .  $S_8$  demonstrates the best performance of the four selection rules. At the 60% selection rate  $A_G$  reaches a maximum of 1.15, and yields an overall gain in  $A_G$  for selection rates greater than 25%.  $S_{S1}$  and  $S_1$  produce the next best performance, with a maximum of 1.12 occurring at the 70% selection rate, and a net gain in  $A_G$  for selection rates greater than 30%.  $S_4$  produces the poorest results, with a maximum of 1.07 occurring at 70% selection rate, and a net gain in  $A_G$  for selection rates greater than 35%.

Figure 4.11 demonstrates how the gain curves for the  $S_{S1}$  metric behave as function of frequency at the 70%, 30%, and 20% selection rates. At the 70% selection rate, a gain in SNR occurs over 65% of the diffraction-limited frequency range. The peak gain occurs at 40% of the diffraction limit, and represents a 30% gain in SNR. There is a 5% loss at low frequencies, and a 2.5% loss at high frequencies. At the 30% selection rate, the peak gain occurs at 40% of the diffraction limit, and represents a 35% gain SNR. Over the frequency range [0.3, 0.6] the gain curve for the 35% selection rate is approximately 5% greater than the gain curve for the 70% selection

rate, however, the overall range for which a gain is realized is 25% less. There is a 40% loss in SNR at low frequencies, and a 25% loss at high frequencies. At the 20% selection rate, the range over which a gain is realized is 30% less than the SNR gain range produced at the 70% selection rate. There is a 50% loss in SNR at low frequencies, and a 30% loss at high frequencies. These results demonstrate that the best overall improvement occurs at the 70% selection rate, which was predicted by the  $A_G$  curve.

To determine the relative performance of the four selection rules, consider the gain curves at the 75% selection rate. These curves are depicted in Figure 4.12. Again,  $S_8$  achieves the best performance, with a gain in SNR occurring over 70% of the diffraction-limited frequency range. The peak gain occurs at 35% of the diffraction limit and represents a 28% gain in SNR.  $S_{S1}$  achieves a net gain over the same range as  $S_8$ , but with a slightly lower peak gain occurring at 35% of the diffraction limit.  $S_1$  closely resembles  $S_{S1}$ , but exhibits a more rapid drop-off in gain as frequency increases.  $S_4$  exhibits the poorest performance, with a net gain over the 65% of the frequency range, and a peak gain of 20% at 42% of the diffraction limit. Of the three quality metrics which can be implemented in an operational setting,  $S_{S1}$  demonstrates the best overall performance.

*4.2.6 Conclusions.* The results of this section are significant because they establish the major implications of frame selection: frame selection improves image quality by narrowing the point spread function and improving the signal to noise ratio, particularly in the mid-frequency range. Furthermore, this improvement in signal to noise ratio is a function of the frame selection rate, and there generally exists an optimal selection rate, beyond which signal to noise ratio degrades. This degradation at low frame selection rates is due to an insufficient number of frames in the subset to adequately reduce the effects of photon noise through the averaging process. Hence, photon noise imposes the fundamental limit on the performance of the frame selection rule. It is important to remember that these results have only

been established for the case of a relatively bright point source. The Air Force is primarily interested in imaging extended objects. The next experiment will address this issue.

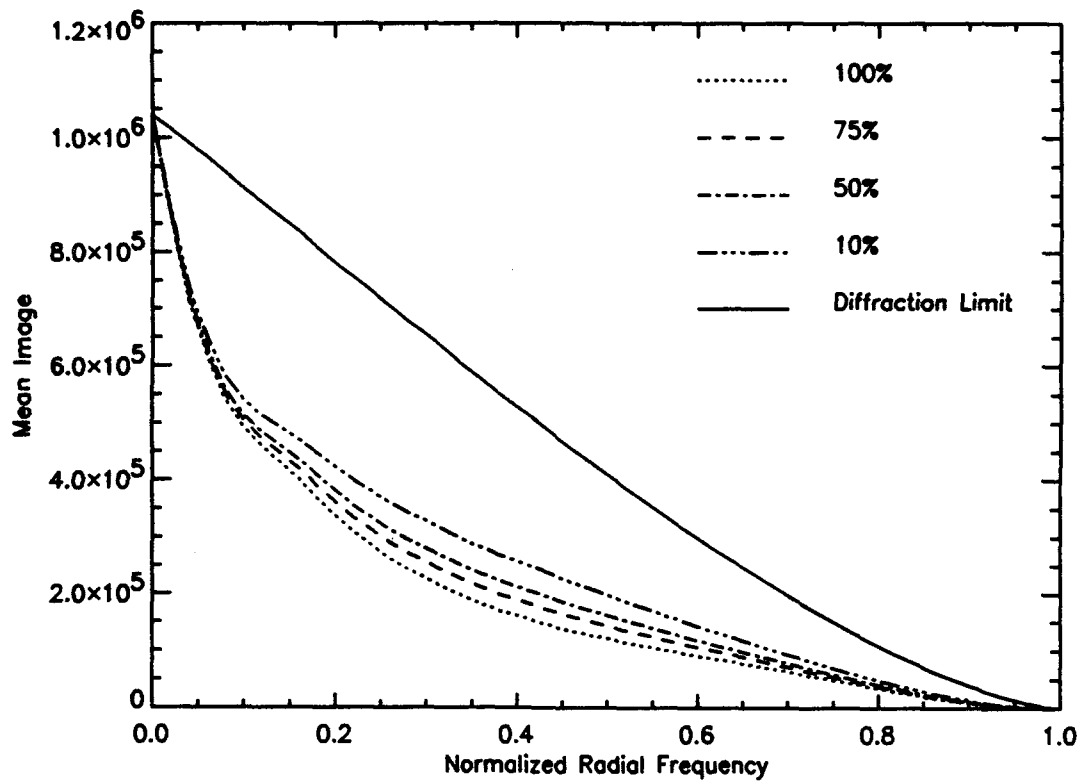


Figure 4.1 Mean Image Spectrum vs Frequency, Point Source,  $m_o = -1$ ,  $r_o = 10\text{cm}$

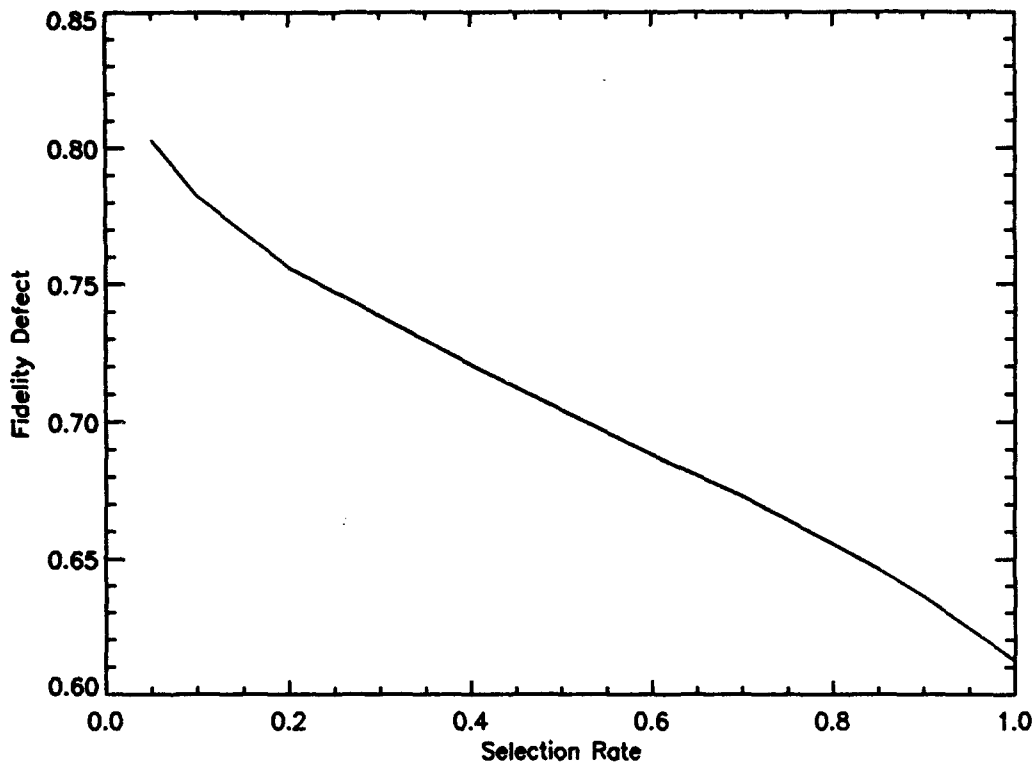


Figure 4.2 Fidelity Defect vs Selection Rate, Point Source,  $m_v=-1$ ,  $r_o=10\text{cm}$

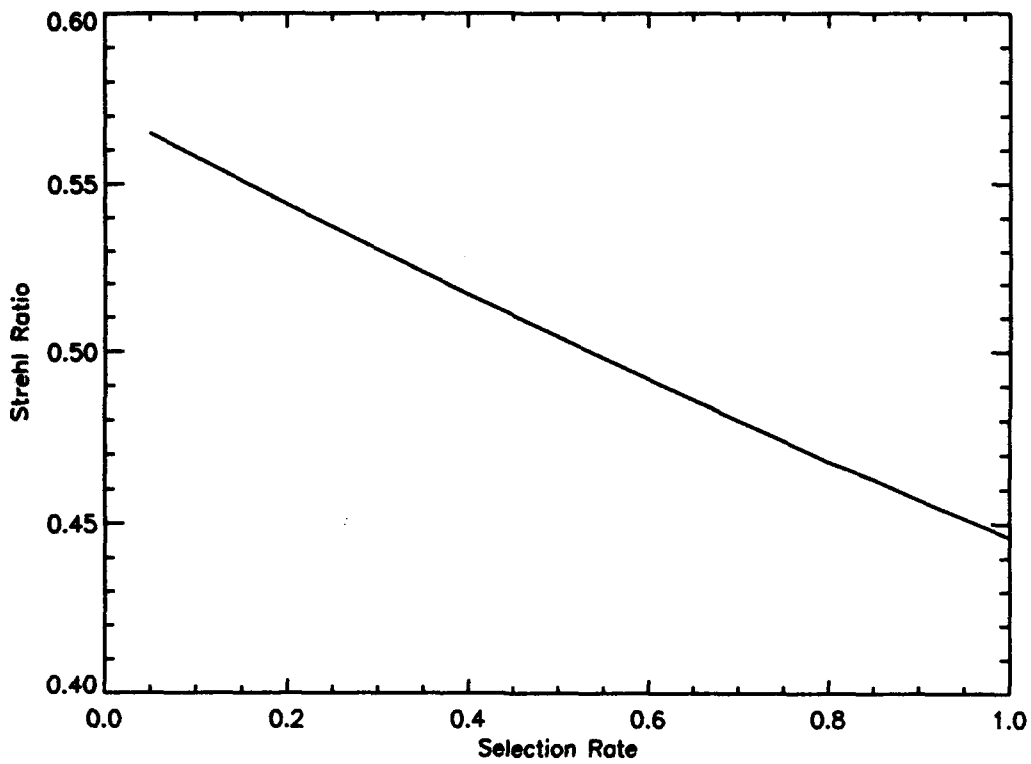


Figure 4.3 Strehl Ratio vs Selection Rate, Point Source,  $m_o=-1$ ,  $r_o=10\text{cm}$

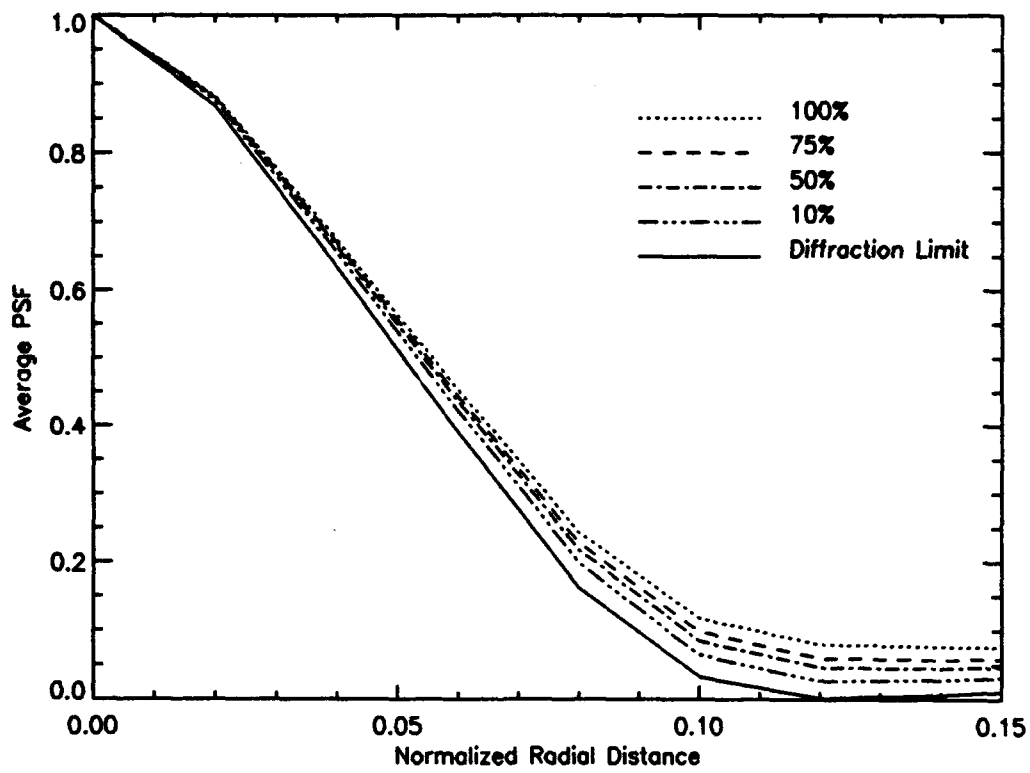


Figure 4.4 Point Spread Function, Point Source,  $m_o = -1$ ,  $r_o = 10\text{cm}$

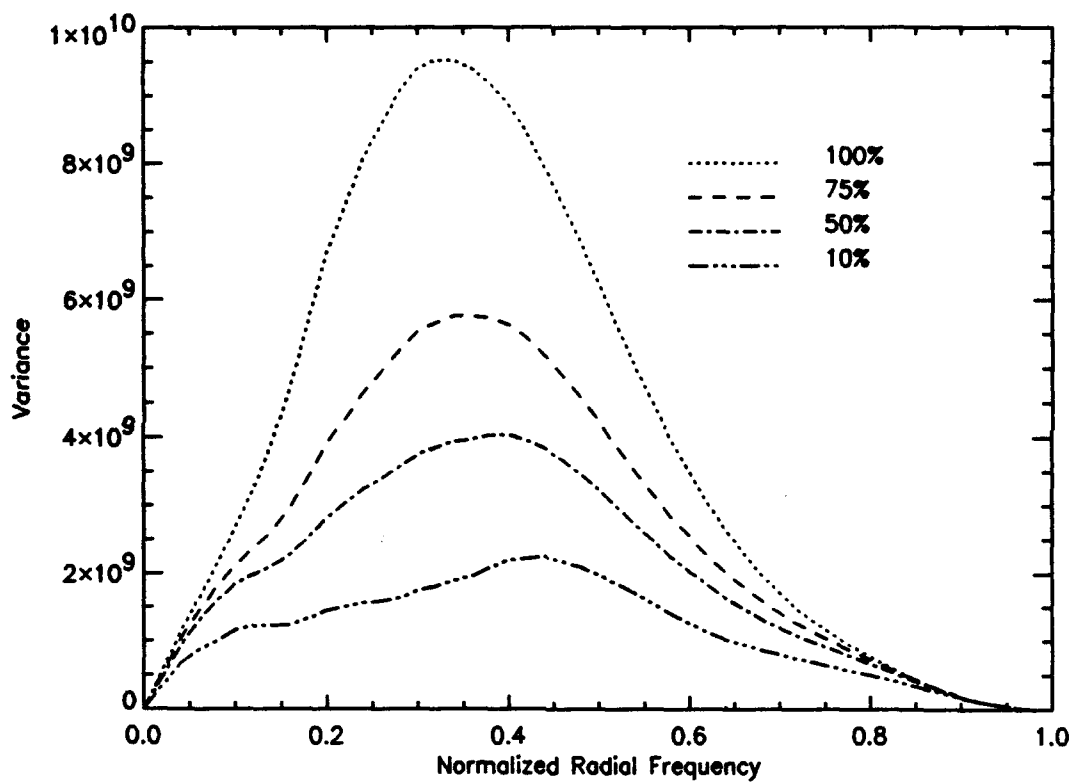


Figure 4.5 Image Spectrum Variance vs Frequency, Point Source,  $m_v = -1$ ,  $r_o = 10\text{cm}$

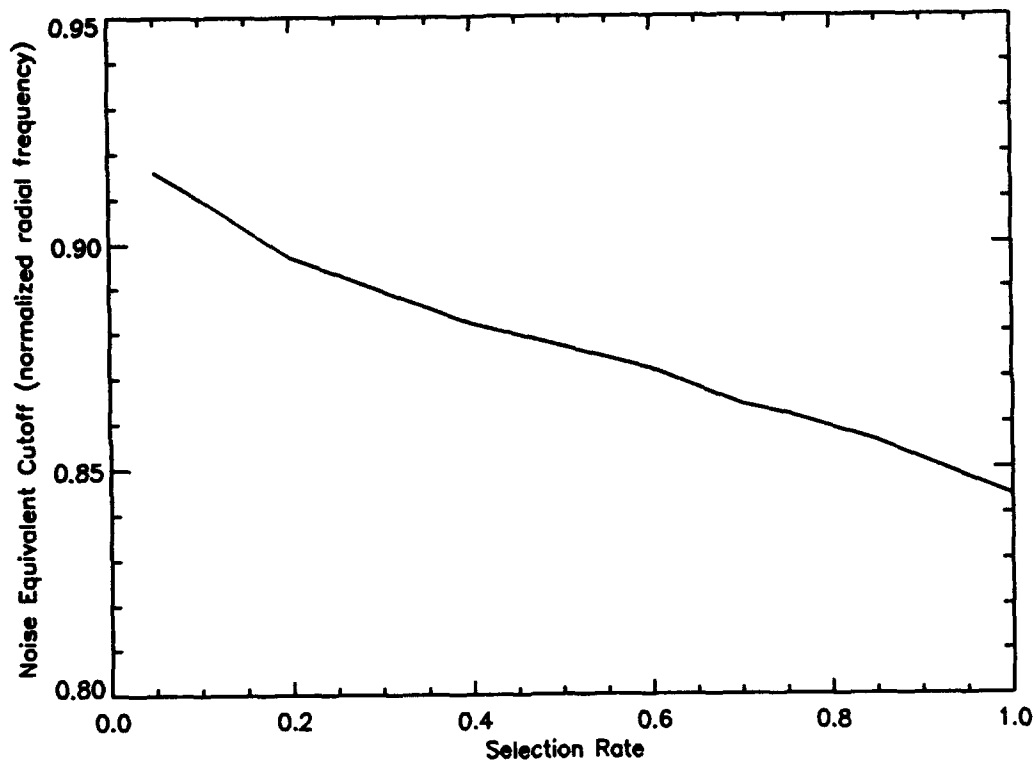


Figure 4.6  $\eta$  vs Selection Rate, Point Source,  $m_v=-1$ ,  $r_o=10\text{cm}$

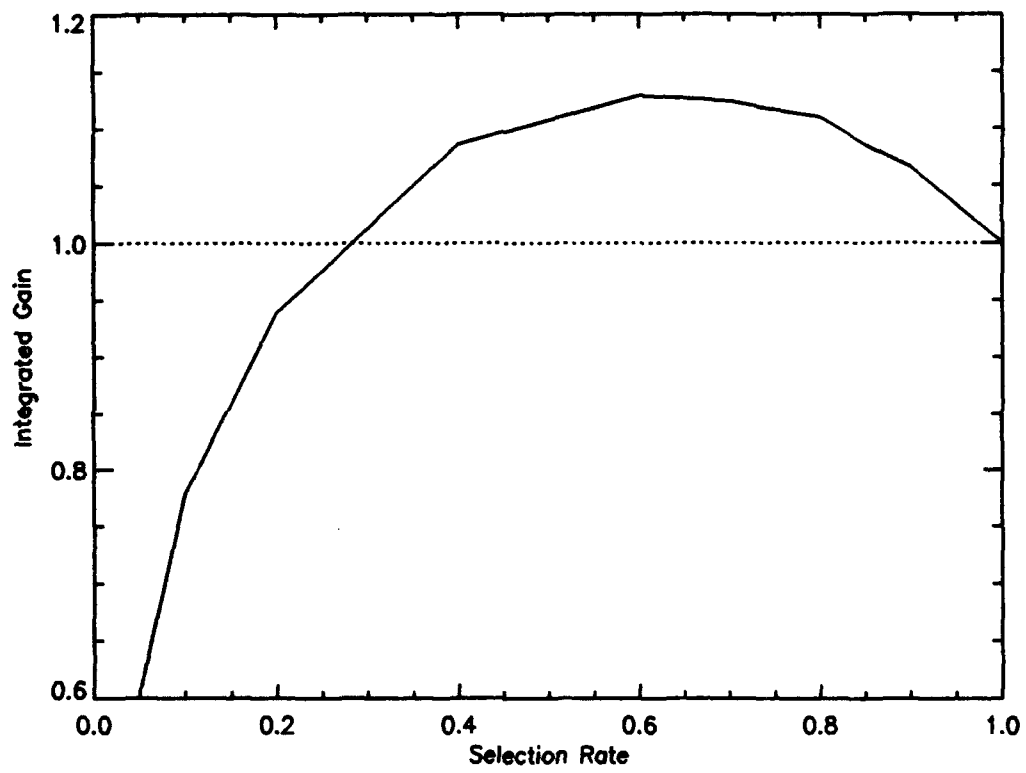


Figure 4.7  $A_G$  vs Selection Rate, Point Source,  $m_v=-1$ ,  $r_o=10\text{cm}$

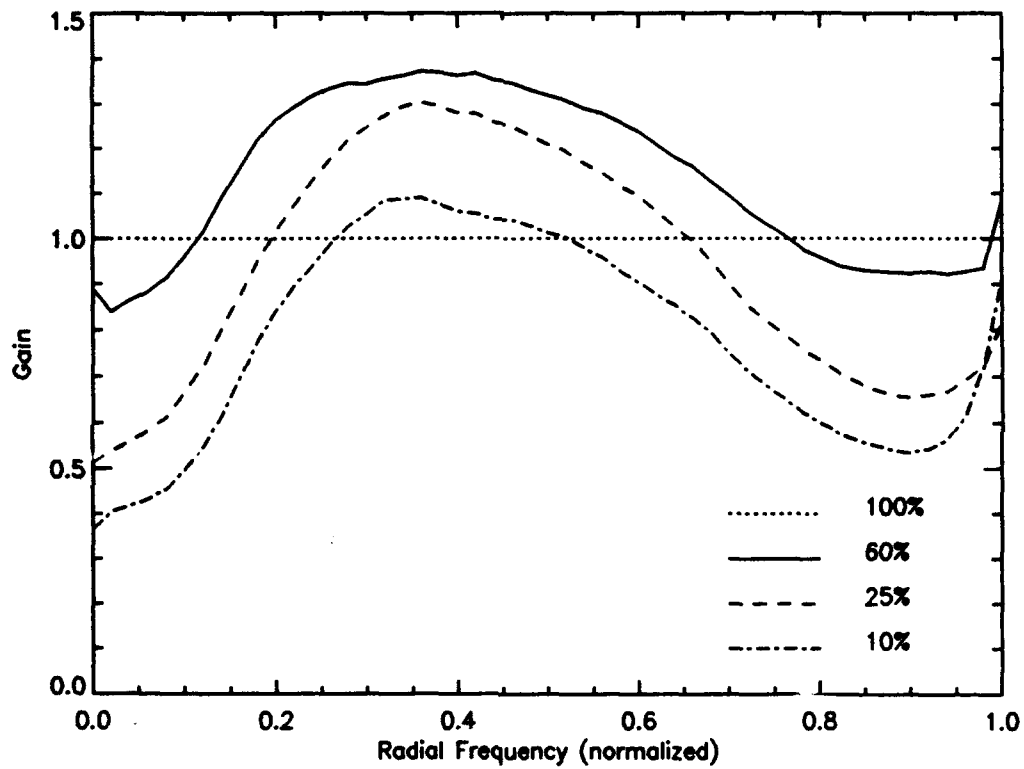


Figure 4.8 Gain Curves, 60%, 25%, 10% Selection Rates, Point Source,  $m_v = -1$ ,  $r_o = 10\text{cm}$

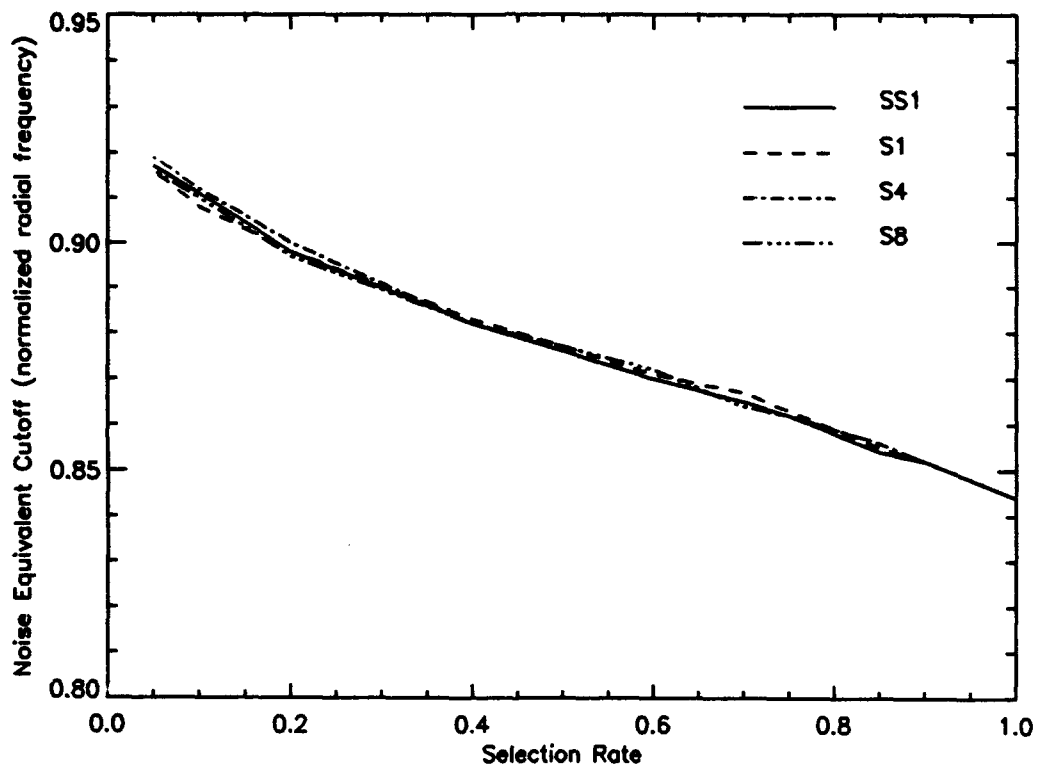


Figure 4.9  $\eta$  vs Selection Rate, Different Quality Metrics, Point Source,  $m_v=-1$ ,  $r_o=10\text{cm}$

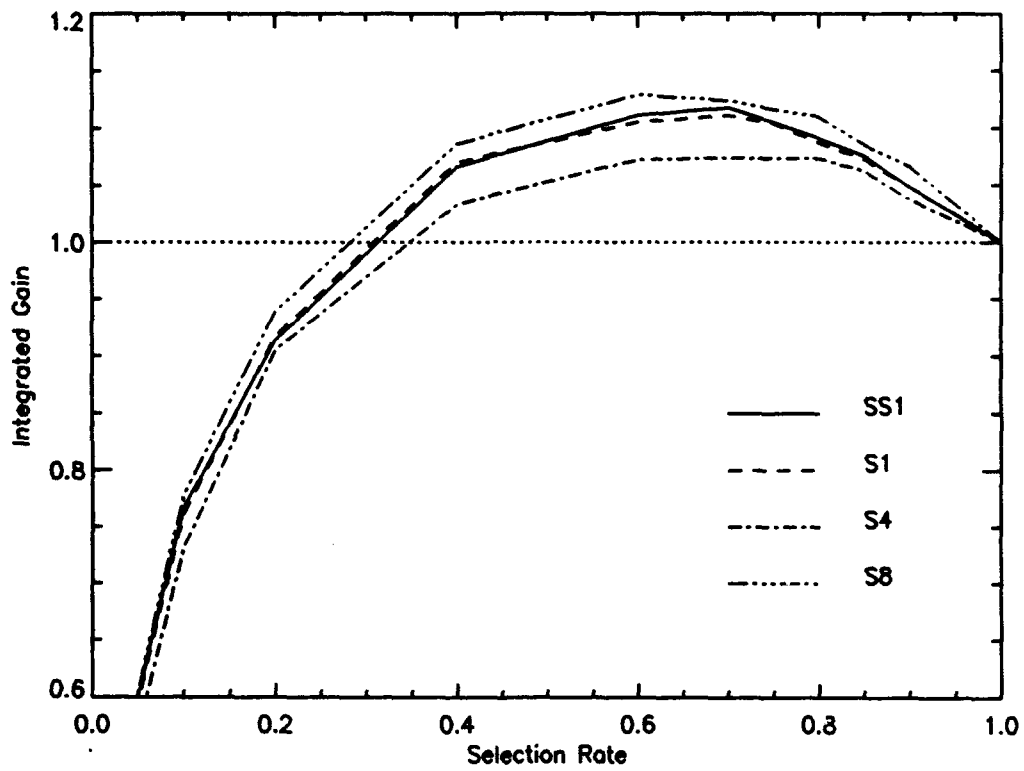


Figure 4.10  $A_G$  vs Selection Rate, Different Quality Metrics, Point Source,  $m_v=-1$ ,  $r_o=10\text{cm}$

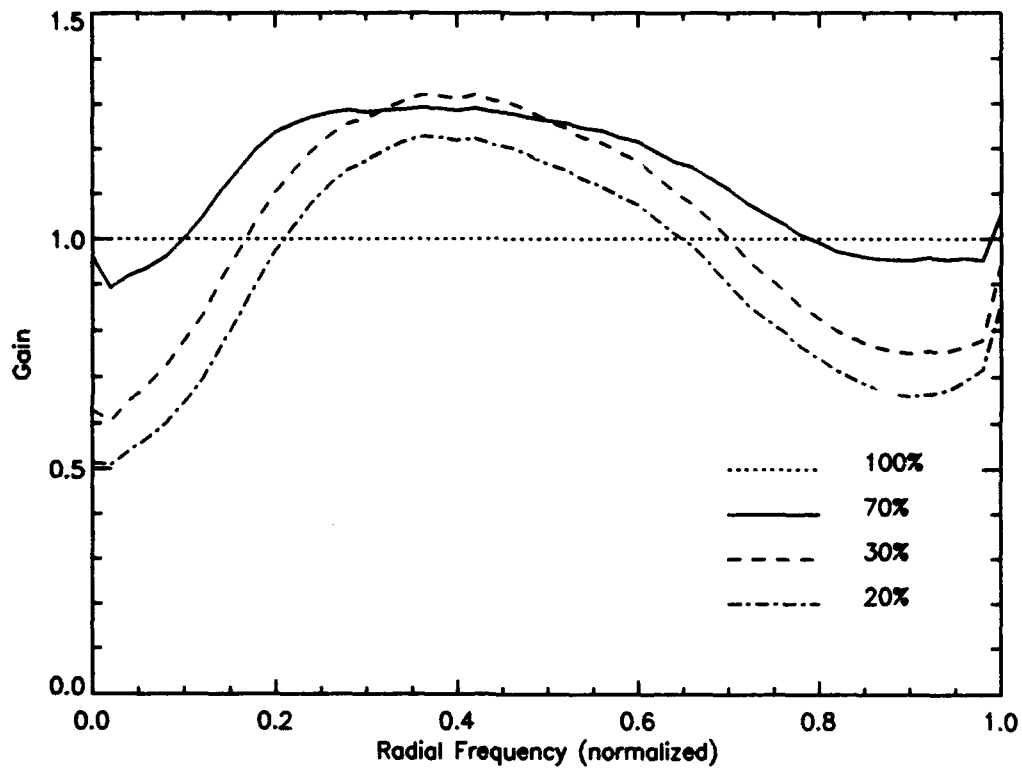


Figure 4.11 Gain Curves for  $S_{S1}$ , Point Source,  $m_v=-1$ ,  $r_o=10\text{cm}$

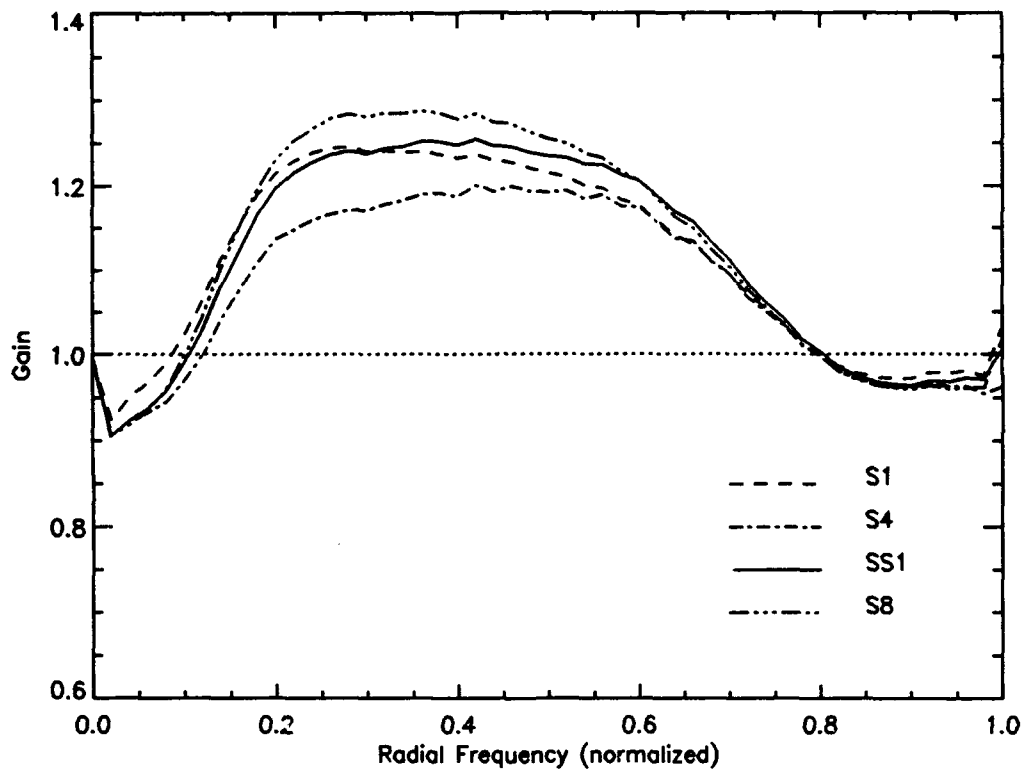


Figure 4.12 Comparison of Gain Curves, 75% Selection Rate, Point Source,  $m_v=-1$ ,  $r_o=10\text{cm}$

### 4.3 Experiment Two

This experiment investigates the performance of frame selection with respect to image signal to noise ratio for an extended object. The performance of the four different quality metrics is compared.

*4.3.1 Simulation Parameters.* The object is a CAD rendering of a space satellite, and is depicted in Figure 4.13. The object was assumed to be approximately 12 meters in length and orbiting at a distance of approximately 500 kilometers. The object's apparent brightness  $m_v$  is -1.0, about the same as the Hubble telescope or the Russian Mir space station. The parameter  $r_o$  was set to 10cm to simulate "average" seeing conditions at a good observatory. Photon limited conditions (no CCD noise) were simulated.

*4.3.2 Simulation Results.* Figure 4.14 compares the performance of the frame selection rule in terms of  $\eta$  for the extended object and the point source from experiment one. The extended object exhibits an  $\eta$  that is 70% less than the point source at the 100% selection rate, and approximately 35% less at the 5% selection rate. However, the extended object does exhibit a 35% improvement in  $\eta$  at the 5% selection rate, as opposed to a 7% improvement for the point source.

Figure 4.15 compares the performance of the frame selection rule in terms of the  $A_G$  metric for the extended object and the point source. The extended object exhibits a maximum  $A_G$  at the 75% selection rate. This maximum is 58% less than the maximum for the point source. Also note that the point where  $A_G$  drops to 1.0 is 50% higher than that for the point source. Figures 4.14, 4.15 illustrate the effects of the object spectrum on signal to noise ratio. Recall from Chapter three that the expression for the short exposure signal to noise ratio for an adaptive optics system free of residual tilt error and using a charge-coupled device (CCD) camera is given by [34]:

$$SNR_{SE}(u, v) = \frac{K |E_{SE}[H(u, v)] O(u, v)|}{\{K + K^2 |O(u, v)|^2 var[H(u, v)] + P \sigma^2\}^{\frac{1}{2}}} \quad (4.12)$$

where  $H$  is the system OTF and  $I$  is the object spectrum. Hence,  $SNR_{SE}$  is a function of the product of the average OTF, and the object spectrum. The object spectrum dependence is due to signal dependent nature of photon noise. In the case of a point source, the object frequency spectrum is a constant for all frequencies, which means that the frequency characteristics of the optical transfer function is the dominant term in the product. For the case of an extended object, the object spectrum falls off much more rapidly than the OTF as a function of frequency, which means that the object spectrum is the dominant factor in determining frequency domain signal to noise ratio, especially at high frequencies. Figure 4.16 demonstrates this relationship by comparing the radially averaged frequency spectrum of the space object illustrated in Figure 4.13, and the average OTF estimated by averaging 100% of the frames collected in the experiment.

Figure 4.17 illustrates the behavior of the gain curves at the 70%, 40%, and 20% selection rates. At the 70% selection rate, there is an improvement in signal to noise ratio over 62% of the diffraction-limited frequency range. The maximum gain occurs at 35% of the diffraction limit and represents a 20% improvement in SNR. There is a 15% loss in SNR at lower frequencies and a 5% loss at high frequencies. At the 40% selection rate, the frequency range where improvement occurs is 30% smaller than the equivalent range at the 70% selection rate. There is a 40% loss of SNR at lower frequencies and a 20% loss at high frequencies. At the 20% selection rate, there is no appreciable gain in signal to noise ratio, and the loss at 80% of the diffraction limit is approximately 35%. These results indicate that the 70% selection rate is the best for maximizing signal to noise ratio.

4.3.3 *Quality Metric Performance.* To determine the relative performance of the four selection rules, consider the gain curves at the 70% selection rate. These curves are depicted in Figure 4.18.  $S_{S1}$  produces the best improvement in signal to noise ratio, with  $S_8$  producing very similar results.  $S_4$  provides the next best performance, although the gain drops off rapidly at higher frequencies.  $S_1$  performs the worst in this case.

4.3.4 *Conclusions.* This experiment demonstrates the effects of the object spectrum on signal to noise ratio. Because of the signal dependent nature of photon noise, the object spectrum has a major impact on frequency domain signal to noise ratio. Hence, extended objects must be investigated separately from point sources. This experiment demonstrates that frame selection can improve the signal to noise ratio of a bright extended object, such as the Hubble telescope or the Mir space station.  $S_{S1}$  performed the best in this experiment.

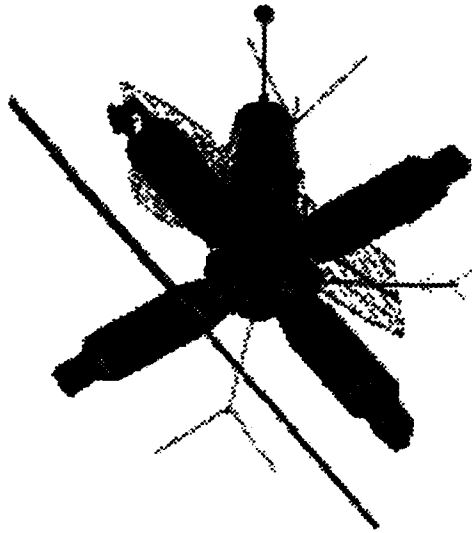


Figure 4.13 Typical Space Object

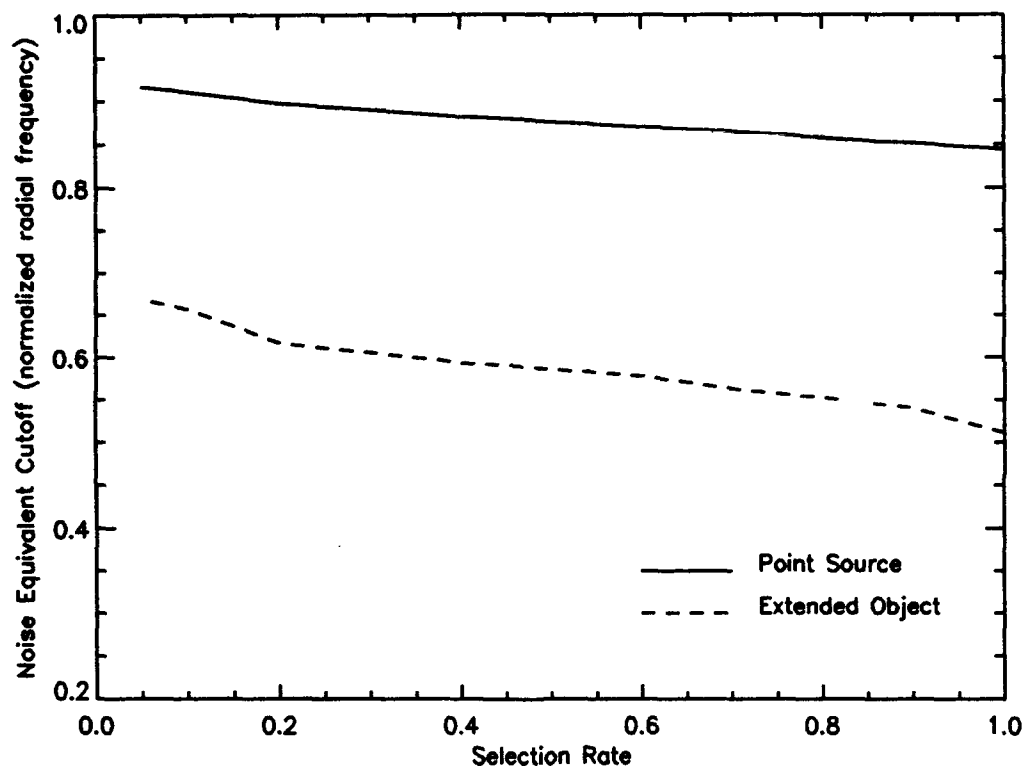


Figure 4.14  $\eta$  vs Selection Rate, Extended Object and Point Source,  $m_v=-1$ ,  $r_o=10\text{cm}$

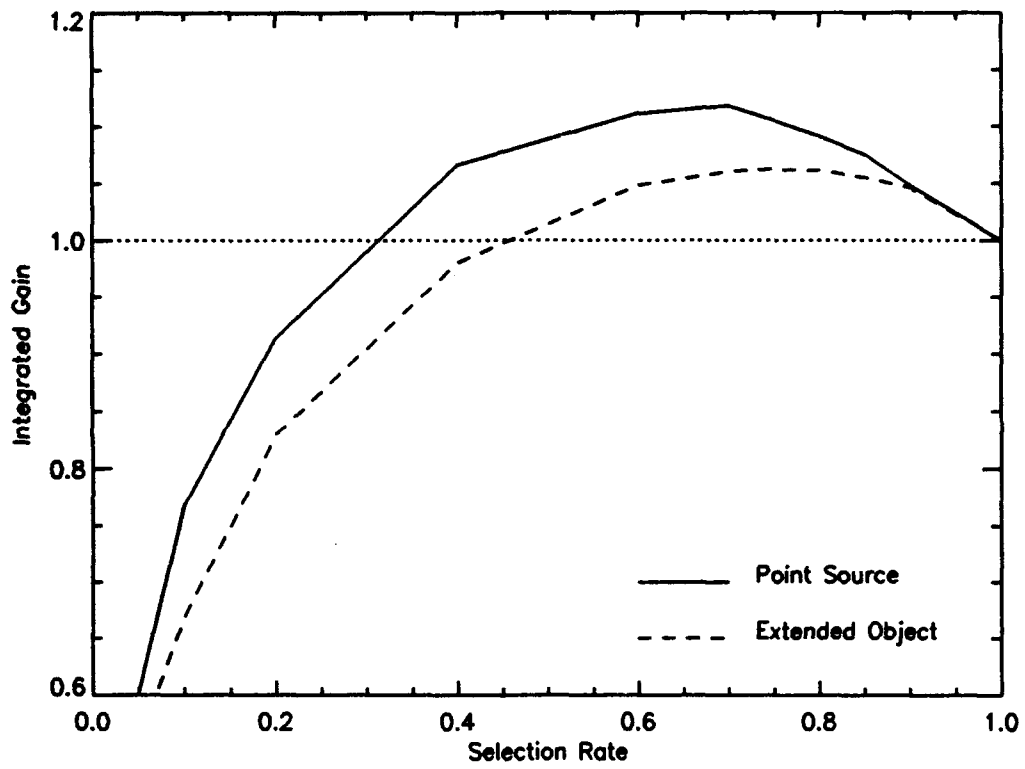


Figure 4.15  $A_G$  vs Selection Rate, Extended Object and Point Source,  $m_v=-1$ ,  $r_o=10\text{cm}$

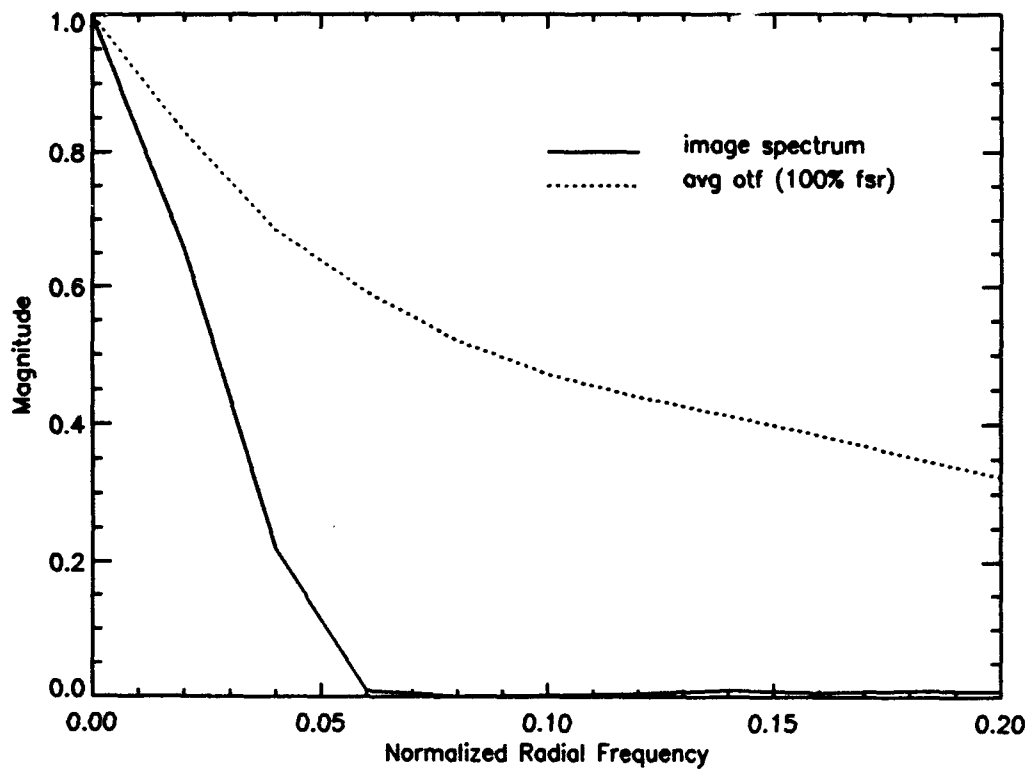


Figure 4.16 Object Spectrum and Average OTF,  $m_v=-1$ ,  $r_o=10\text{cm}$

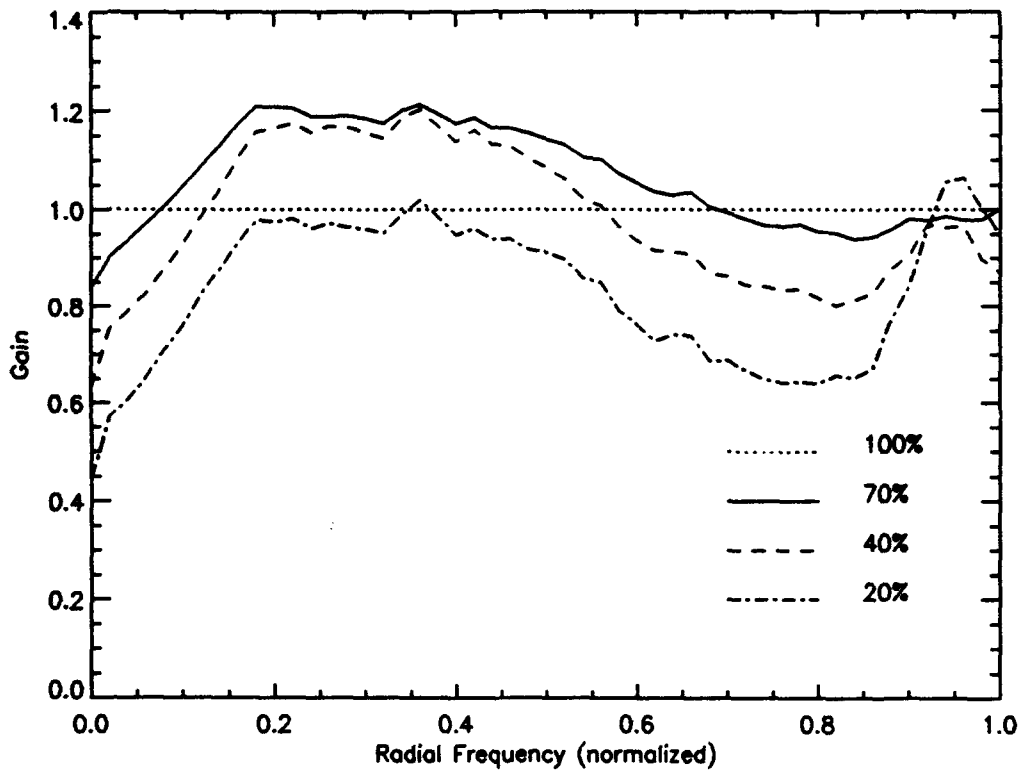


Figure 4.17 Gain Curves, Extended Object,  $m_v = -1$ ,  $r_o = 10\text{cm}$

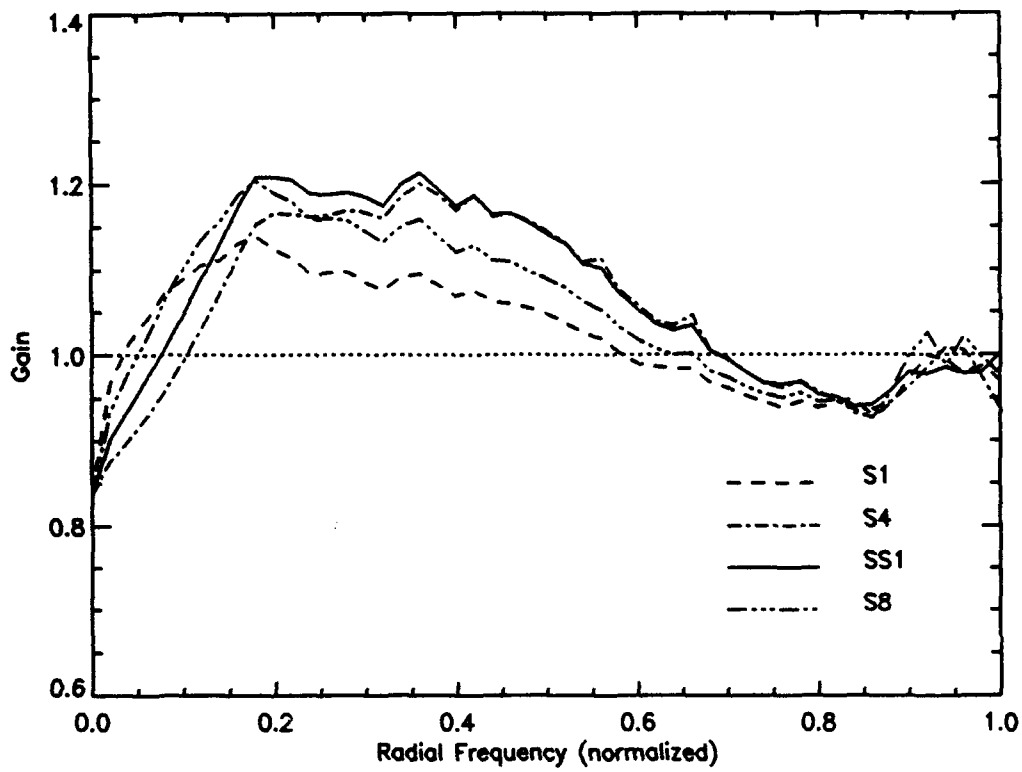


Figure 4.18 Comparison of Gain Curves, Extended Object,  $m_v = -1$ ,  $r_o = 10\text{cm}$

#### 4.4 Experiment Three

This experiment investigates the frame selection technique under different seeing conditions. The performance of the four different quality metrics is compared.

*4.4.1 Simulation Parameters.* The object is the same CAD rendering of a space satellite used in experiment two, and is depicted in Figure 4.13. The object was assumed to be approximately 12 meters in length and orbiting at a distance of approximately 500 kilometers. The object's apparent brightness  $m_v$  is -1.0. The parameter  $r_o$  was set to 7, 10 and 13cm to simulate poor, average, and good seeing conditions at a good observatory. Photon limited conditions (no CCD noise) were simulated.

Figure 4.19 illustrates the effect of seeing conditions on image statistics. First, consider  $\eta$  at the 100% frame selection rate. When  $r_o$  is 7cm,  $\eta$  is 55% less than the case where  $r_o$  is 13cm, and the value at 10cm is 17% less. However, frame selection has a much more pronounced effect on  $\eta$  under poor conditions: at the 5% frame selection rate,  $\eta$  improves by 109% for  $r_o$  equal to 7cm, but only 20% for  $r_o$  equal to 13cm. This is because phase aberrations diminish as seeing conditions improve, which means that photon noise becomes the random process which has the greatest effect on signal to noise ratio. This point is underscored by Figure 4.20.  $A_G$  drops to one at the 35% selection rate for  $r_o$  equal to 7cm as opposed to the 60% selection rate for  $r_o$  equal to 13cm. These results demonstrate that as seeing conditions improve, the gain in signal to noise ratio achieved by discarding the frames most distorted by random phase aberrations is less pronounced than the gain in signal to noise ratio achieved by reducing the effects of photon noise through averaging a large number of frames.

Figure 4.21 illustrates the behavior of the gain curves when  $r_o$  equals 7cm. At the 80% selection rate, gain is achieved over 90% of the diffraction-limited frequency range, with a peak gain of 15% occurring at 15% of the diffraction limit. At the 60%

selection rate, gain is achieved over 70% of the frequency range, with a peak gain of 30% occurring at 35% of the diffraction limit. There is a 10% loss in signal to noise ratio at low frequencies, and a 5% loss at 80% of the diffraction limit. Note that 60% is the selection rate for maximum  $A_G$ . At the 40% selection rate, the range over which gain occurs decreases to 45% of the diffraction limit, and the loss at the higher frequencies increases to 15%. These results demonstrate that the 60% selection rate provides the best overall improvement in signal to noise ratio.

Now consider the behavior of the gain curves when  $r_o$  equals 13cm, depicted in Figure 4.22. The 80% selection rate produces the best results, with a gain in signal to noise ratio occurring over 60% of the diffraction-limited frequency range, with a peak gain of 20% occurring at 20% of the diffraction limit, and a 5% loss as higher frequencies. Note that at the 40% selection rate, the loss at the higher frequencies approaches 25%, again demonstrating the effects of photon noise as subset size decreases.

There is a tendency to misinterpret the data in Figures 4.21 and 4.22. For example, at the 40% selection rate the loss in signal to noise ratio is more pronounced at  $r_o$  equal to 13cm than it is at 7cm. One is tempted to conclude that the composite image generated by averaging the 40% subset collected at 7cm is superior to the one generated from the 40% subset collected at 13cm. This is incorrect. It is important to note that  $G$  is a measure of relative gain that occurs as a result of applying the frame selection rule. Recall from Figure 4.19 that the set collected at 7cm was much worse than the one collected at 13cm. Hence the relative improvement is greater, but the magnitude of the signal to noise ratio is lower. This point is illustrated in Figure 4.23

*4.4.2 Quality Metric Performance.* Consider Figure 4.24, which depicts the performance of the quality metrics at  $r_o$  equal to 7cm, and a 60% frame selection rate.  $S_{S_1}$  and  $S_8$  demonstrate the best performance, with gain occurring over 60%

of the frequency range, and a peak gain of 20% occurring at 20% of the diffraction limit.  $S_4$  is the next best, with slightly poorer performance at low frequencies.  $S_1$  is the worst, with a 10% gain at 20% of the diffraction limit.

Now consider Figure 4.25, which depicts the performance of the quality metrics at  $r_o$  equal to 13cm, and an 80% frame selection rate. Again,  $S_{S1}$  and  $S_8$  demonstrate the best performance, followed by  $S_4$  and  $S_1$ .

*4.4.3 Conclusions.* This experiment demonstrates that the image spectrum signal to noise ratio is governed by two different random processes: random phase aberrations due to atmospheric turbulence, and photon noise, which is intrinsic to the signal. When seeing conditions are poor, random phase aberrations dominate the signal to noise ratio, and frame selection based on sharpness functions can significantly improve the signal to noise ratio by discarding those frames which have been most severely degraded by these phase aberrations. However, as seeing conditions improve, photon noise becomes a greater factor in signal to noise ratio, and the gain in signal to noise ratio achieved by discarding the frames most severely degraded by random phase aberrations is less pronounced than the gain in signal to noise ratio achieved by reducing the effects of photon noise through averaging a large number of frames. The  $S_{S1}$  quality metric produced the best results.

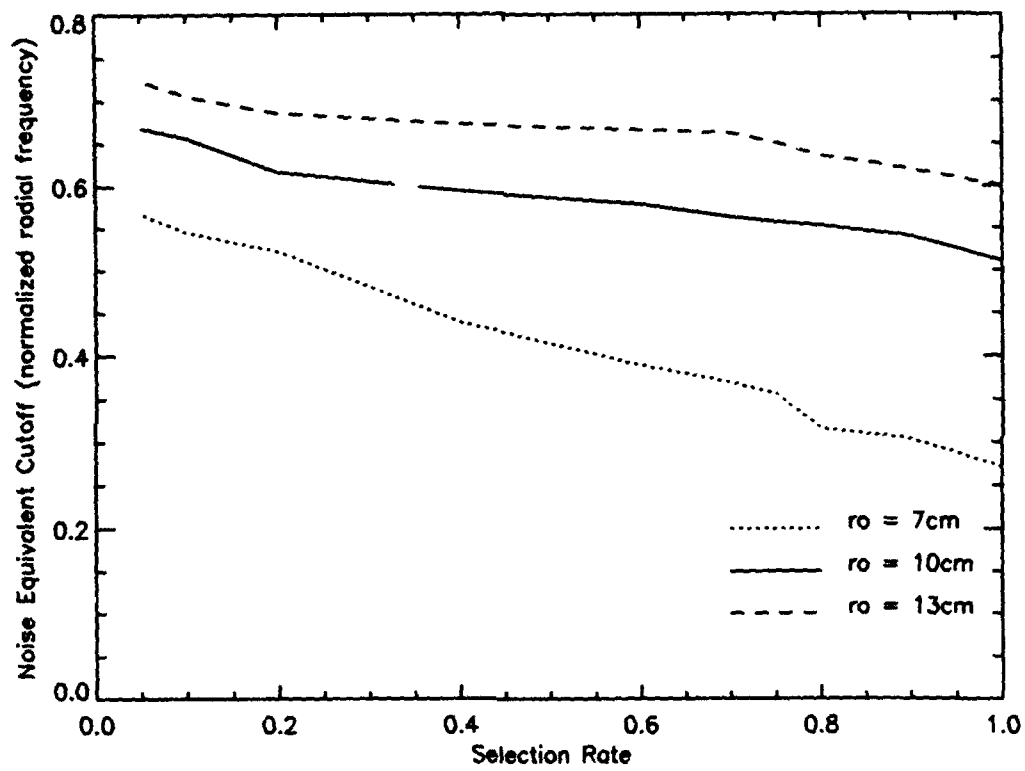


Figure 4.19  $\eta$  vs Selection Rate for Different Seeing Conditions, Extended Object,  $m_v = -1$

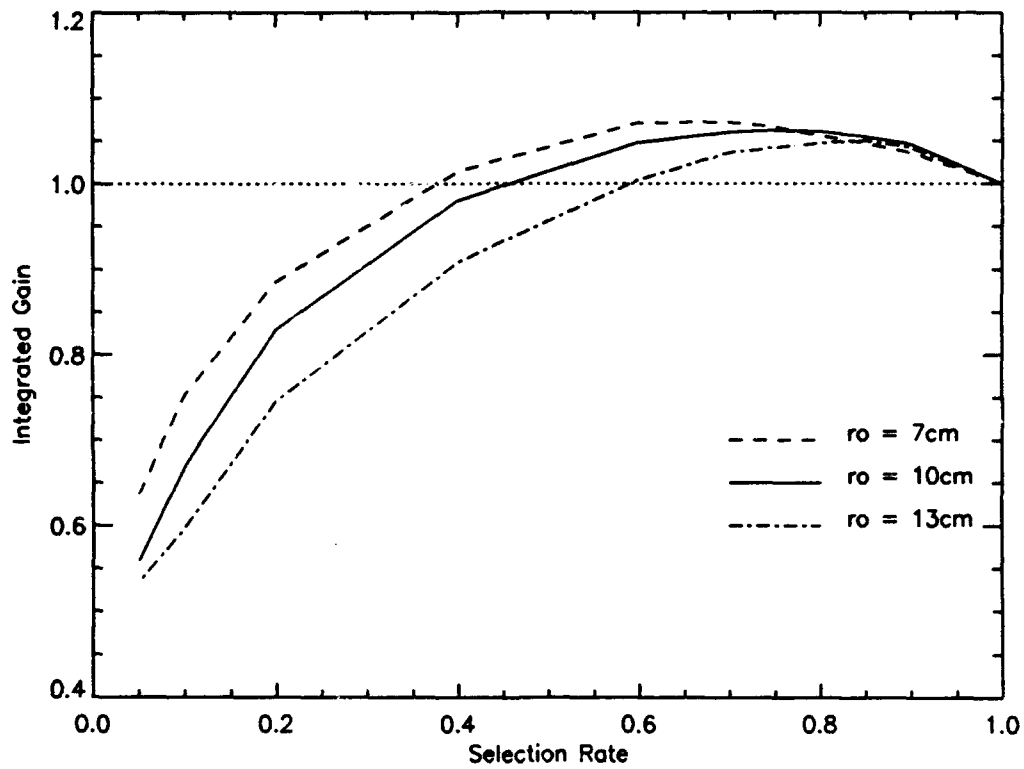


Figure 4.20  $A_G$  vs Selection Rate for Different Seeing Conditions, Extended Object,  $m_v = -1$

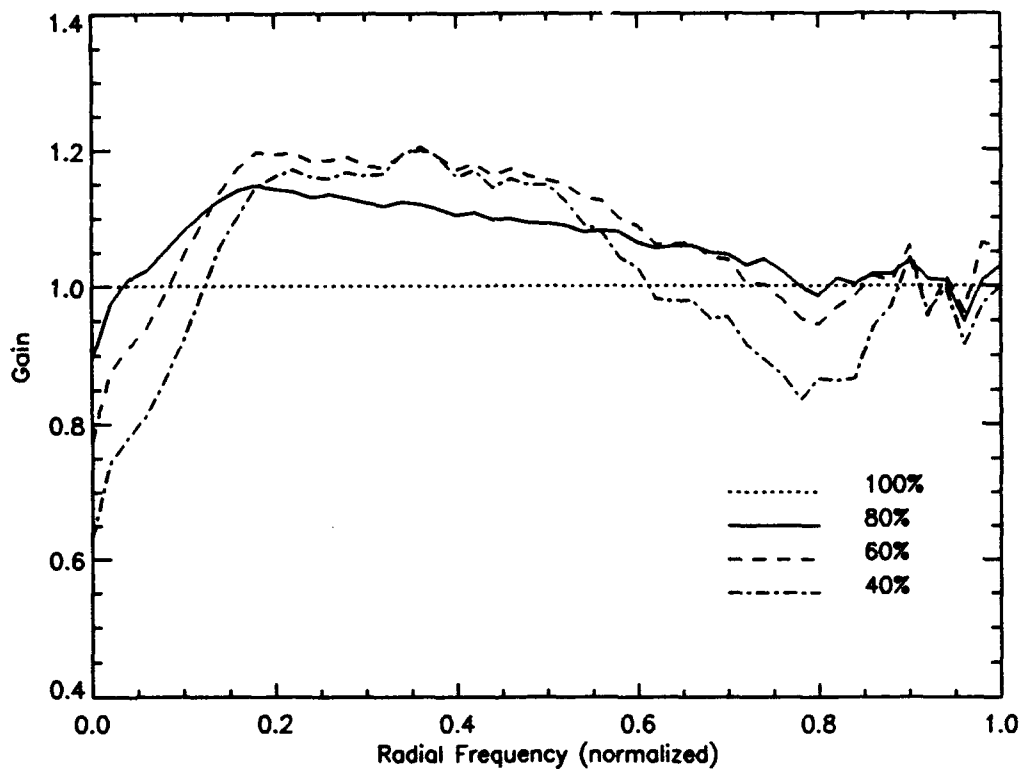


Figure 4.21 Gain Curves for Extended Object,  $r_o=7\text{cm}$ ,  $m_v=-1$

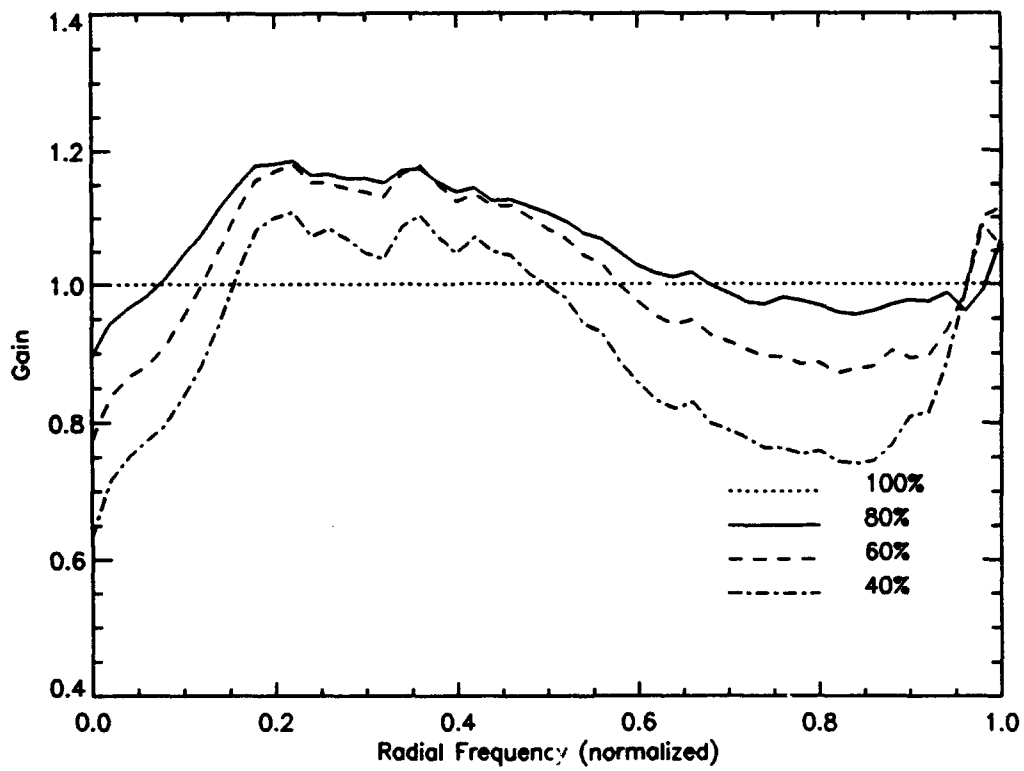


Figure 4.22 Gain Curves for Extended Object,  $r_o=13\text{cm}$ ,  $m_v=-1$

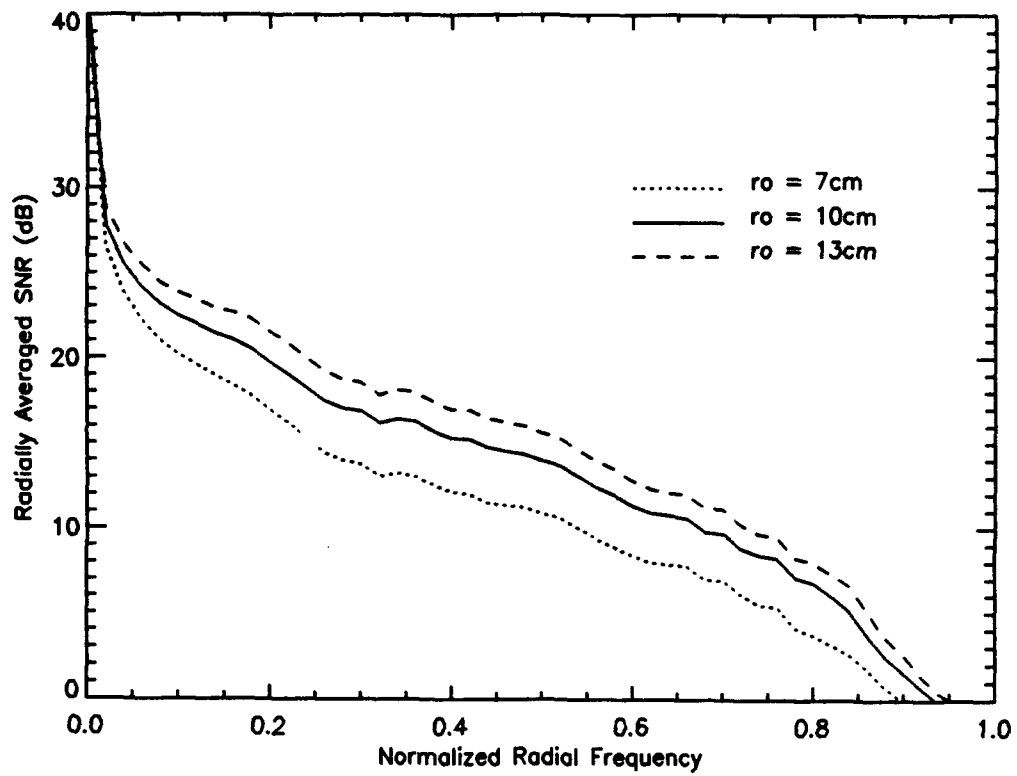


Figure 4.23 SNR at 40% Selection Rate for Different Seeing Conditions, Extended Object,  $m_v = -1$

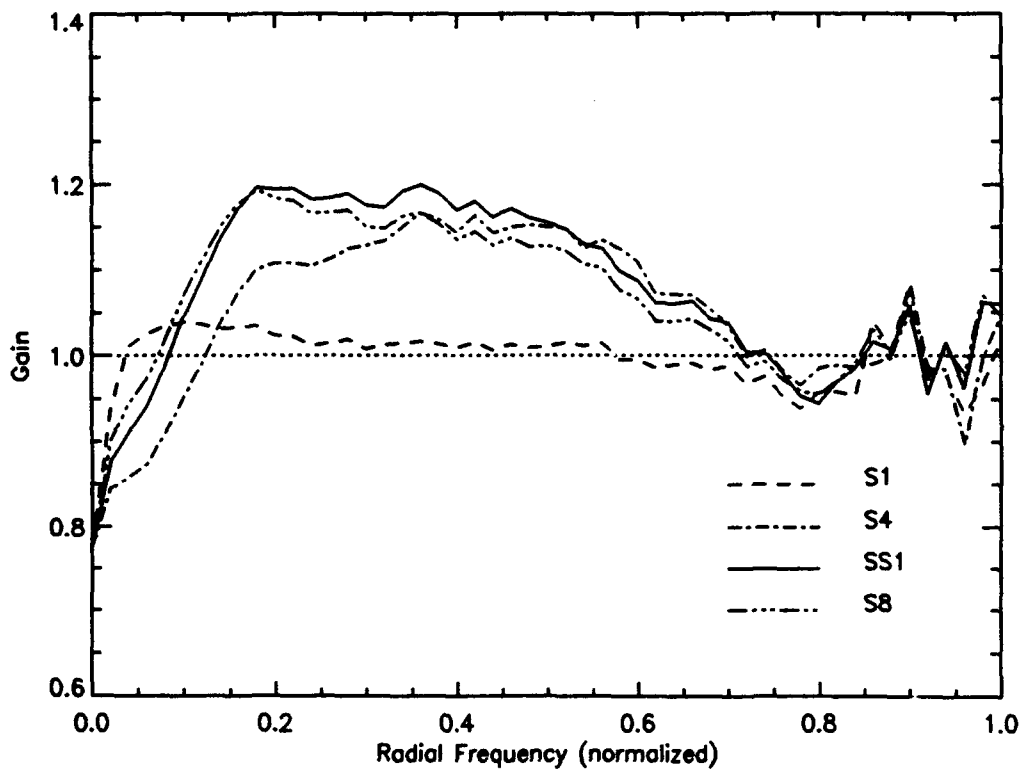


Figure 4.24 Comparison of Gain Curves at 60% Frame Selection Rate, Extended Object,  $m_v = -1$ ,  $r_o = 7\text{cm}$

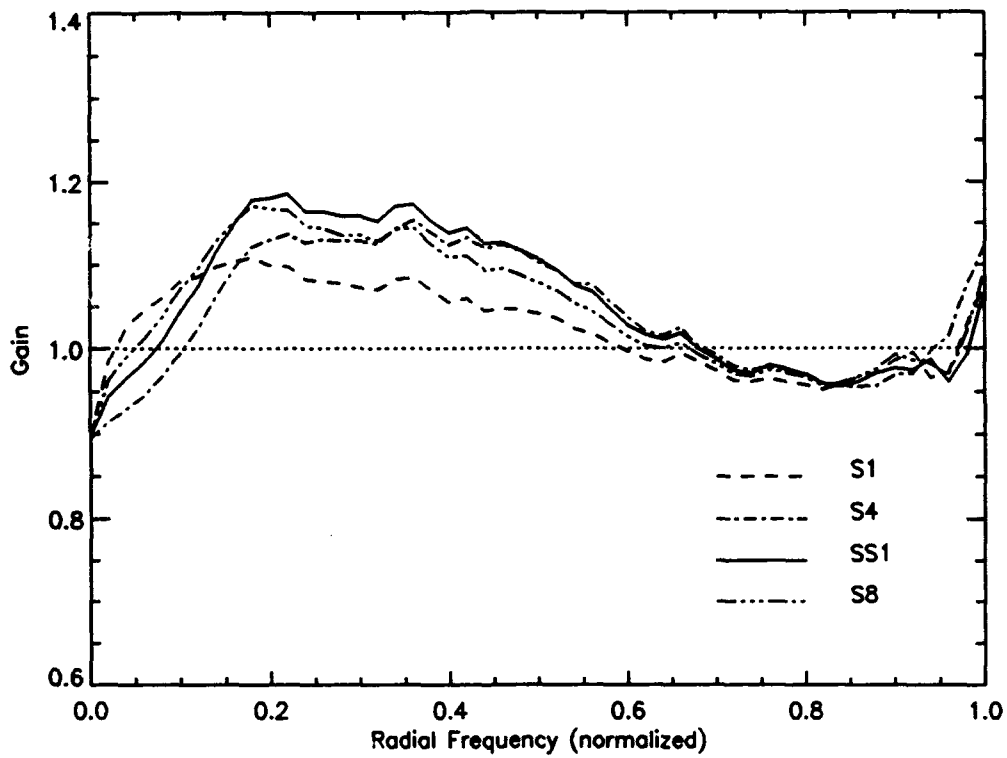


Figure 4.25 Comparison of Gain Curves at 80% Frame Selection Rate, Extended Object,  $m_v = -1$ ,  $r_o = 13\text{cm}$

## 4.5 Experiment Four

This experiment investigates the effects of image brightness on the performance of the frame selection technique. Results for both a point source and an extended object are presented. The performance of the four different quality metrics is compared.

*4.5.1 Simulation Parameters.* Both the extended object and a point source were simulated. The extended object was assumed to be approximately 12 meters in length and orbiting at a distance of approximately 500 kilometers. The apparent brightness in both cases is +3.0, equivalent to a dim satellite (recall that in the visual magnitude system, a larger value indicates a dimmer object). The results are compared to the results previously obtained in experiments one and two. Photon limited conditions (no CCD noise) were simulated.

*4.5.2 Simulation Results.* First, consider the case of a point source. Figure 4.26 illustrates the effects of image brightness on  $\eta$ . There is very little difference in performance.  $\eta$  decreases by 1% at the 100% selection rate, and by 2% at the 5% frame selection rate.

Figure 4.27 illustrates the effects of image brightness on  $A_G$ . Again, there is very little difference in performance. The point where  $A_G$  drops to one is 5% higher when  $m_v$  equals +3.

Next, consider the gain curves for the  $S_{S1}$  metric. These curves are depicted by Figure 4.28 and are almost identical to the curves depicted in Figure 4.11. These results indicate that point sources are not sensitive to changes in light levels in the range  $[-1, +3]$ .

Now consider the same experiment, substituting the space object for the point source. Figure 4.29 illustrates the effects of image brightness on  $\eta$  for the case of an extended object. In contrast to the point source, the change in  $m_v$  has a marked

impact on  $\eta$ . At the 100% selection rate,  $\eta$  is 50% less, and at the 5% selection rate  $\eta$  is 52% less.

Next, consider  $A_G$ . Figure 4.30 indicates that frame selection will not produce a net gain in signal to noise ratio at  $m_v$  is equal to +3. Figure 4.31 demonstrates this conclusion. These results are very significant, because they demonstrate that the number of photo events collected by the adaptive optics system imposes a fundamental limit on the performance of the frame selection technique. To establish the performance limit for the 1 meter adaptive optics system simulated in this study,  $A_G$  was determined using the  $S_{S1}$  selection rule and a 75% selection rate for values of  $m_v$  between -1 and +4. Figure 4.32 indicates that the frame selection technique will produce a net gain in signal to noise ratio for an extended object when  $m_v$  is less than +2.3. However, it must be stressed that this result is only applicable to the adaptive optics system simulated in this experiment. Note that doubling the size of the aperture will increase the light gathering power of the device by a factor of four, which translates into roughly one and a half steps in apparent magnitude.

*4.5.3 Conclusions.* This experiment is perhaps the most significant one conducted in this investigation, because it demonstrates that the number of photo events imposes a fundamental limitation on the performance of the frame selection technique when processing images of extended objects. As the average number of photo events decreases, the effects of photon noise become more pronounced. In general, there is a point where photon noise - rather than random phase aberrations - becomes the noise process which dominates the signal to noise ratio, and reducing the effects of photon noise requires the largest possible set of images for the averaging process. Under these conditions, frame selection based on sharpness functions is ineffective, since the gain in signal to noise ratio achieved by discarding those frames which exhibit the greatest amount of phase aberration is less than the gain achieved by averaging all of frames to reduce the effects of photon noise. For the adaptive

optics system and the extended object simulated in this experiment, this point occurs when the visual magnitude  $m_v$  of the extended object is dimmer than +2.3.

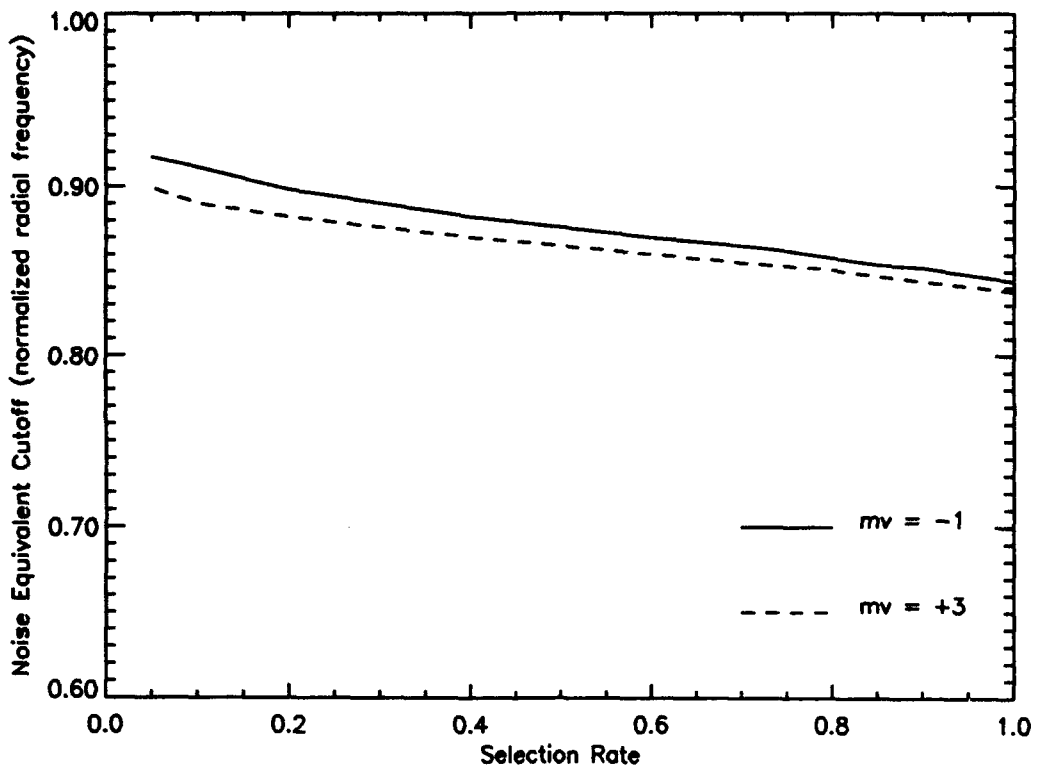


Figure 4.26  $\eta$  vs Frequency, Point Source,  $m_v = -1, +3$ ,  $r_o = 10\text{cm}$

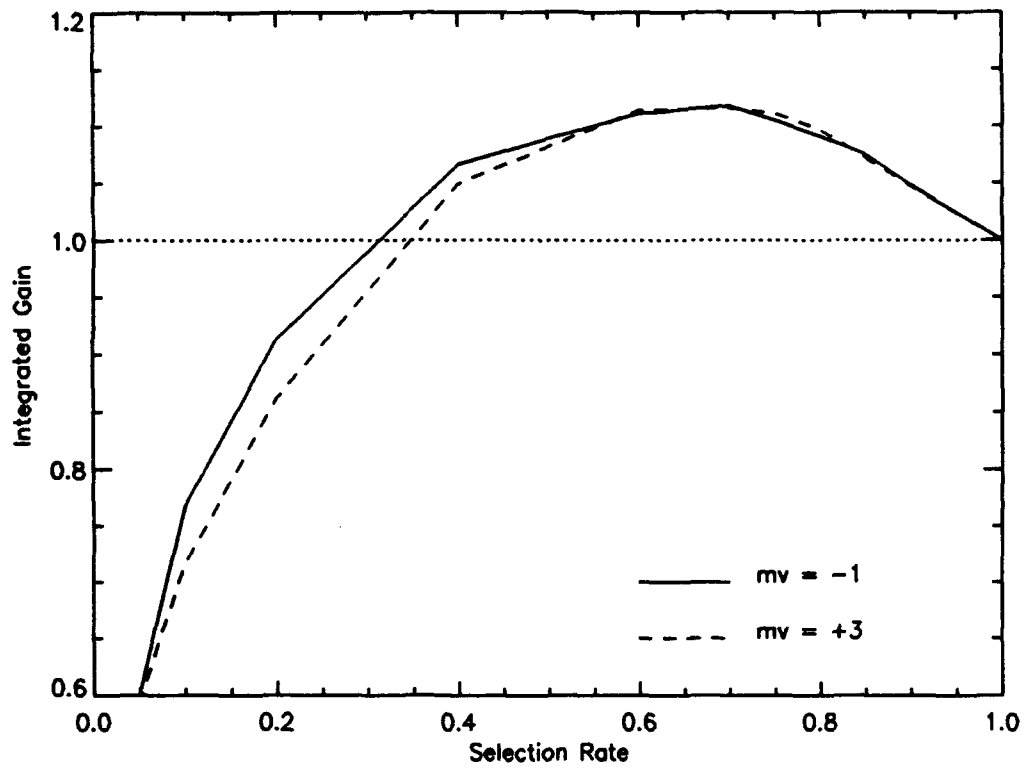


Figure 4.27  $A_G$  vs Frequency, Point Source,  $m_v = -1, +3$ ,  $r_o = 10\text{cm}$

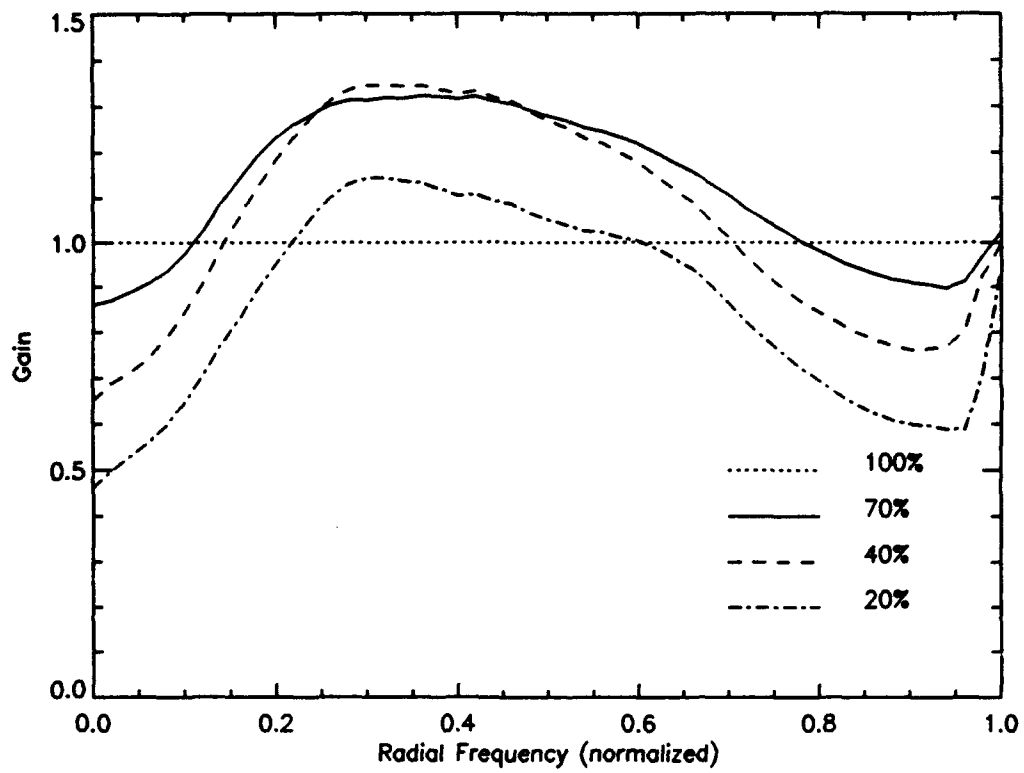


Figure 4.28 Gain Curves, Point Source,  $m_v=+3$ ,  $r_s=10\text{cm}$

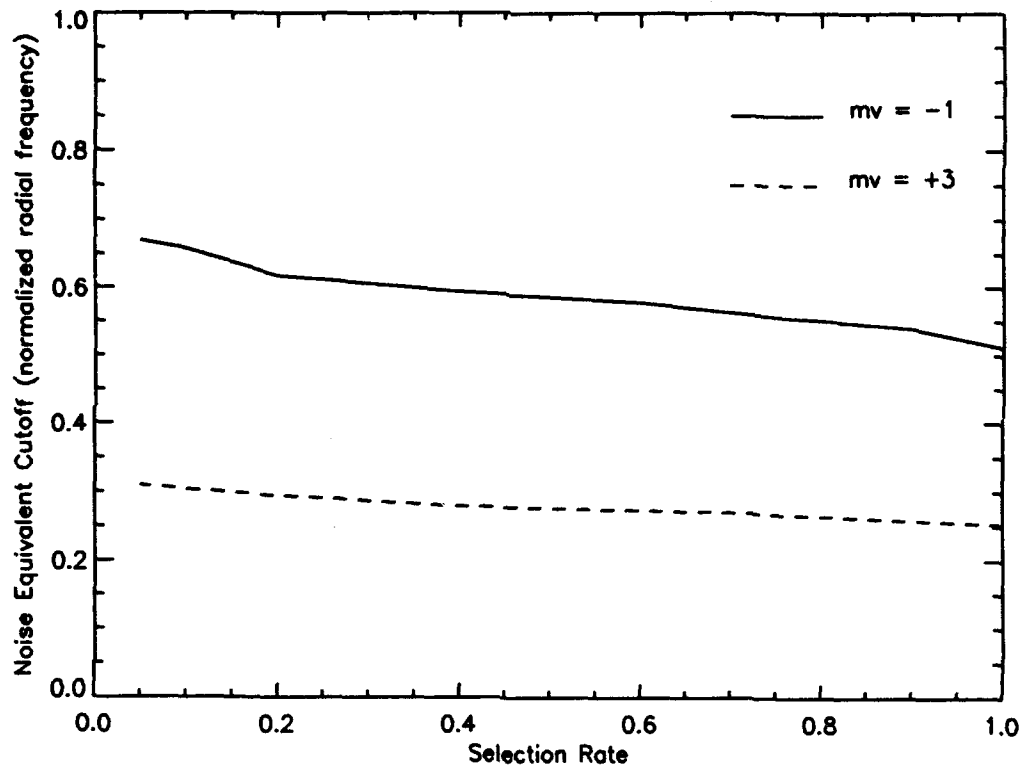


Figure 4.29  $\eta$  vs Selection Rate, Extended Object,  $m_v = -1, +3$ ,  $r_o = 10\text{cm}$

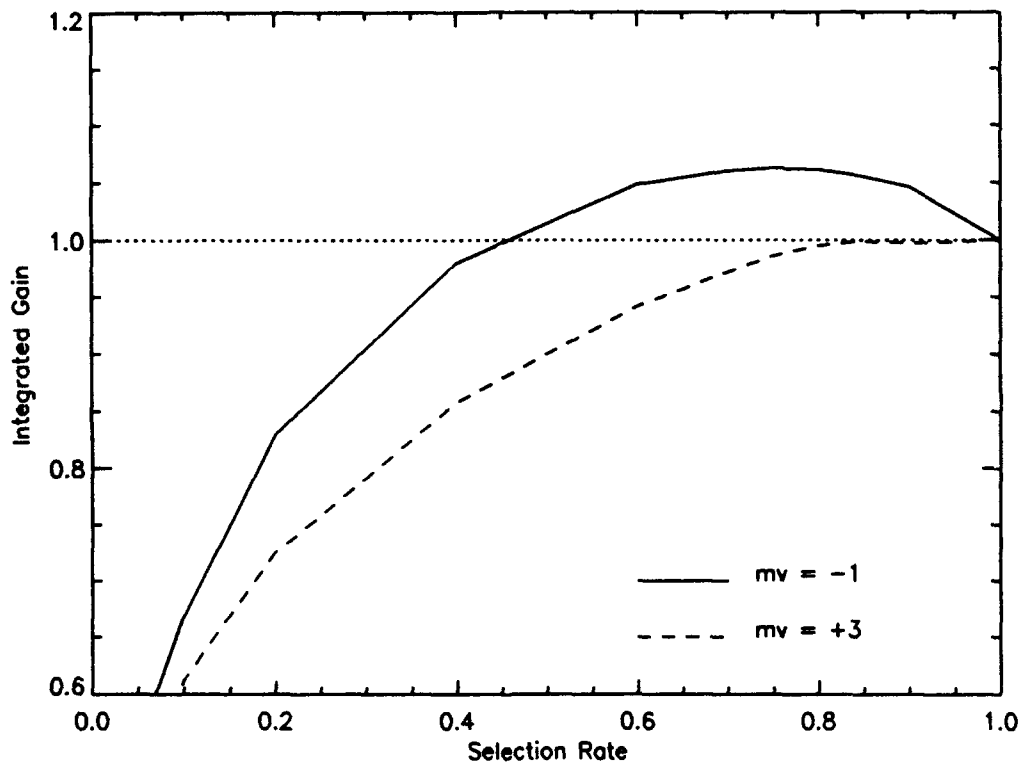


Figure 4.30  $AG$  vs Selection Rate, Extended Object,  $m_o = -1, +3$ ,  $r_o = 10\text{cm}$

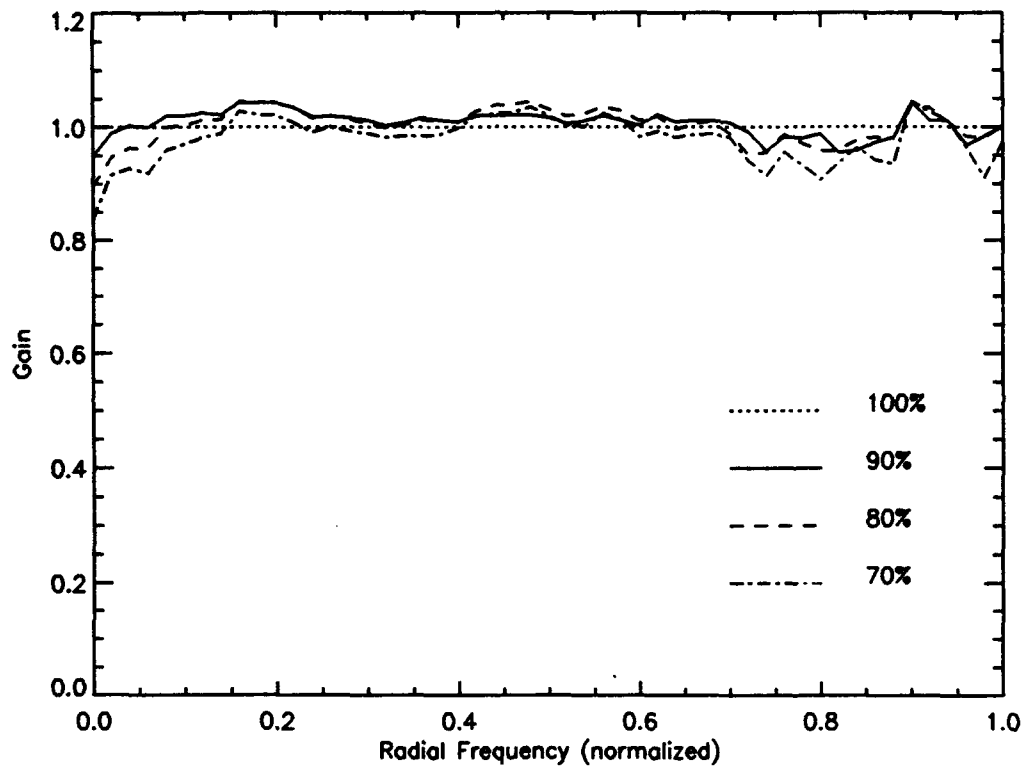


Figure 4.31 Gain Curves, Extended Object,  $m_v = -1, +3$ ,  $r_o = 10\text{cm}$

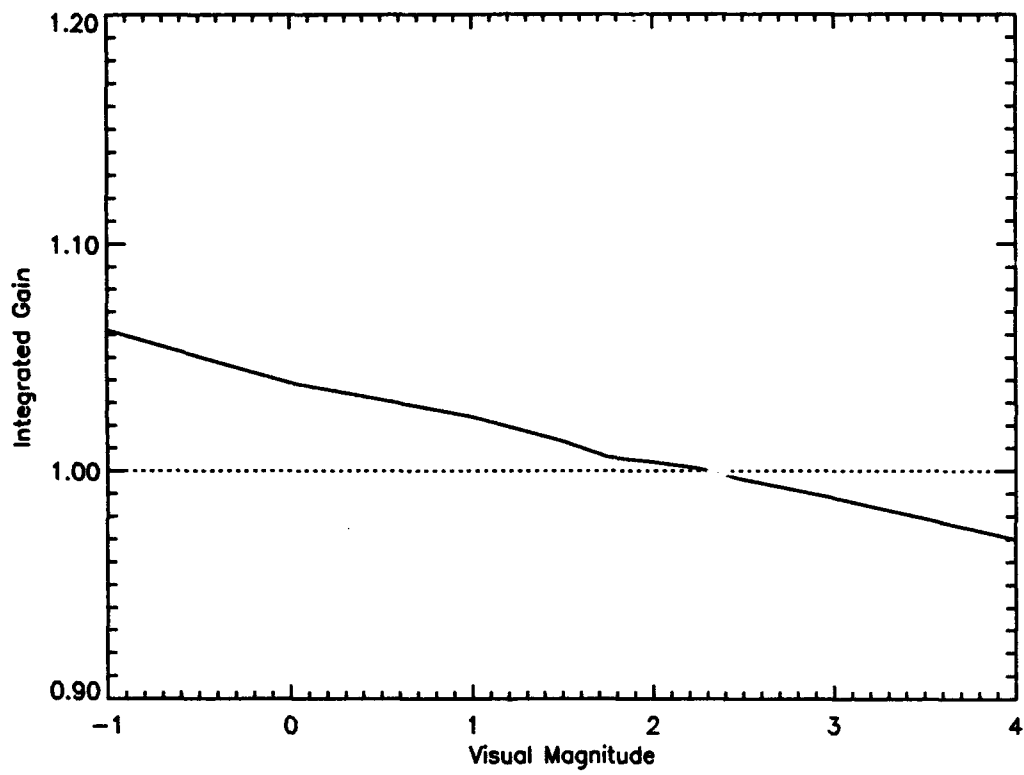


Figure 4.32  $A_G$  vs  $m_v$ , Extended Object,  $r_o=10\text{cm}$

## 4.6 Experiment Five

All four previous experiments assumed photon-limited conditions. This experiment investigates the effects of CCD camera read noise on image signal to noise ratio.

**4.6.1 Simulation Parameters.** A 79 by 79 detector pixel grid was simulated. This grid represents the minimum grid necessary to meet Nyquist sampling requirements (see Appendix one). The pixel noise variance  $\sigma^2$  was set to 15 or 30 electrons per pixel, representing good and poor detection devices. The object was a point source of brightness  $m_v = +3$ .  $r_o$  was set to 10cm.

**4.6.2 Simulation Results.** Figure 4.33 illustrates the effects of camera read noise on subset statistics.  $\eta$  decreases 2% when  $\sigma^2$  is 15, and 4% when  $\sigma^2$  is 30. Figure 4.34 illustrates the integrated gain curves for the case of camera read noise. Again, there is very little difference in performance. Figure 4.35 depicts gain curves for the case of camera read noise with variance  $\sigma^2$  equal to 30. The results are almost identical to the curves depicted in Figure 4.28.

These results indicate that CCD read noise will not limit the performance of the frame selection technique, as long as the pixel grid size is kept to a size in line with sampling requirements, and the detector demonstrates good noise characteristics.

**4.6.3 Quality Metric Performance.** Figure 4.36 depicts gain curves for the different quality metrics for the case of camera read noise with variance  $\sigma^2$  equal to 30.  $S_8$  performs the best, followed by  $S_{S1}$  and  $S_1$ .  $S_4$  exhibited the worst performance.

**4.6.4 Conclusions.** CCD read noise degrades the signal to noise ratio, but it does not interfere with the frame selection rule's ability to find the right frames for averaging. Read noise in the range of commercially available high quality

•  
•

devices does not place a fundamental limit on the performance of the frame selection technique.

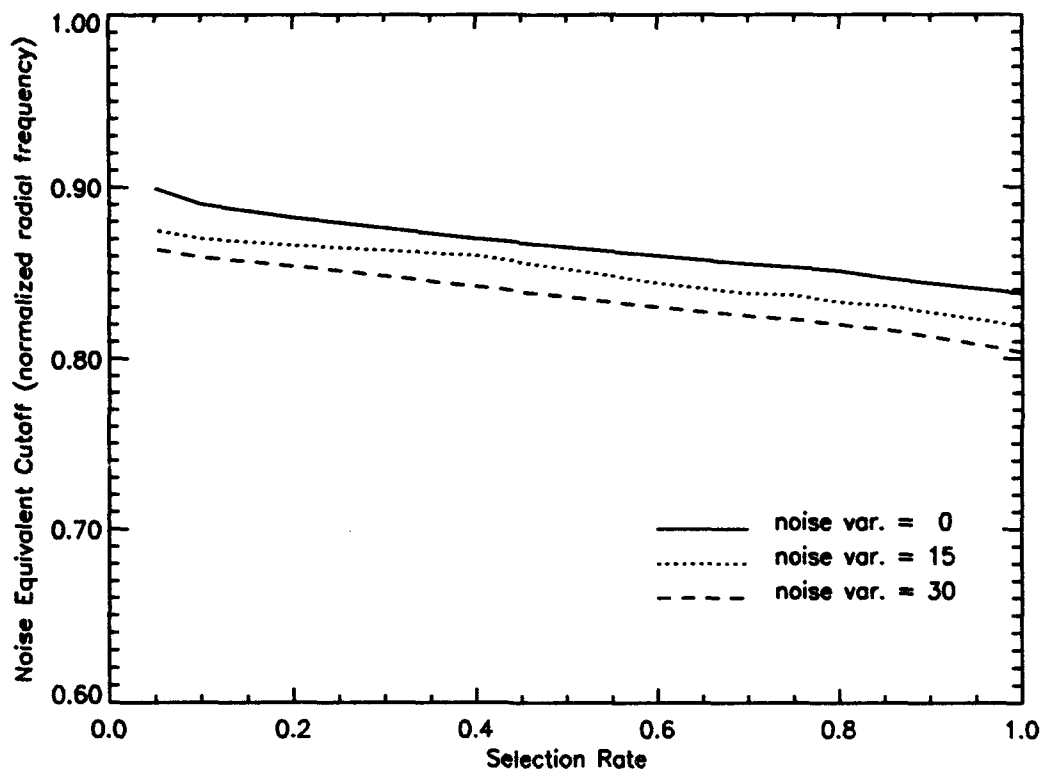


Figure 4.33  $\eta$  vs Frequency, CCD Noise Case, Point Source,  $m_v=+3$ ,  $r_o=10\text{cm}$

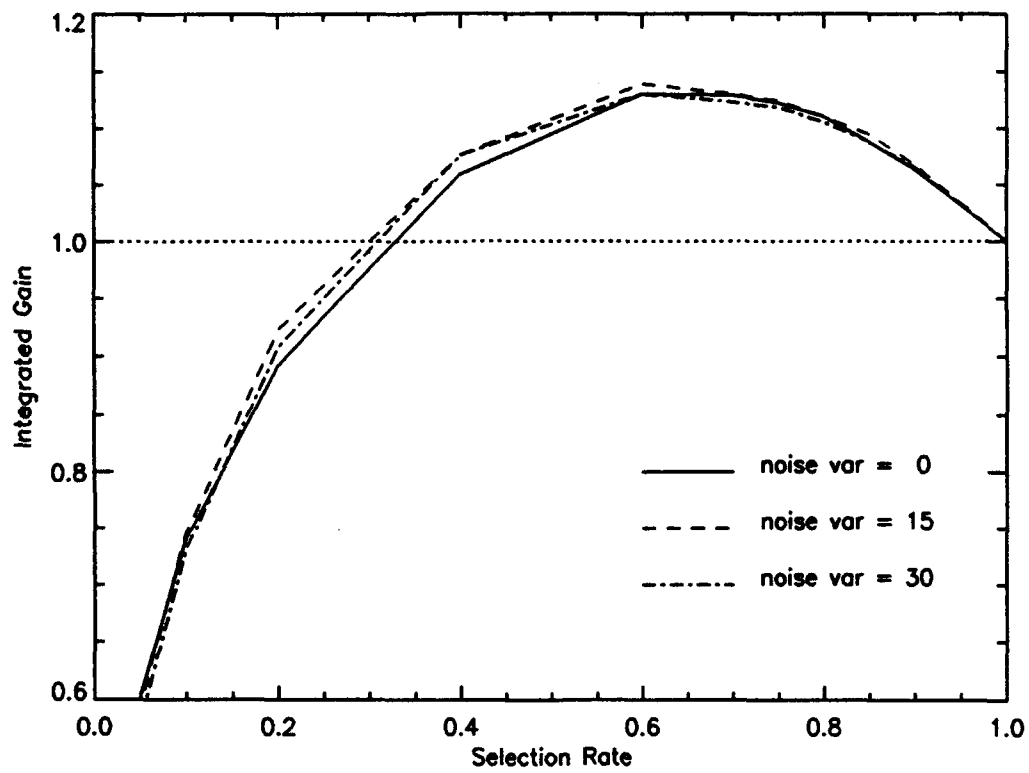


Figure 4.34  $A_G$  vs Frequency, CCD Noise Case, Point Source,  $m_v=+3$ ,  $r_o=10\text{cm}$

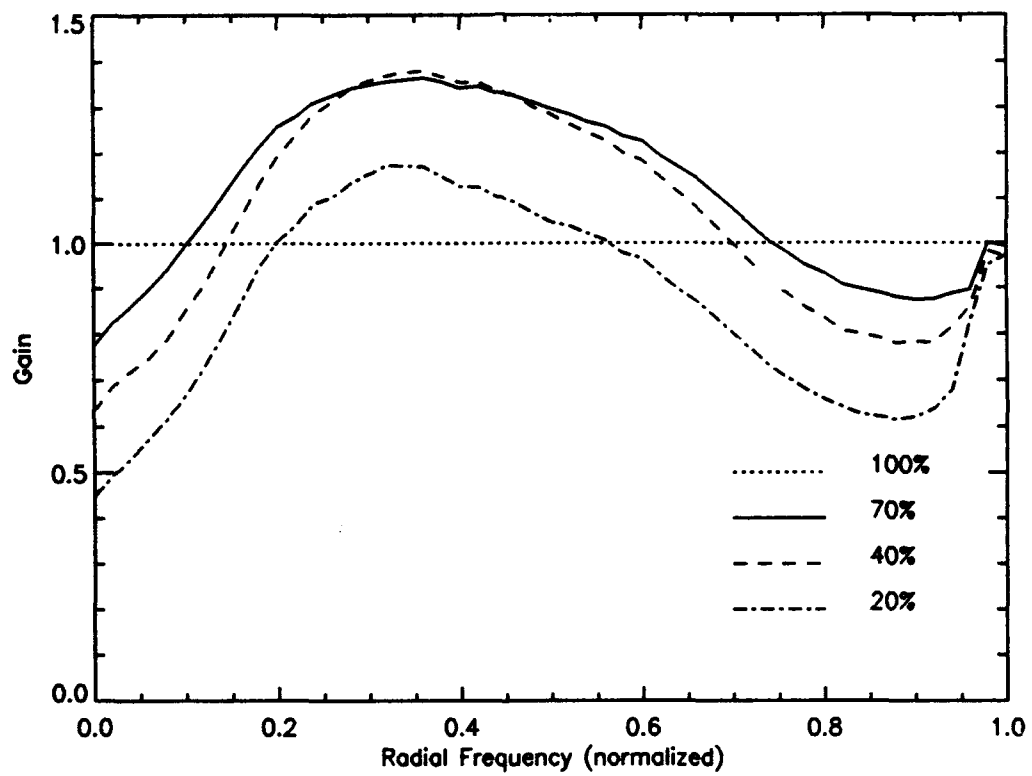


Figure 4.35 Gain Curves, CCD Noise Case, Point Source,  $m_v=+3$ ,  $r_o=10\text{cm}$

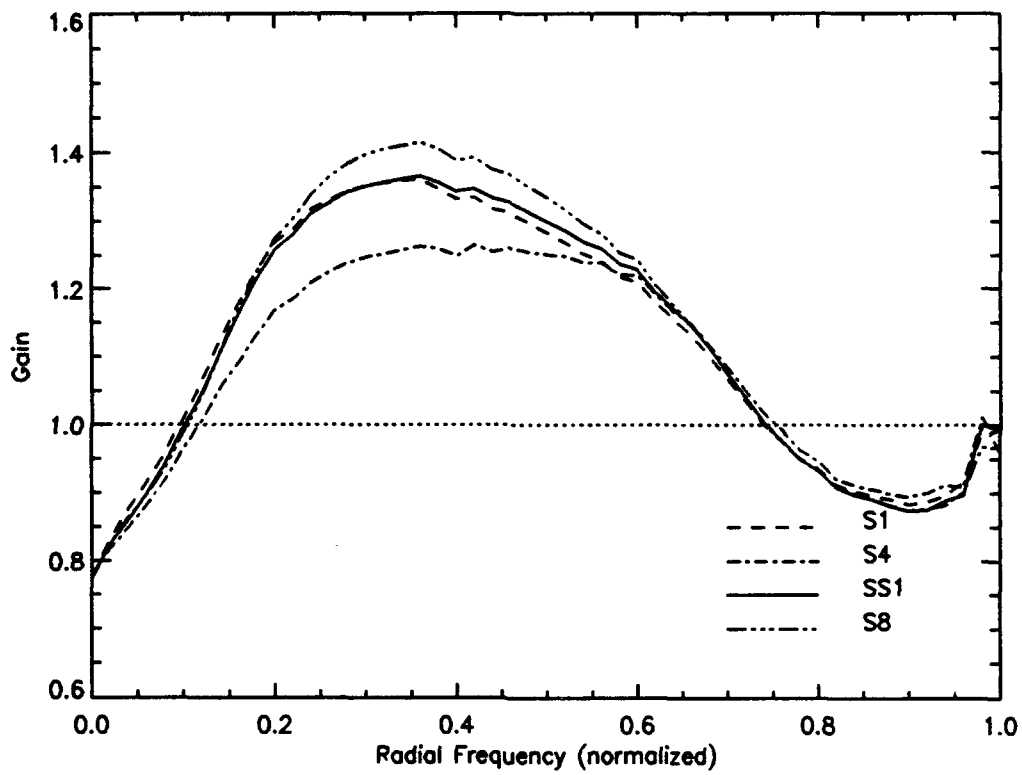


Figure 4.36 Comparison of Gain Curves, CCD Noise Case, Point Source,  $m_v=+3$ ,  $r_o=10\text{cm}$

#### 4.7 Summary

This chapter establishes the hypothesis that frame selection can be used to enhance images produced by Air Force adaptive optics systems. It was shown that frame selection has two important effects on image quality. First, application of the frame selection rule broadens the optical transfer function and narrows the point spread function, which reduces image blurring. Second, frame selection changes the statistics of a set of short exposure images by improving the image spectrum estimate and decreasing the variance, resulting in a net gain in image spectrum signal to noise ratio. There is generally an optimal frame selection rate - typically 60-75% - where the gain in signal to noise ratio is maximized. Beyond this point, any additional improvement in the subset statistics is insufficient to compensate for diminished noise reduction due to averaging a smaller number of images. Hence, there is generally a trade-off between image sharpness due to narrowing of the point spread function and signal to noise ratio, which means one can minimize the effects of blurring at the expense of more pronounced noise, especially at high frequencies. The experiments demonstrate that the signal to noise ratio of an extended object behaves very differently from that of a point source, due to the signal dependent nature of photon noise. It was established that photon noise imposes the fundamental limitation on the performance of the frame selection technique. For the extended object and the adaptive optics system simulated in the experiment, the object must be brighter than  $m_v$ , equal to +2.3 for frame selection to work. Finally, of the four quality metrics investigated in this thesis, the  $S_{S1}$  metric consistently produced the best results.

## *V. Conclusions and Recommendations*

### *5.1 Introduction*

The idea for this thesis began with the observation that in a large set of short exposure images collected by an adaptive optics system, some of the images are much better than others. Since the average of this image set is then processed by reconstruction techniques such as inverse filtering or bispectrum methods to produce a single, high quality image, it was reasonable to hypothesize that image quality could be improved by processing the average of the better images in the set. The results of this thesis prove that this hypothesis was correct. This chapter presents a brief summary of what was accomplished by this research effort, provides some specific recommendations to the end user, and ends with recommendations for future research into this area.

### *5.2 Conclusions*

1. Frame selection significantly increases the amount of noise reduction achieved through averaging a collection of short exposure images. The use of sharpness functions as selection rules can result in a 10-15% improvement in signal to noise ratio for modest selection rates of 60-75% of the entire set. There generally exists an optimal selection rate where the gain in signal to noise ratio is maximized. In terms of spatial frequency, the peak improvement in signal to noise ratio occurs at approximately 40% of the diffraction-limited frequency cutoff. Applying frame selection beyond the 60% selection rate will reduce blurring by narrowing the point spread function, however, the cost of such improvement will be an overall loss in signal to noise ratio. At low selection rates (10-20%), one can expect a sharper, but noisier image.

2. The statistics of point sources and extended objects behave quite differently when the frame selection rule is applied. It was observed that image brightness has

a much more drastic effect on the performance of the frame selection technique when applied to an extended object than it does when applied to a point source. For the one meter telescope simulated in this investigation, the limit of performance for an extended object was determined to be a visual magnitude of +2.3. Since the visual magnitude of most space objects of interest to the Air Force are between -1 and +3, this means that the technique may not improve the images of some of the dimmer space objects. However, it should be noted that the Air Force has plans for larger adaptive optics systems, and increasing the size of the aperture will increase the number of photo events collected by the device. For example, doubling the size of the aperture increases the number of photo events by a factor of four, which equates to one and a half steps in visual magnitude. Hence, the limitation reported in this investigation will be reduced in degree as the Air Force transitions to larger adaptive optics devices.

3. Seeing conditions and CCD read noise affect the overall performance of the technique, however, they are not as critical as the image brightness level.

4. The  $S_{S1}$  quality metric outperformed the other quality metrics evaluated in this investigation, and should be considered the quality metric of choice for frame selection.

### *5.3 Recommendations to the User*

1. The appropriate frame selection rate depends on the characteristics of the entire post-processing scheme used to produce the final product, and the end user's requirements. In the case where image averaging is used as a stand-alone post-processing technique with no subsequent reconstruction processing, then a fairly low (10-20%) frame selection rate will yield a sharper, but noisier image. If the end-user is a human operator, then this is probably the best compromise, since the human visual system is fairly tolerant of uncorrelated noise, and most people would rather look at a sharp, rather than blurred, image. In the case where additional reconstruction

processing is performed on the result of the averaging process, then the effects of noise on the performance of that reconstruction technique must be taken into account. For example, it is well known that the inverse filter amplifies noise effects [2]. Hence, when using the inverse filter, the best frame selection rate would be 60-75%, which maximizes signal to noise ratio. The noise characteristics of other reconstruction techniques - such as bispectrum processing - are not as well understood, however, the safest approach would be to use frame selection to maximize signal to noise ratio, and then rely on the reconstruction technique to deblurr the image.

2. The  $S_{S1}$  metric performs better than the others evaluated in this investigation, and should be used in the frame selection process. Although it is the most complex in terms of computational requirements, this should not present a problem in a post-processing environment.

#### *5.4 Recommendations for Further Research*

1. It should be noted that the issue of optimality was not addressed by this thesis. It is not known whether or not the subsets chosen by the frame selection rules investigated by this thesis are optimal in the sense of achieving the maximum gain in signal to noise ratio. An effort to find an optimal frame selection rule could prove to be quite challenging.

2. The simulation results consistently demonstrate that most of the gain in signal to noise ratio is in the mid-frequency range, usually from 10% to 80% of the diffraction limit. The effects of changes in signal to noise ratio in these frequencies on subjective human assessments of image quality is poorly understood. A psychometric study of human assessment of image quality in response to changes in frequency domain signal to noise ratio could lead to a more precise determination of the optimum frame selection rate. Such a study should also include an evaluation of the trade-off between signal to noise ratio and image blurring.

3. This thesis establishes the fact that frame selection is light level dependent for extended objects. The results demonstrate that when there is a limited number of photo events, every frame in the set is needed to reduce the effects of photon noise. This suggests an alternate approach: instead of discarding the poorer frames in the set, perhaps it would be more advantageous to weight each frame according to its quality. If the weighted sum was then averaged, this might preserve the photon noise reduction properties of the entire set while also narrowing the point spread function.

## *Appendix A. CCD Camera Model*

### *A.1 Introduction*

A charge coupled device (CCD) is a semiconductor device that can store an electric charge at one point, and then transfer and detect it at another point on demand [38]. One way to input a charge into a CCD is via the absorption of photons at the device surface. Hence, it is possible to generate an electronic data stream representing an image by creating a two dimensional array of a large number of CCD photo detectors to register the photon flux at many different spatial points, and then periodically reading out the charge accumulated by each photo detector. The individual photo detectors in such an array are called pixels. Such imaging systems are known as CCD cameras, and they are widely used in both military and civilian applications. CCD cameras introduce noise into the image, and the effects of this noise must be accounted for in any realistic simulation of an adaptive optics system. This appendix provides a detailed development of the CCD noise model developed during this thesis and incorporated into the HYSIM simulation package. The first section describes the determination of the optimum array size for minimizing the amount of noise introduced into the image. The second section determines the proper mean and variance of the noise added to each sample in the simulation grid. The last section validates the model by comparing results from the model with the results predicted by theoretical calculation.

### *A.2 Pixel Array Size*

The noise associated with a CCD is the result of thermal noise, shot noise in the signal current, and noise associated with readout from the CCD [25]. Since these noise effects are independent with respect to each pixel in the array, they are usually modeled as zero mean, Gaussian additive noise, with variance  $\sigma_p^2$  electrons per pixel. Since each pixel in the array is an independent noise source, it is desirable to limit

the array to the minimum size needed to resolve a given target. This development adopts the Rayleigh criterion of resolution: "two incoherent point sources are barely resolved by a diffraction-limited system when the center of the Airy disk generated by one source falls on the first zero of the Airy disk generated by the second" [12]. Hence, the minimum resolvable separation in the image plane,  $\delta_i$ , is given by:

$$\delta_i \approx \frac{1.22 \lambda s_i}{D}, \quad (\text{A.1})$$

where  $\lambda$  is the imaging wavelength,  $s_i$  is the distance from the aperture to the image plane, and  $D$  is the aperture diameter. Let  $\delta_o$  represent the separation of the two point sources in the object plane. Using the thin lens magnification equation [15],  $\delta_i$  and  $\delta_o$  are related by:

$$\delta_i = \frac{s_i}{s_o} \delta_o, \quad (\text{A.2})$$

where  $s_o$  is the distance from the aperture to the object plane. The minimum separation  $\delta_o$  between two points in the object plane that can still be resolved in the image plane is found by combining Eqs.(A.1, A.2), and is given by:

$$\delta_o = \frac{1.22 \lambda s_o}{D} \quad (\text{A.3})$$

The spatial frequency  $\nu$  associated with this separation is given by:

$$\nu = \frac{D}{1.22 \lambda s_o} \quad (\text{A.4})$$

According to the Nyquist sampling theorem [20], the CCD camera array must sample at twice this spatial frequency to perfectly reconstruct the object within the Rayleigh resolution criterion. Thus, the sampling frequency  $\nu_s$  is given by:

$$\nu_s = \frac{2 D}{1.22 \lambda s_o}, \quad (\text{A.5})$$

and the minimum pixel size (in one dimension) is given by:

$$\delta_p = \frac{1.22 \lambda s_o}{2 D} \quad (\text{A.6})$$

Let  $L$  represent the length of the object. Assuming that the object very nearly fills the simulation sample grid, the number of pixels along one side of the CCD pixel array,  $p_x$ , is given by:

$$p_x = \frac{2 D L}{1.22 \lambda s_o} \quad (\text{A.7})$$

Assuming a square CCD pixel array, the total number of pixels  $P$  is given by:

$$P = p_x^2 \quad (\text{A.8})$$

### *A.3 Sample Noise Variance*

The last section determined the minimum number of pixels  $P$  which are needed to meet Rayleigh resolution requirements. Since the mean of a sum of Gaussian random variables is the sum of the means of the individual random variables, and the variance is the sum of the variances [13], the mean for the entire pixel array is zero, and the variance is given by  $P\sigma_p^2$ . Note that the computational algorithms used in the simulation dictate the size of the sample grid in the object and image planes. In general, the number of samples  $l_q^2$  used by the simulation is several times greater than  $P$ . Using the property of the variance of a sum of Gaussian random variables mentioned previously, the variance  $\sigma_s^2$  of the additive noise to be added to each sample in the image plane is related to  $\sigma_p^2$  by:

$$P \sigma_p^2 = l_q^2 \sigma_s^2 \quad (\text{A.9})$$

Thus,  $\sigma_s^2$  is given by:

$$\sigma_s^2 = \frac{P}{l_q^2} \sigma_p^2 \quad (\text{A.10})$$

Hence, the noise effects of a CCD camera consisting of  $P$  pixels with noise variance  $\sigma_p^2$  can be modeled by adding zero mean Gaussian noise with variance  $\sigma_s^2$  to each sample in the image plane.

#### A.4 Model Validation

This section verifies the accuracy of the model by comparing results to values predicted by theoretical calculations. As discussed in chapter three, the expected single frame  $SNR$  for a set of short exposure images measured by an adaptive optics system free of residual tilt error, using a CCD camera, is given by:

$$SNR_{SE}(u, v) = \frac{K |E_{SE}[H(u, v)] O(u, v)|}{\{K + K^2 |O(u, v)|^2 var[H(u, v)] + P \sigma_p^2\}^{\frac{1}{2}}} \quad (\text{A.11})$$

where  $K$  is the average number of photo events per integration time,  $E_{SE}$  is the expectation operator,  $O$  is the object spectrum,  $H$  is the system OTF,  $P$  is the number of pixels employed by the CCD camera and  $\sigma_p^2$  is the camera read noise variance. First, Eq.(A.11) was used to calculate the  $SNR$  for an image formed by averaging 100 short exposure images. The target was the space object discussed in chapter four. The object was assumed to be approximately 12m in length and orbiting at a distance of approximately 500 kilometers. The object's apparent brightness  $m_v$  was +3.0, and the parameter  $r_o$  was set to 10cm. Using Eq.(A.7), the pixel array was

determined to be 79 by 79. The pixel noise variance  $\sigma_p^2$  was set to 30.  $E_{SE}[H(u, v)]$  and  $var[H(u, v)]$  were estimated with the OTFSIM code developed by Michael C. Roggeman. The theoretical results determined from Eq.(A.11) were then compared with the results obtained from the modified version of HYSIM with the CCD model. Figure A.1 demonstrates that the results of the simulation are nearly identical to the the theoretical results.

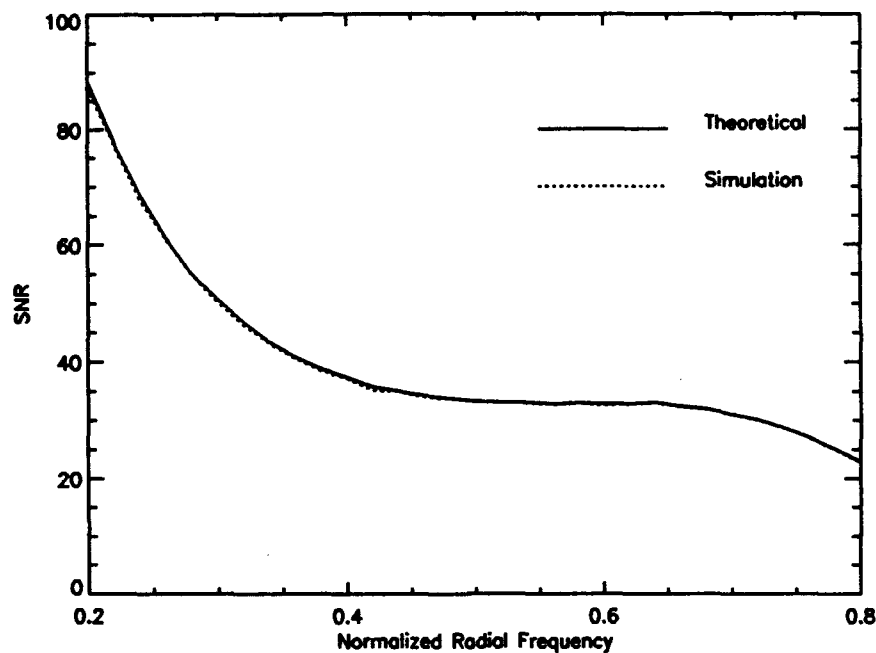


Figure A.1 Comparison of Theoretical and Simulation Results, CCD Camera Model

## *Appendix B. Simulation Results*

This appendix contains the gain curves for the five experiments performed in Chapter four.

### *B.1 Experiment One*

Experimental parameters: point source,  $r_o = 10\text{cm}$ ,  $m_o = -1$ , photon limited

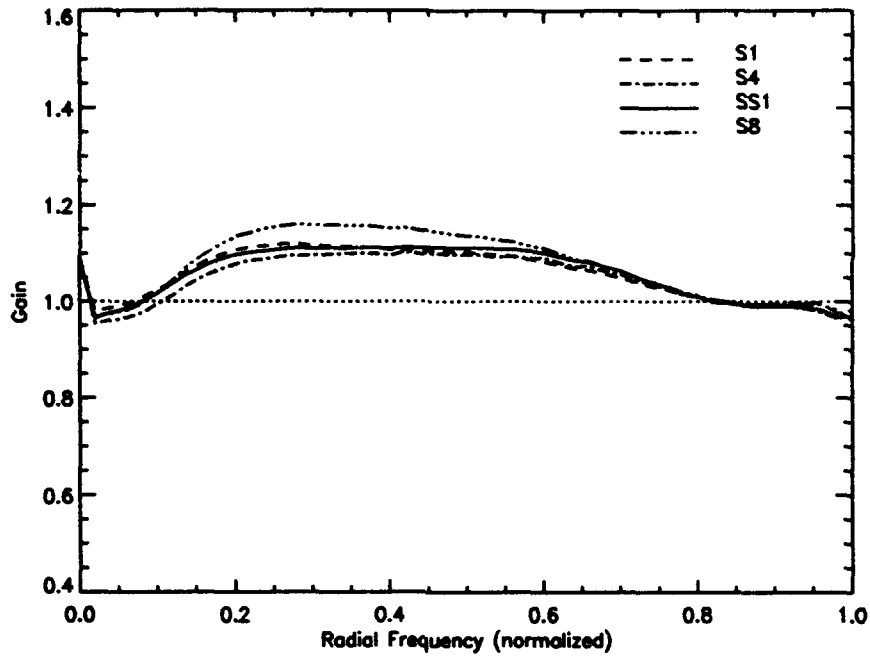


Figure B.1 Gain Curves, Experiment 1: Point source,  $r_o = 10\text{cm}$ ,  $m_v = -1$ , Photon limited, Selection rate = 90%

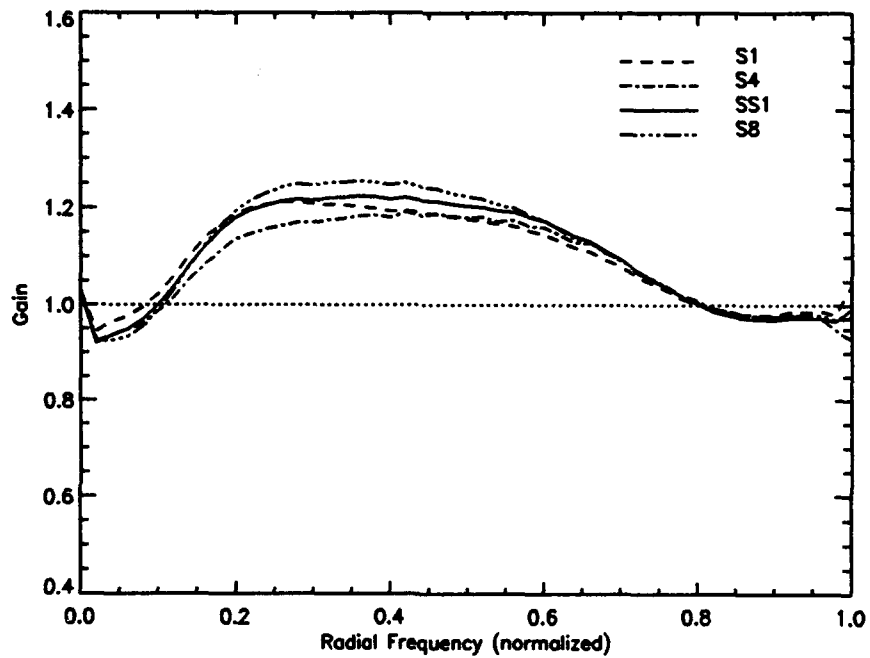


Figure B.2 Gain Curves, Experiment 1: Point source,  $r_o = 10\text{cm}$ ,  $m_v = -1$ , Photon limited, Selection rate = 80%

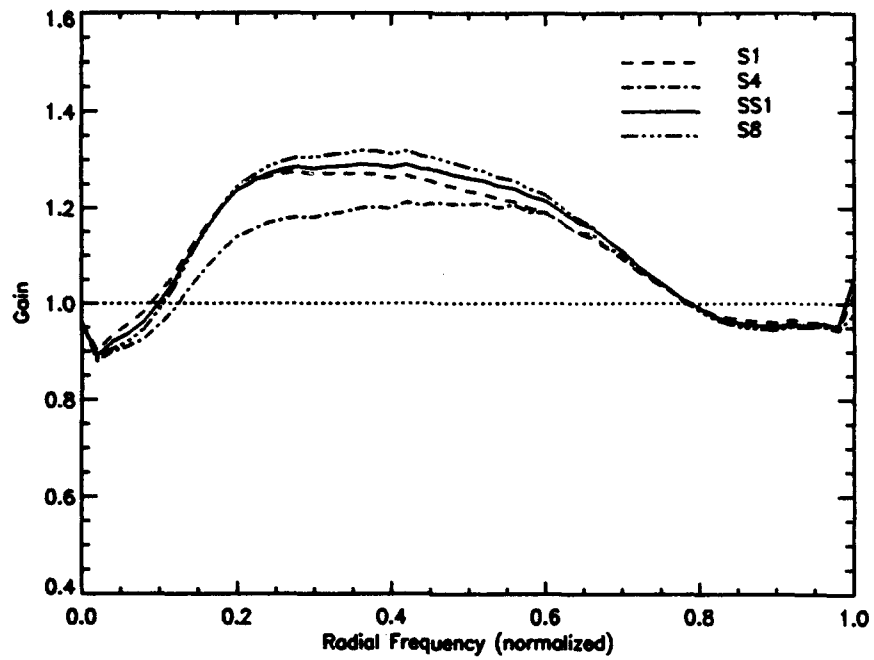


Figure B.3 Gain Curves, Experiment 1: Point source,  $r_o = 10\text{cm}$ ,  $m_v = -1$ , Photon limited, Selection rate = 70%

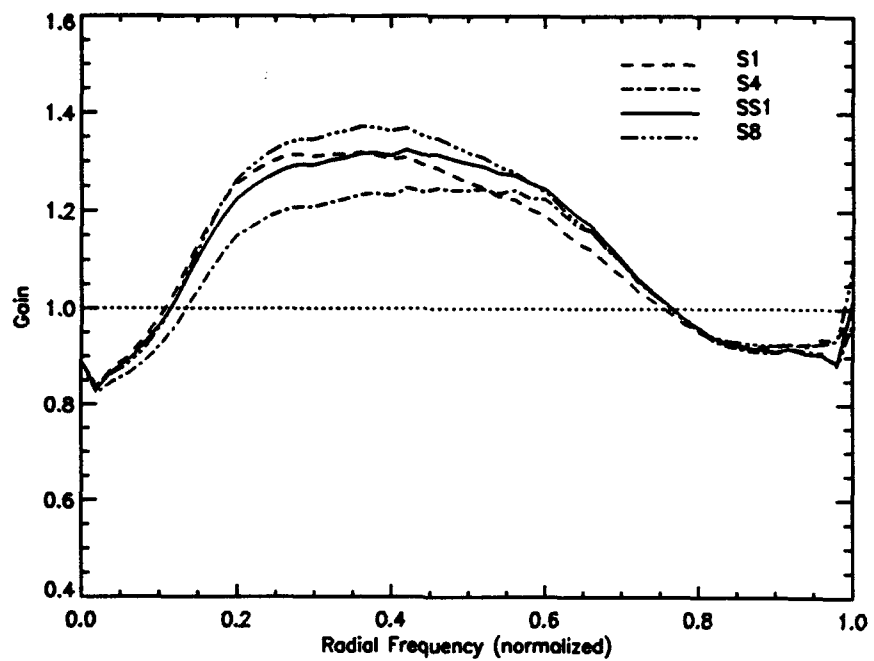


Figure B.4 Gain Curves, Experiment 1: Point source,  $r_o = 10\text{cm}$ ,  $m_v = -1$ , Photon limited, Selection rate = 60%

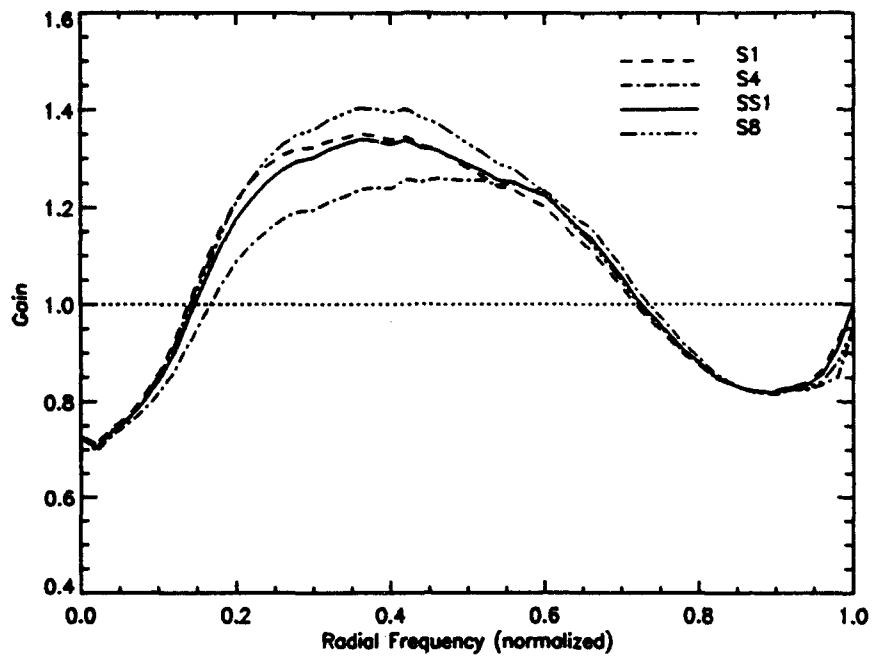


Figure B.5 Gain Curves, Experiment 1: Point source,  $r_o = 10\text{cm}$ ,  $m_v = -1$ , Photon limited, Selection rate = 40%

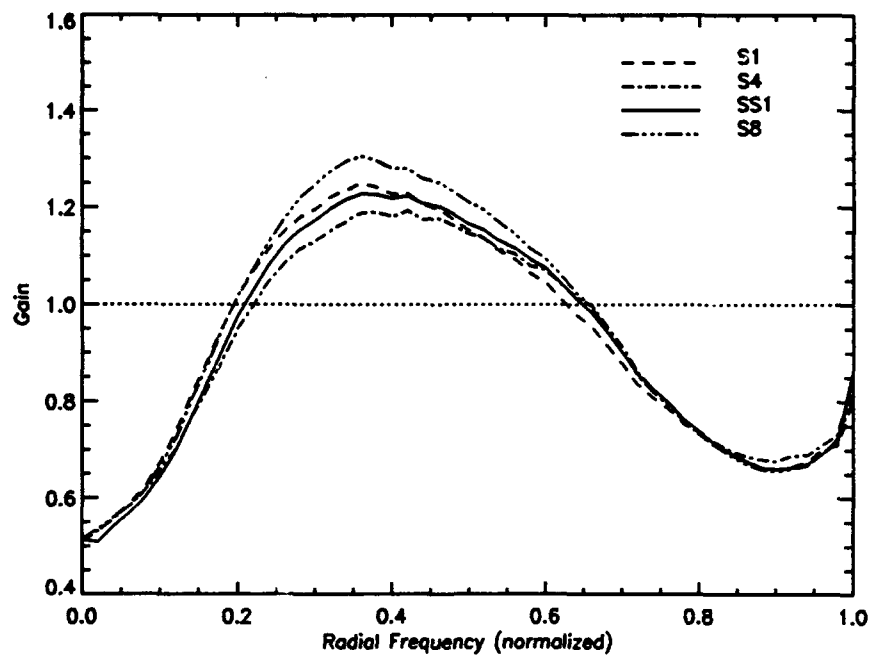


Figure B.6 Gain Curves, Experiment 1: Point source,  $r_o = 10\text{cm}$ ,  $m_v = -1$ , Photon Limited, Selection rate = 20%

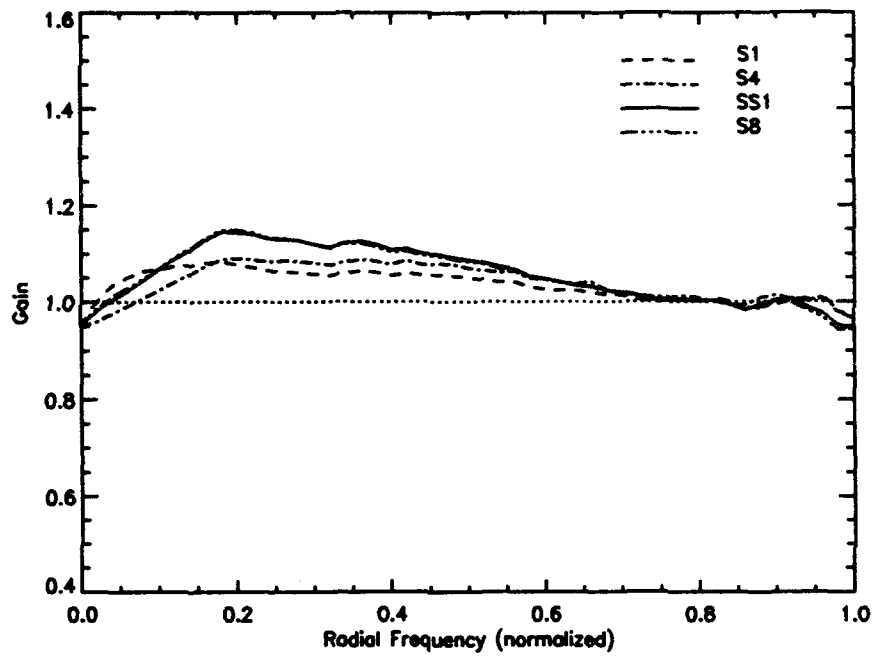


Figure B.7 Gain Curves, Experiment 2: Extended object,  $r_o = 10\text{cm}$ ,  $m_v = -1$ , Photon limited, Selection rate = 90%

### B.2 Experiment Two

Experimental parameters: extended object,  $r_o = 10\text{cm}$ ,  $m_v = -1$ , photon limited

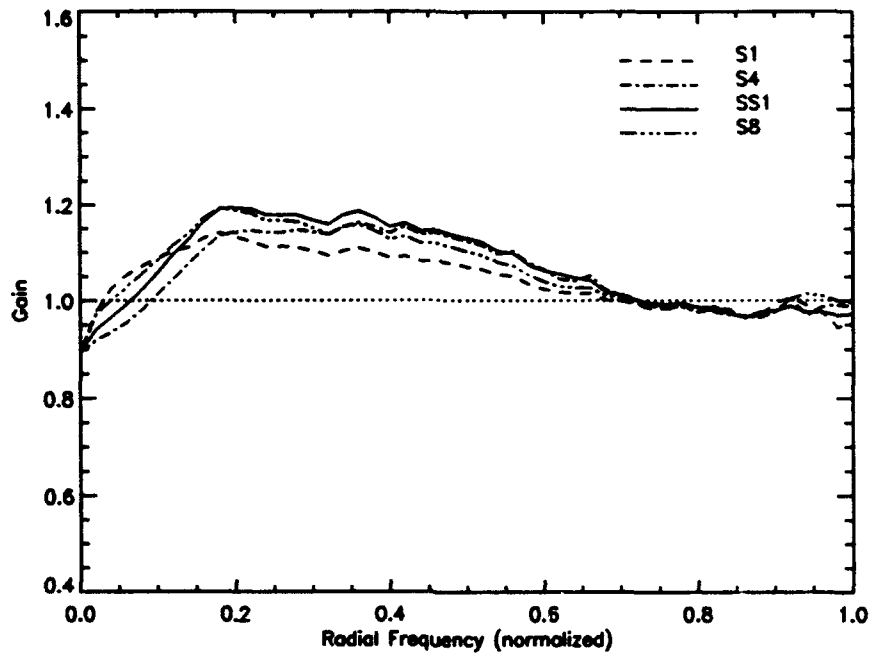


Figure B.8 Gain Curves, Experiment 2: Extended object,  $r_o = 10\text{cm}$ ,  $m_v = -1$ , Photon limited, Selection rate = 80%

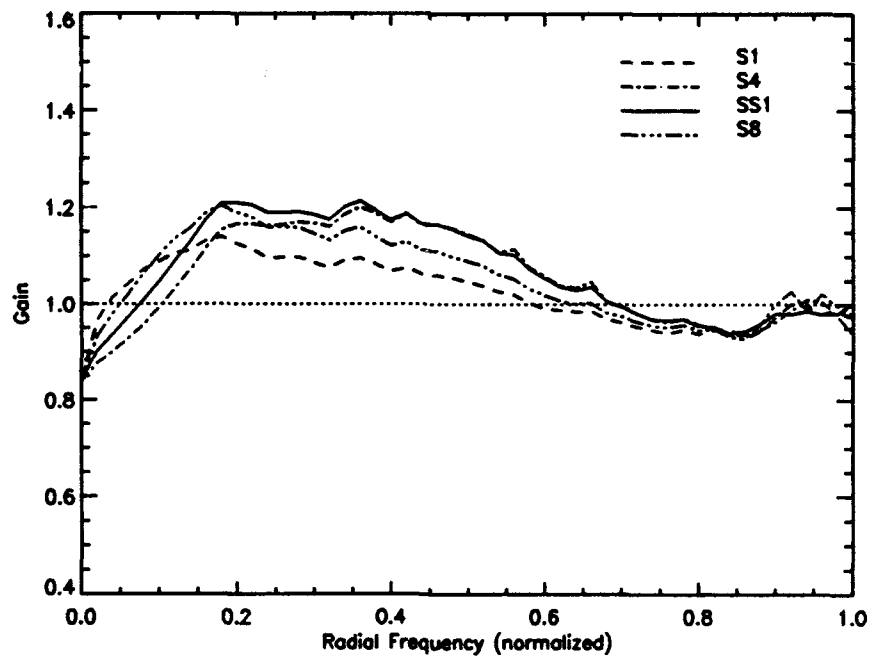


Figure B.9 Gain Curves, Experiment 2: Extended object,  $r_o = 10\text{cm}$ ,  $m_v = -1$ , Photon limited, Selection rate = 70%

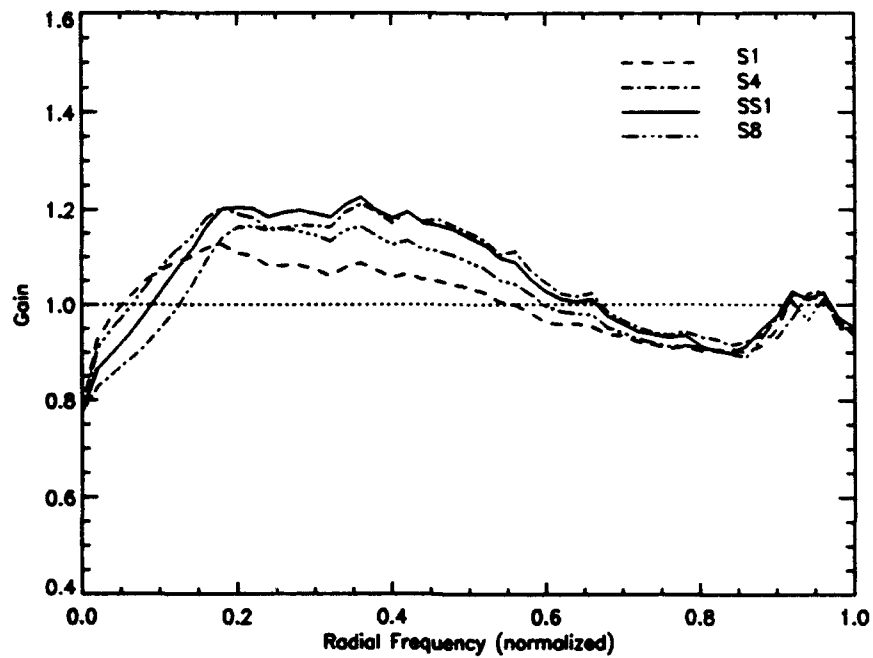


Figure B.10 Gain Curves, Experiment 2: Extended object,  $r_o = 10\text{cm}$ ,  $m_v = -1$ , Photon limited, Selection rate = 60%

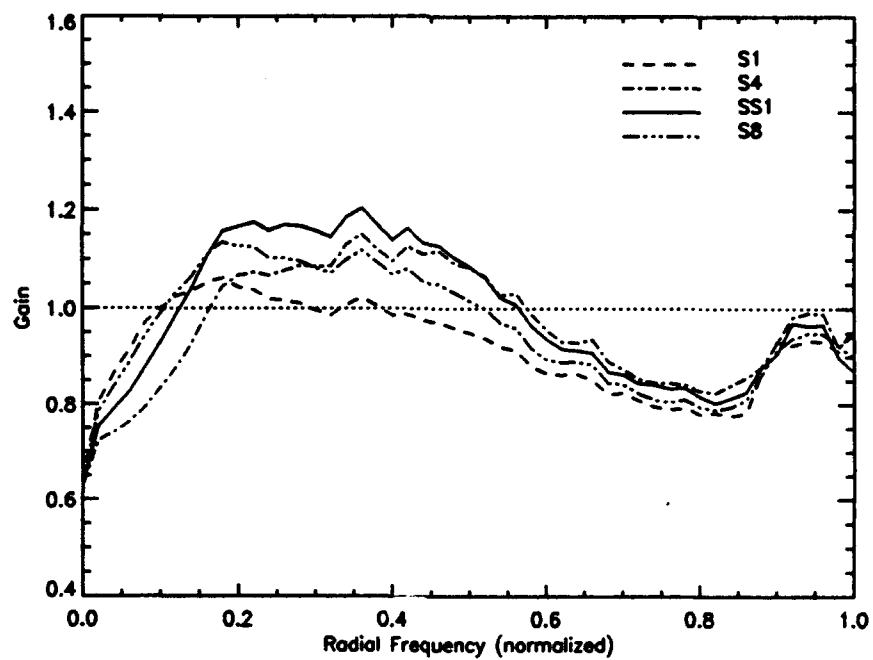


Figure B.11 Gain Curves, Experiment 2: Extended object,  $r_o = 10\text{cm}$ ,  $m_v = -1$ , Photon limited, Selection rate = 40%

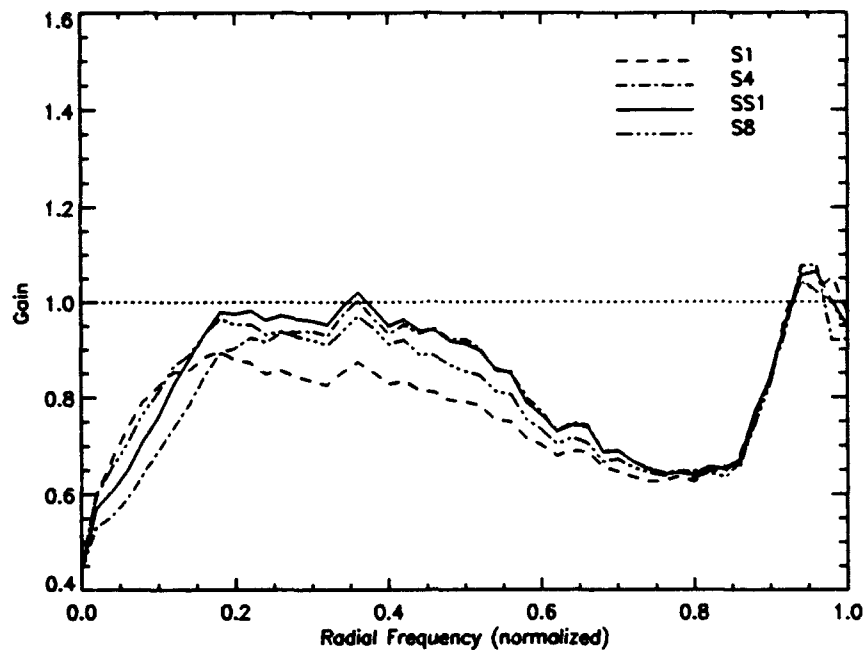


Figure B.12 Gain Curves, Experiment 2: Extended object,  $r_o = 10\text{cm}$ ,  $m_v = -1$ , Photon limited, Selection rate = 20%

### B.3 Experiment Three

Experimental parameters: extended object,  $r_o = 7, 13\text{cm}$ ,  $m_v = -1$ , photon limited

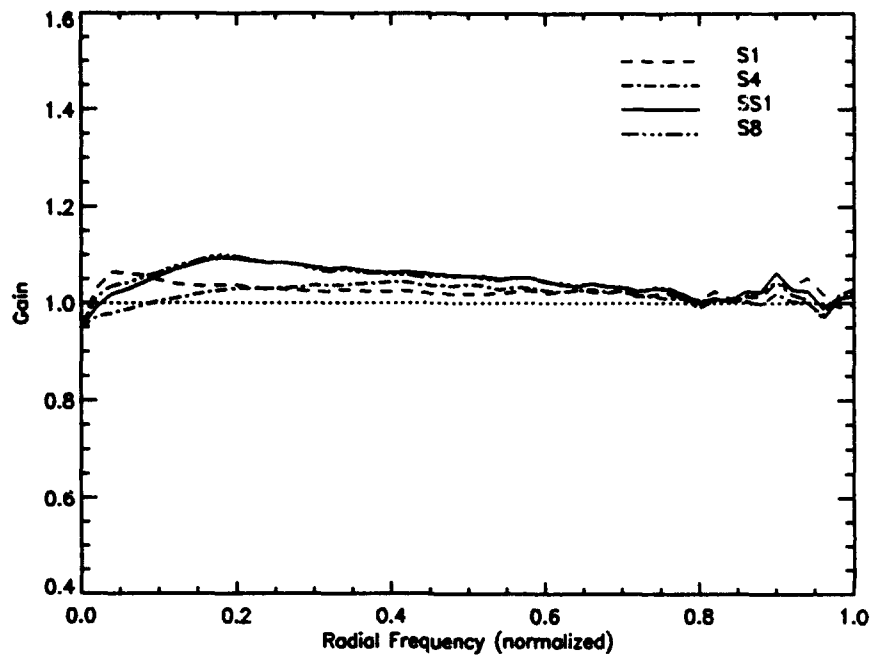


Figure B.13 Gain Curves, Experiment 3: Extended object,  $r_o = 7\text{cm}$ ,  $m_v = -1$ , Photon limited, Selection rate = 90%

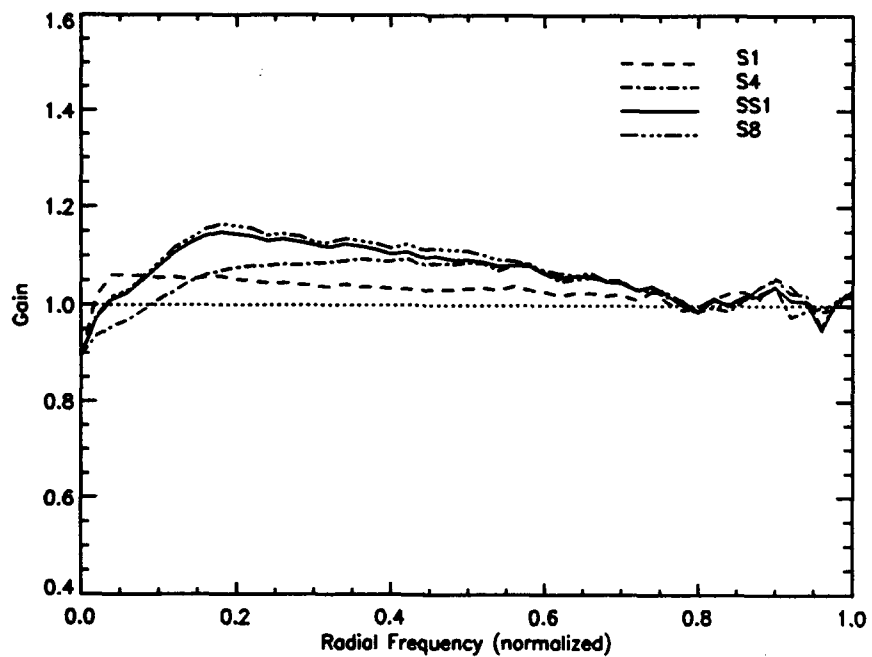


Figure B.14 Gain Curves, Experiment 3: Extended object,  $r_o = 7\text{cm}$ ,  $m_v = -1$ , Photon limited, Selection rate = 80%

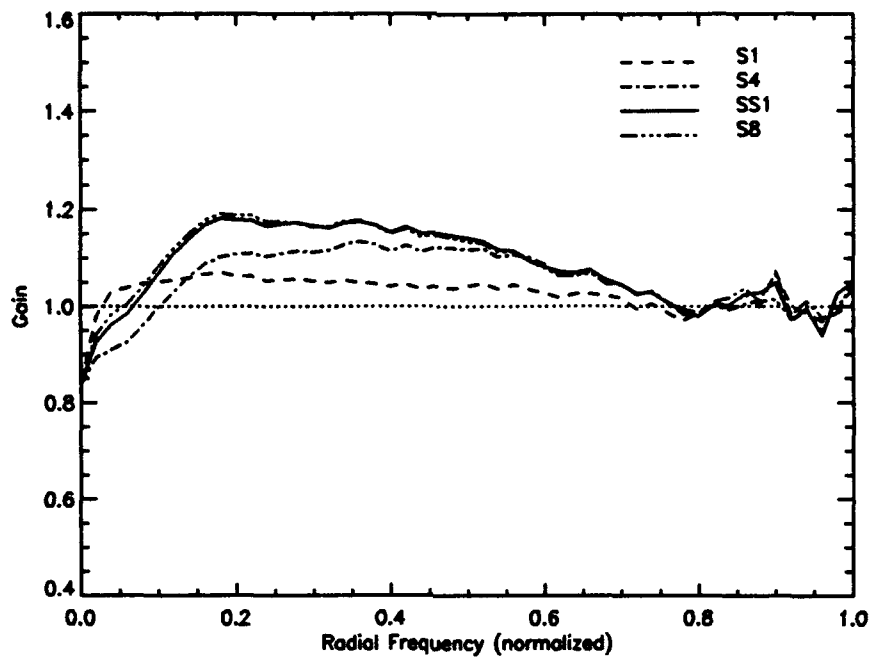


Figure B.15 Gain Curves, Experiment 3: Extended object,  $r_o = 7\text{cm}$ ,  $m_v = -1$ , Photon limited, Selection rate = 70%

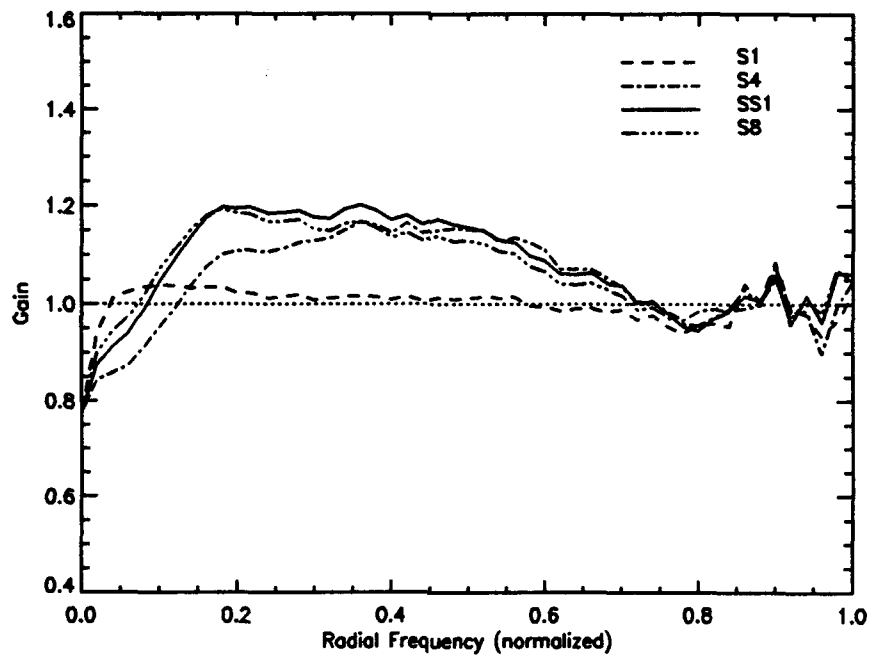


Figure B.16 Gain Curves, Experiment 3: Extended object,  $r_o = 7\text{cm}$ ,  $m_v = -1$ , Photon limited, Selection rate = 60%

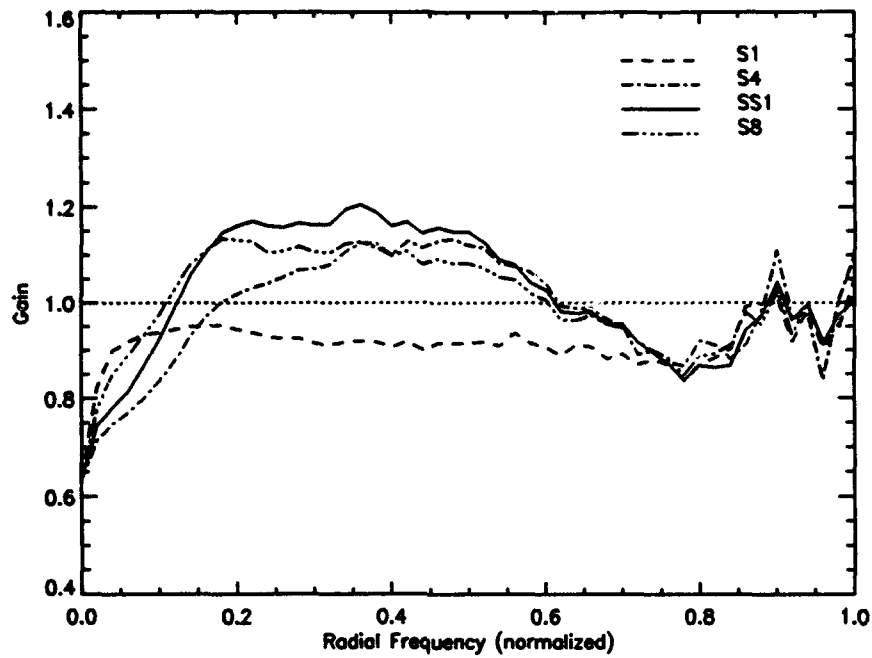


Figure B.17 Gain Curves, Experiment 3: Extended object,  $r_o = 7\text{cm}$ ,  $m_v = -1$ , Photon limited, Selection rate = 40%

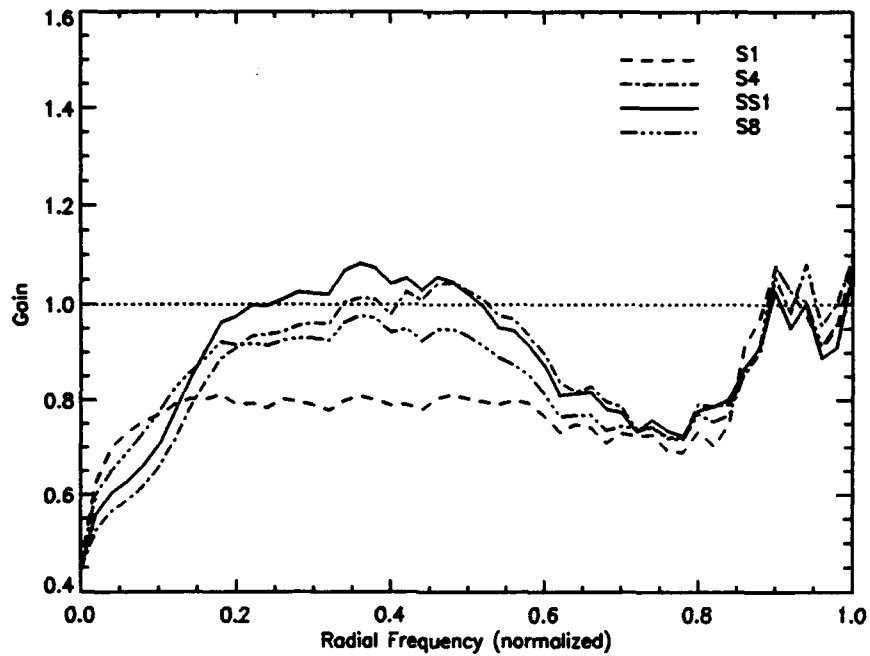


Figure B.18 Gain Curves, Experiment 3: Extended object,  $r_o = 7\text{cm}$ ,  $m_v = -1$ , Photon limited, Selection rate = 20%

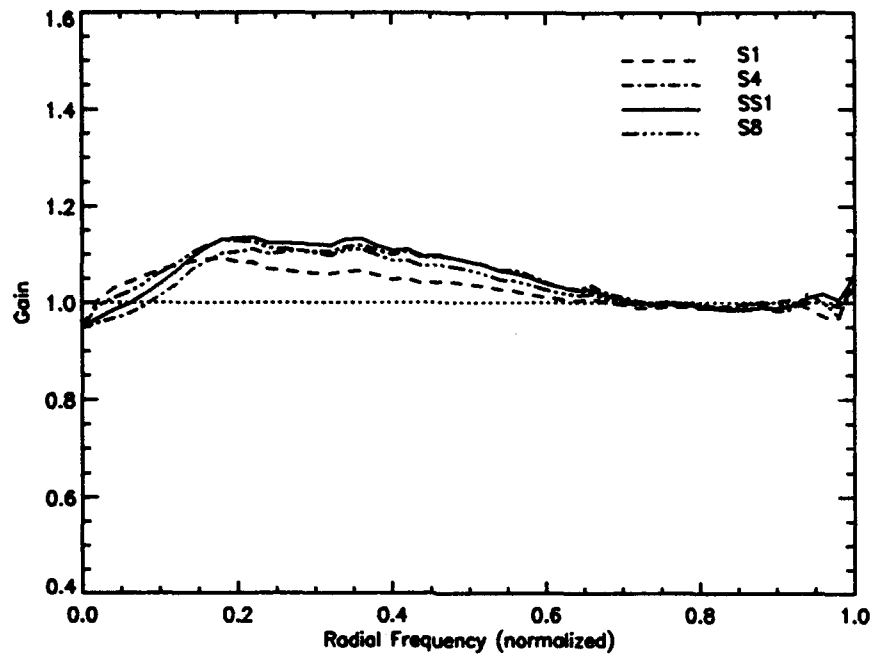


Figure B.19 Gain Curves, Experiment 3: Extended object,  $r_o = 13\text{cm}$ ,  $m_v = -1$ , Photon limited, Selection rate = 90%

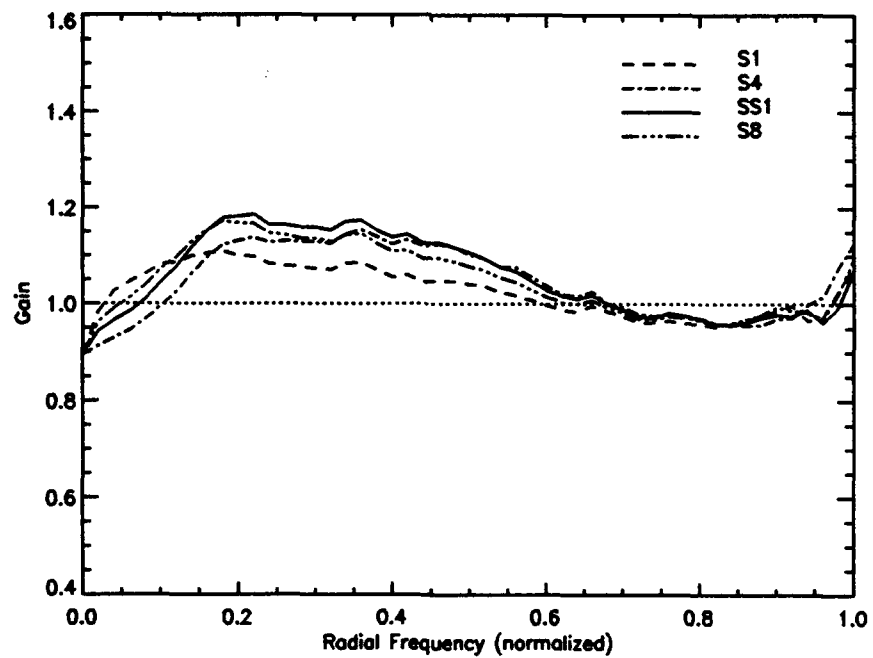


Figure B.20 Gain Curves, Experiment 3: Extended object,  $r_o = 13\text{cm}$ ,  $m_v = -1$ , Photon limited, Selection rate = 80%

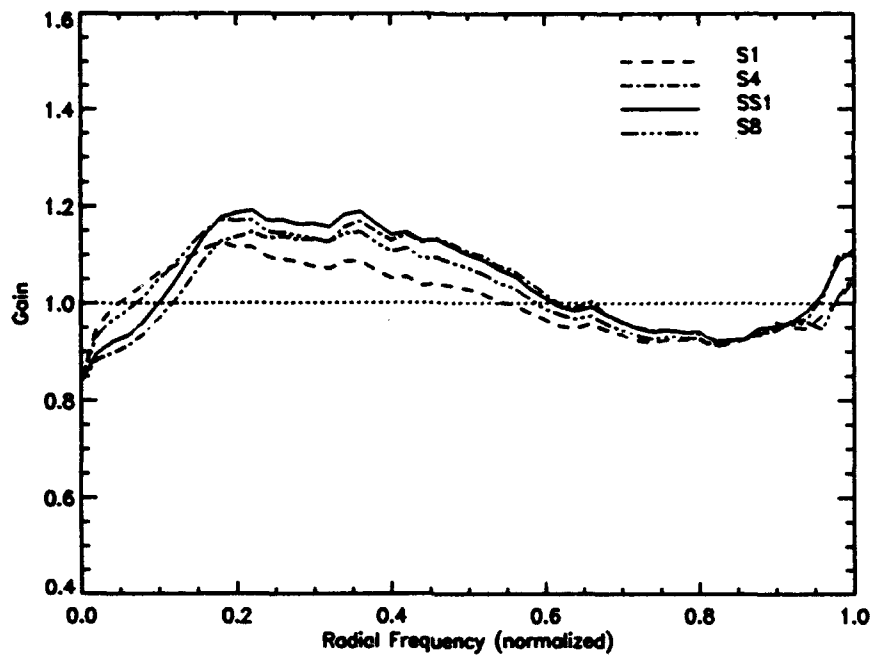


Figure B.21 Gain Curves, Experiment 3: Extended object,  $r_o = 13\text{cm}$ ,  $m_v = -1$ , Photon limited, Selection rate = 70%

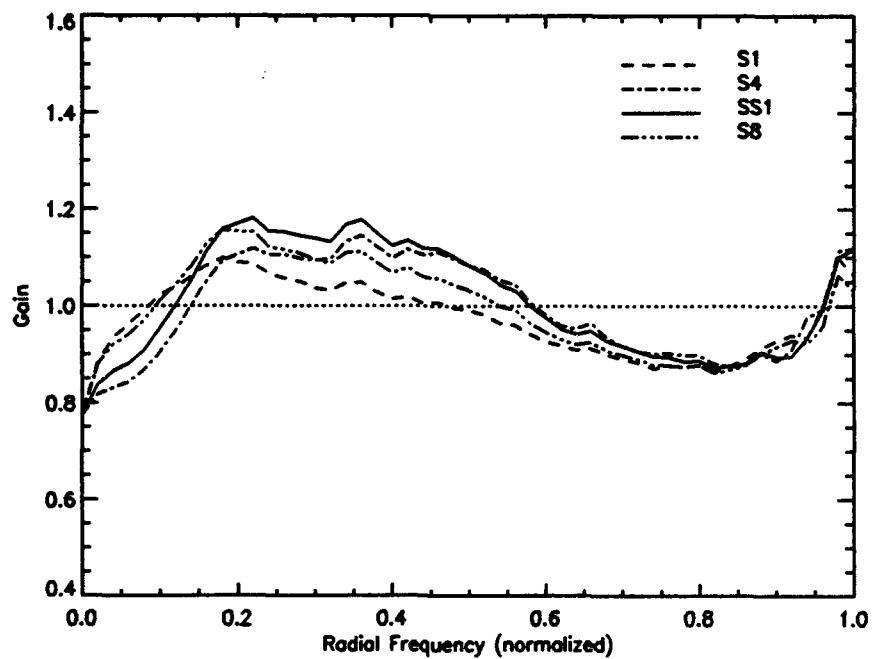


Figure B.22 Gain Curves, Experiment 3: Extended object,  $r_o = 13\text{cm}$ ,  $m_v = -1$ , Photon limited, Selection rate = 60%

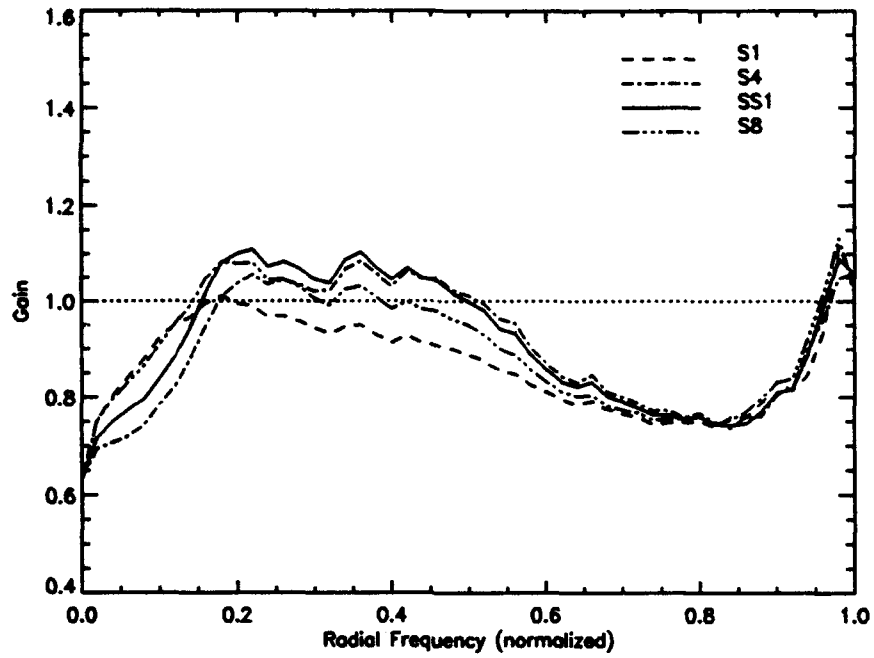


Figure B.23 Gain Curves, Experiment 3: Extended object,  $r_o = 13\text{cm}$ ,  $m_v = -1$ , Photon limited, Selection rate = 40%

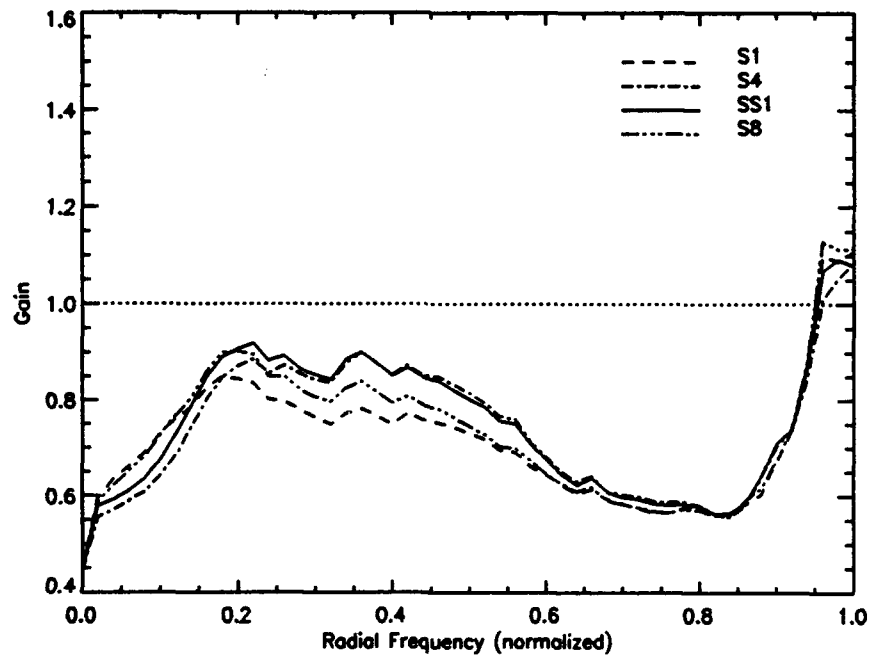


Figure B.24 Gain Curves, Experiment 3: Extended object,  $r_o = 13\text{cm}$ ,  $m_v = -1$ , Photon limited, Selection rate = 20%

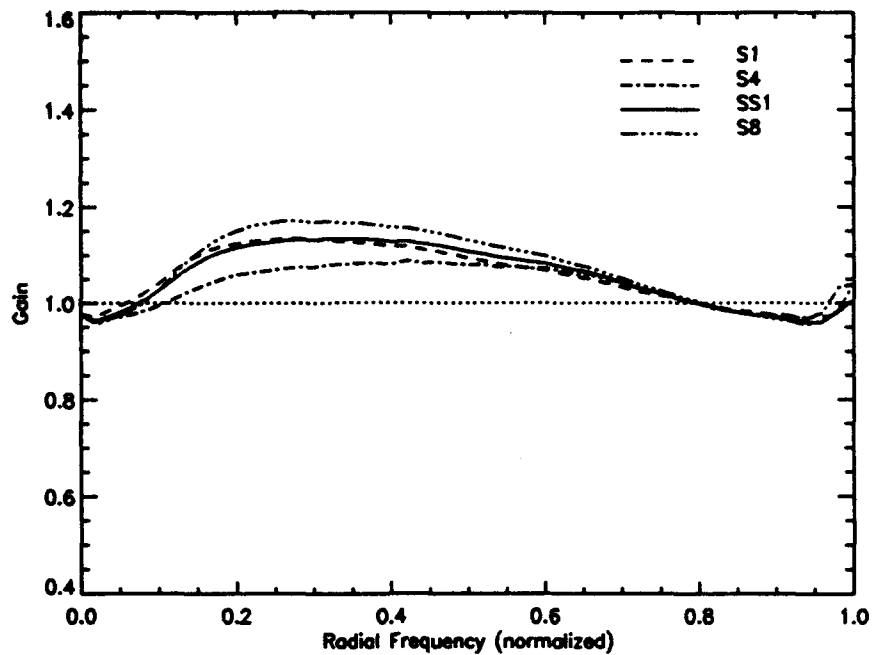


Figure B.25 Gain Curves, Experiment 4: Point source,  $r_o = 10\text{cm}$ ,  $m_v = +3$ , Photon limited, Selection rate = 90%

#### B.4 Experiment Four

Experimental parameters: extended object, point source,  $r_o = 10\text{cm}$ ,  $m_v = +3$ , photon limited

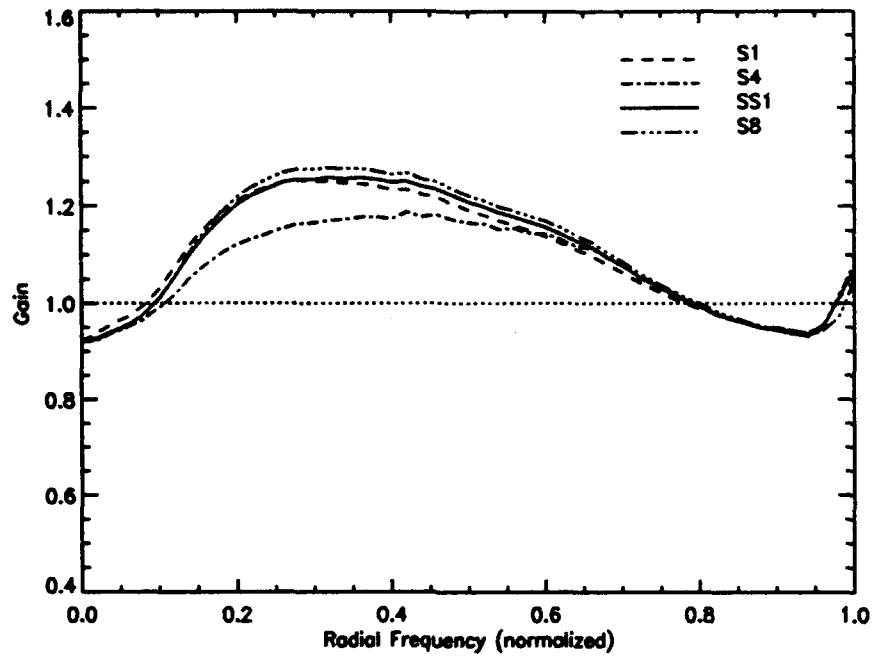


Figure B.26 Gain Curves, Experiment 4: Point source,  $r_o = 10\text{cm}$ ,  $m_v = +3$ , Photon limited, Selection rate = 80%

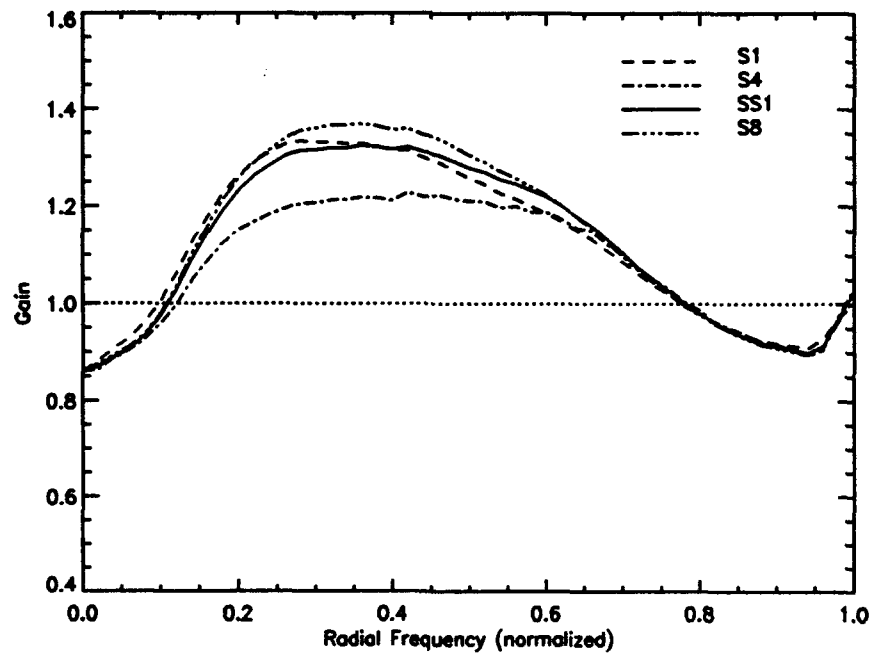


Figure B.27 Gain Curves, Experiment 4: Point source,  $r_o = 10\text{cm}$ ,  $m_v = +3$ , Photon limited, Selection rate = 70%

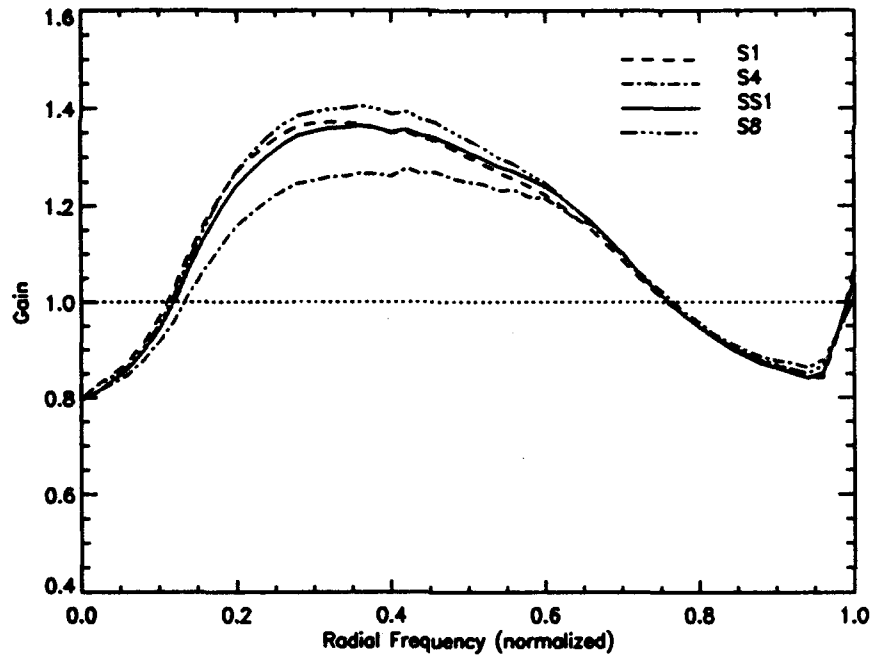


Figure B.28 Gain Curves, Experiment 4: Point source,  $r_o = 10\text{cm}$ ,  $m_v = +3$ , Photon limited, Selection rate = 60%

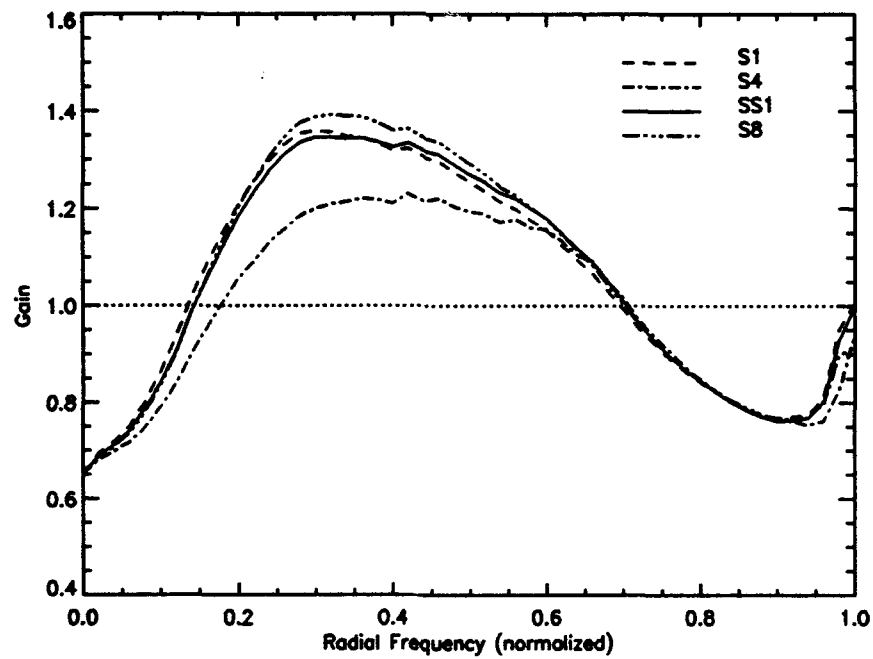


Figure B.29 Gain Curves, Experiment 4: Point source,  $r_o = 10\text{cm}$ ,  $m_v = +3$ , Photon limited, Selection rate = 40%

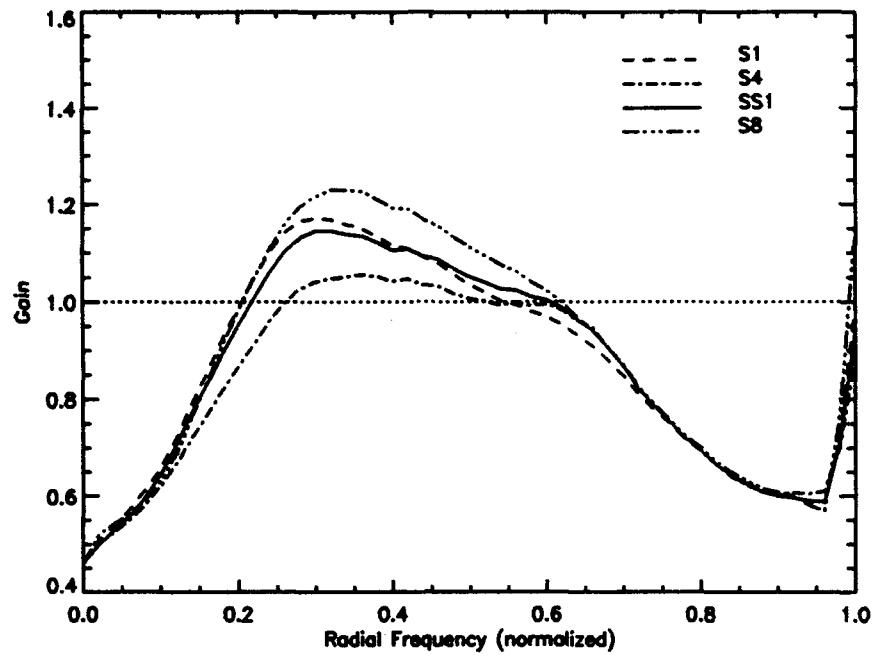


Figure B.30 Gain Curves, Experiment 4: Point source,  $r_o = 10\text{cm}$ ,  $m_v = +3$ , Photon limited, Selection rate = 20%

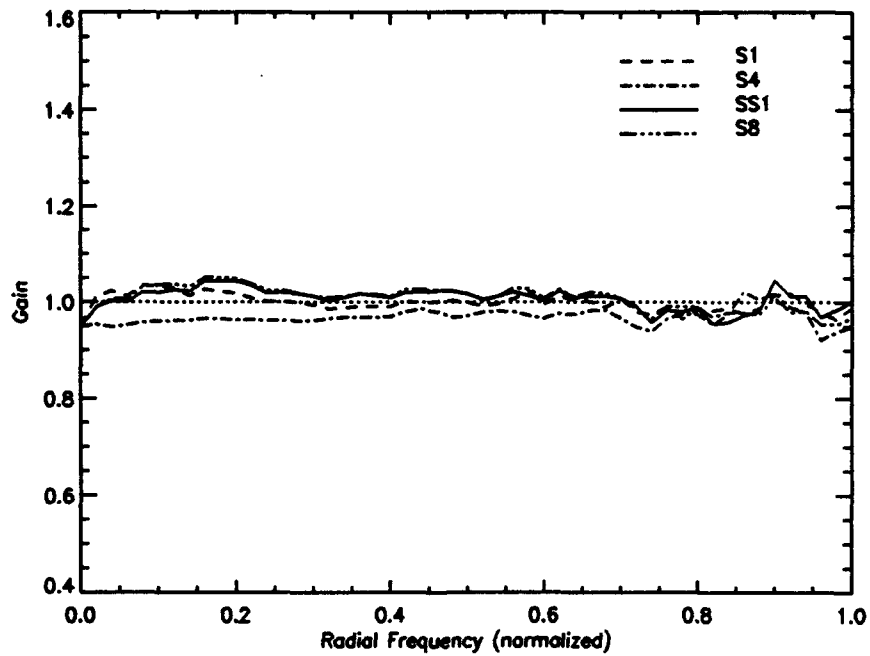


Figure B.31 Gain Curves, Experiment 4: Extended object,  $r_o = 10\text{cm}$ ,  $m_v = +3$ , Photon limited, Selection rate = 90%

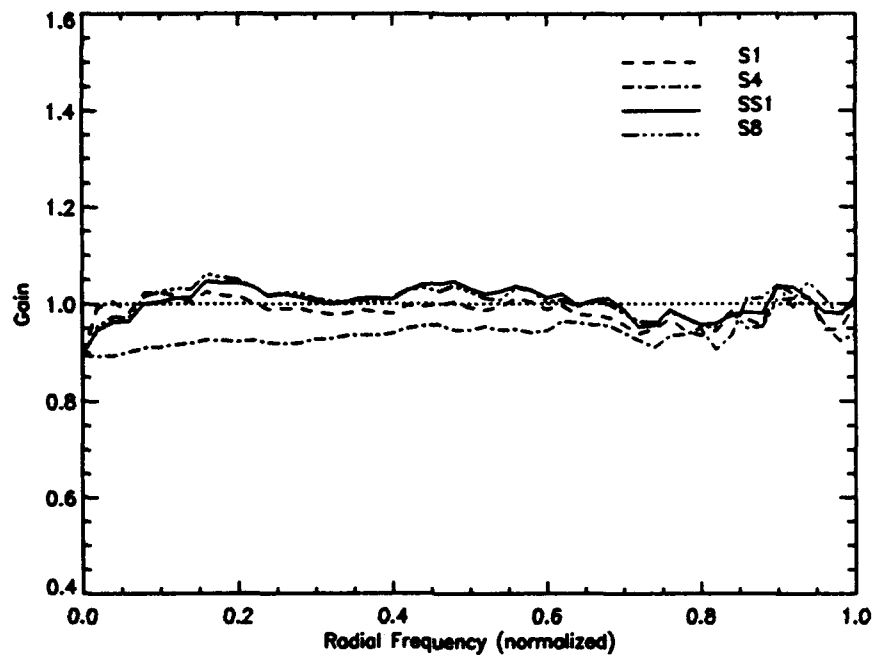


Figure B.32 Gain Curves, Experiment 4: Extended object,  $r_o = 10\text{cm}$ ,  $m_v = +3$ , Photon limited, Selection rate = 80%

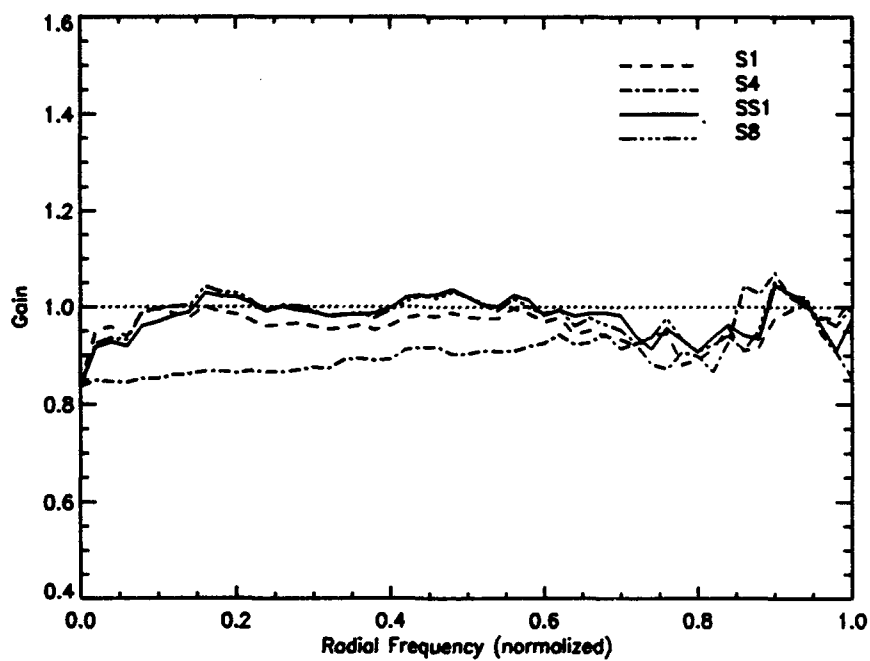


Figure B.33 Gain Curves, Experiment 4: Extended object,  $r_o = 10\text{cm}$ ,  $m_v = +3$ , Photon limited, Selection rate = 70%

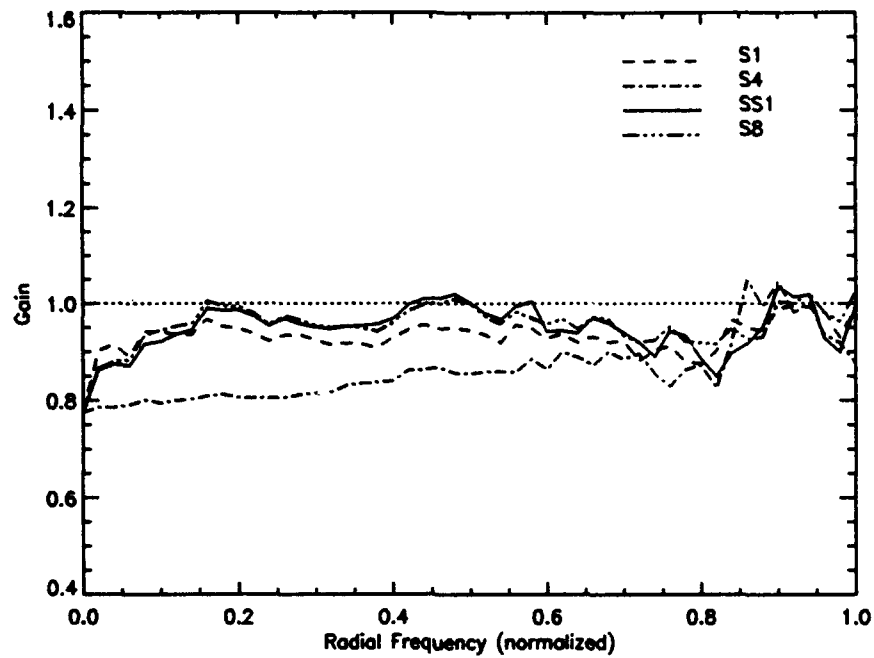


Figure B.34 Gain Curves, Experiment 4: Extended object,  $r_o = 10\text{cm}$ ,  $m_v = +3$ , Photon limited, Selection rate = 60%

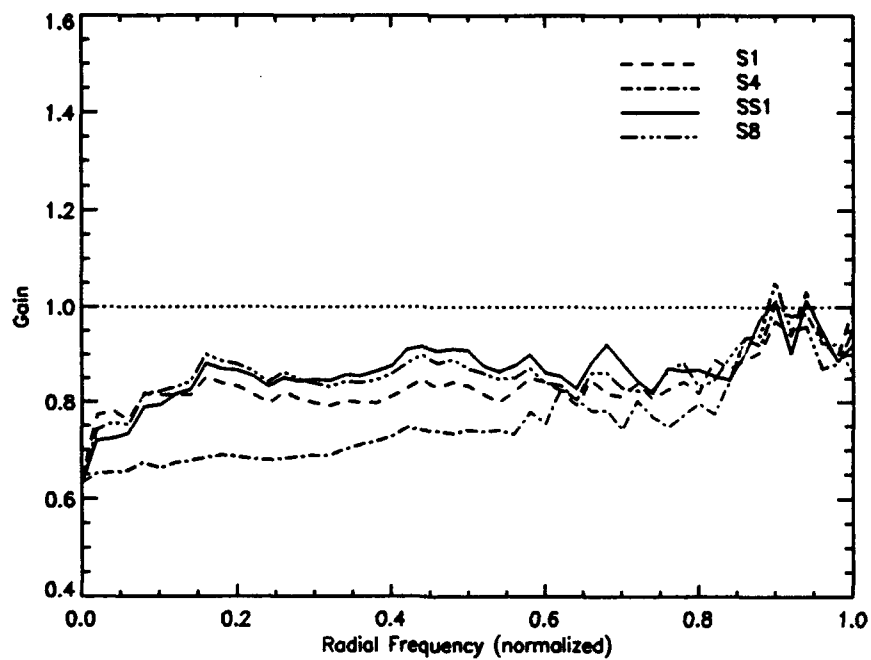


Figure B.35 Gain Curves, Experiment 4: Extended object,  $r_o = 10\text{cm}$ ,  $m_v = +3$ , Photon limited, Selection rate = 40%

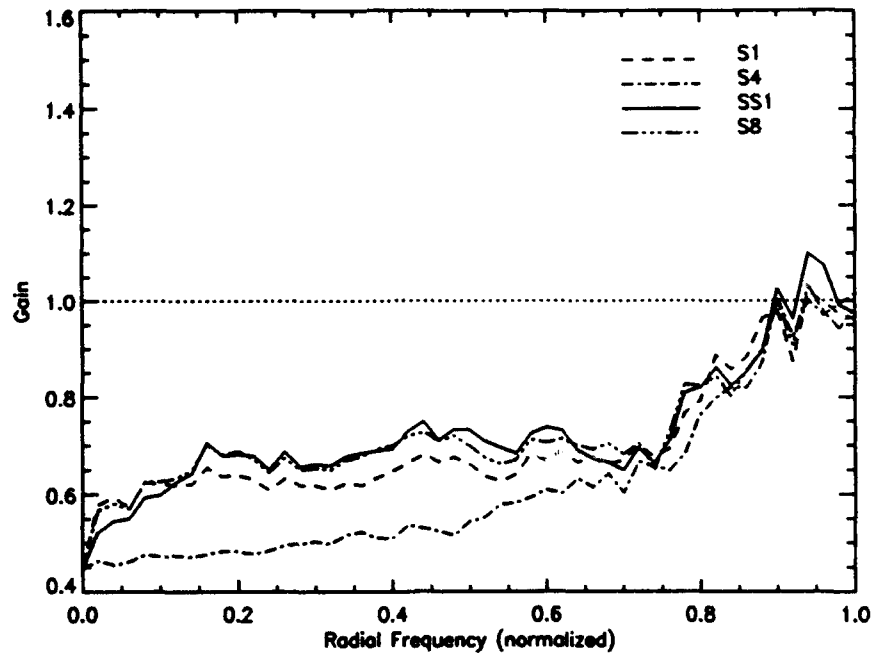


Figure B.36 Gain Curves, Experiment 4: Extended object,  $r_o = 10\text{cm}$ ,  $m_v = +3$ , Photon limited, Selection rate = 20%

*B.5 Experiment Five*

Experimental parameters: point source,  $r_o = 10\text{cm}$ ,  $m_v = +3$ ,  $\sigma^2 = 15, 30$

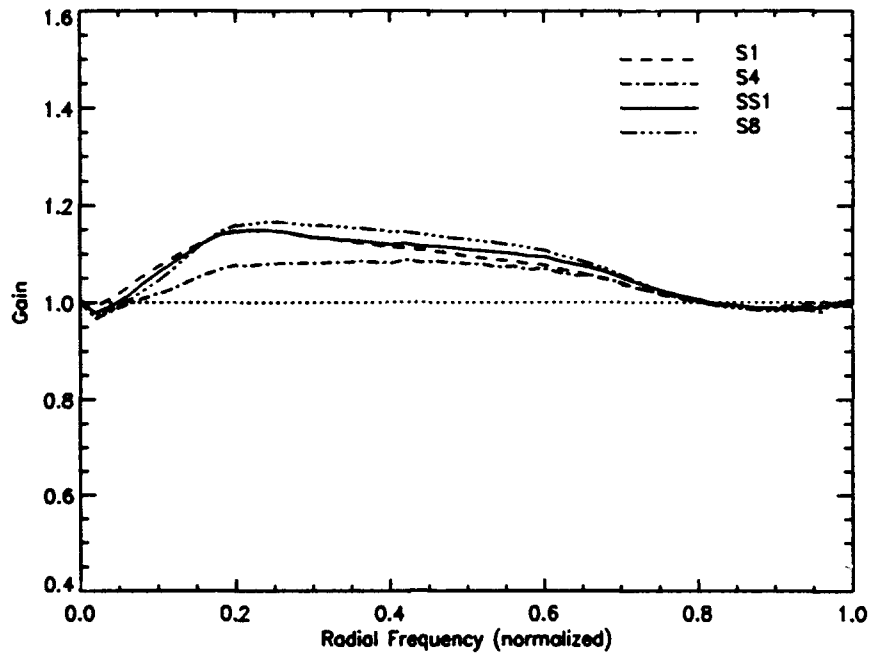


Figure B.37 Gain Curves, Experiment 5: Point source,  $r_o = 10\text{cm}$ ,  $m_v = +3$ ,  $\sigma^2 = 15$ , Selection rate = 90%

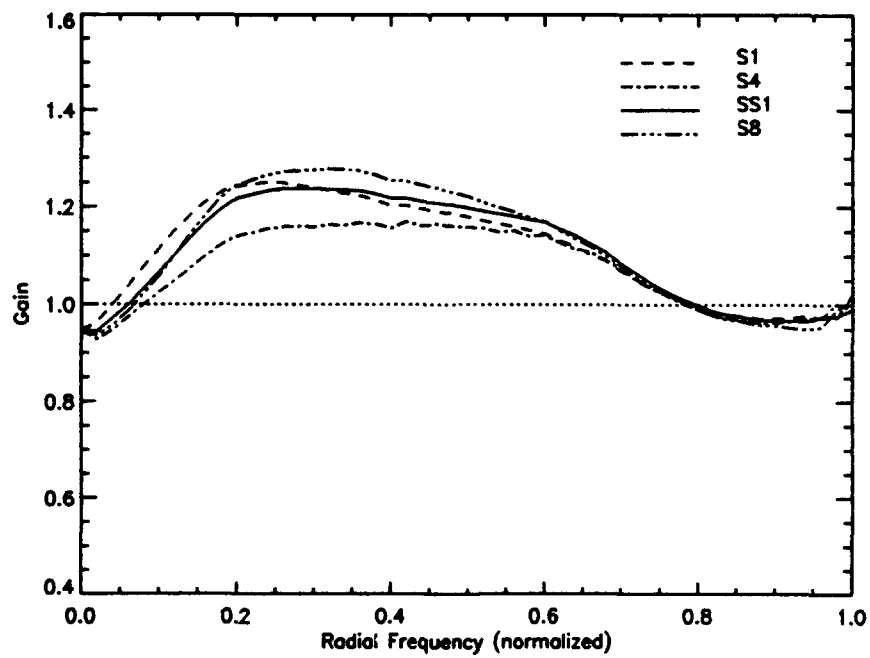


Figure B.38 Gain Curves, Experiment 5: Point source,  $r_o = 10\text{cm}$ ,  $m_v = +3$ ,  $\sigma^2 = 15$ , Selection rate = 80%

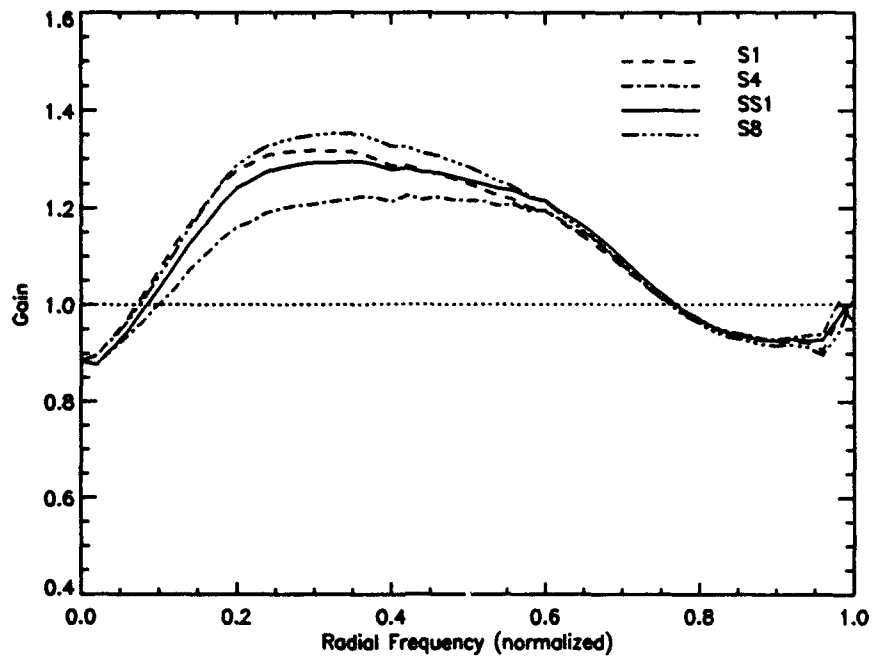


Figure B.39 Gain Curves, Experiment 5: Point source,  $r_o = 10\text{cm}$ ,  $m_v = +3$ ,  $\sigma^2 = 15$ , Selection rate = 70%

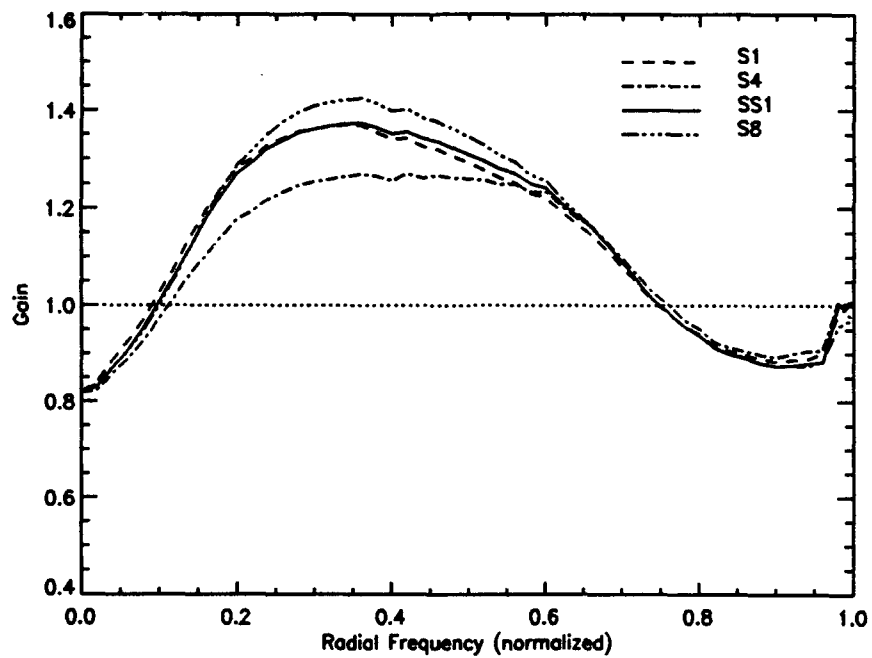


Figure B.40 Gain Curves, Experiment 5: Point source,  $r_o = 10\text{cm}$ ,  $m_v = +3$ ,  $\sigma^2 = 15$ , Selection rate = 60%

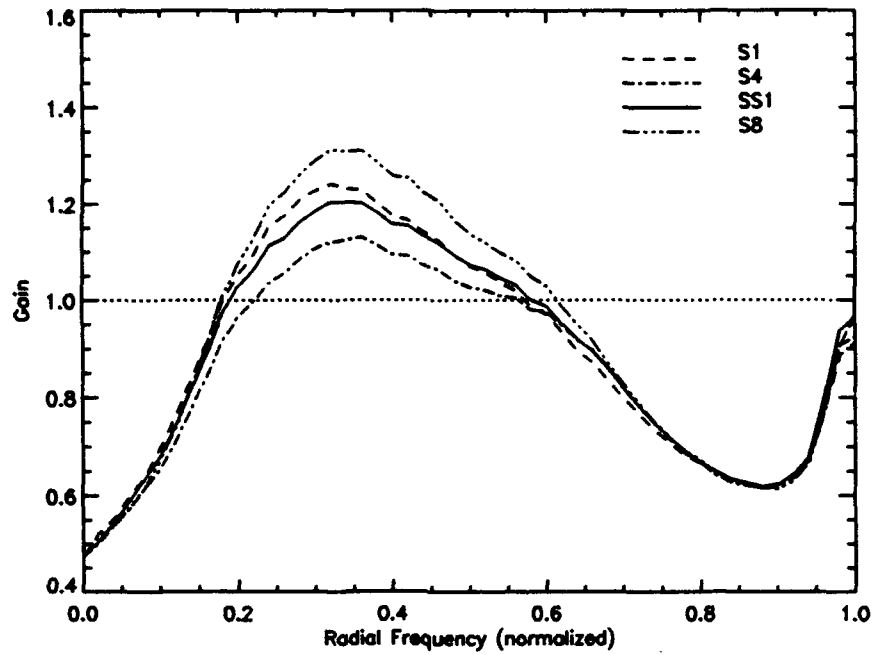


Figure B.41 Gain Curves, Experiment 5: Point source,  $r_o = 10\text{cm}$ ,  $m_v = +3$ ,  $\sigma^2 = 15$ , Selection rate = 20%

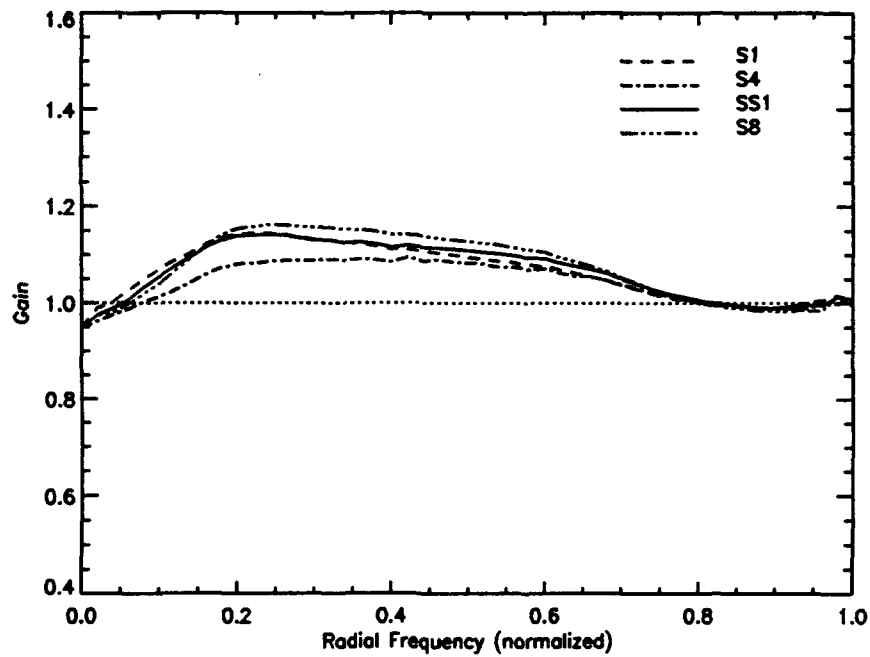


Figure B.42 Gain Curves, Experiment 5: Point source,  $r_o = 10\text{cm}$ ,  $m_v = +3$ ,  $\sigma^2 = 30$ , Selection rate = 90%

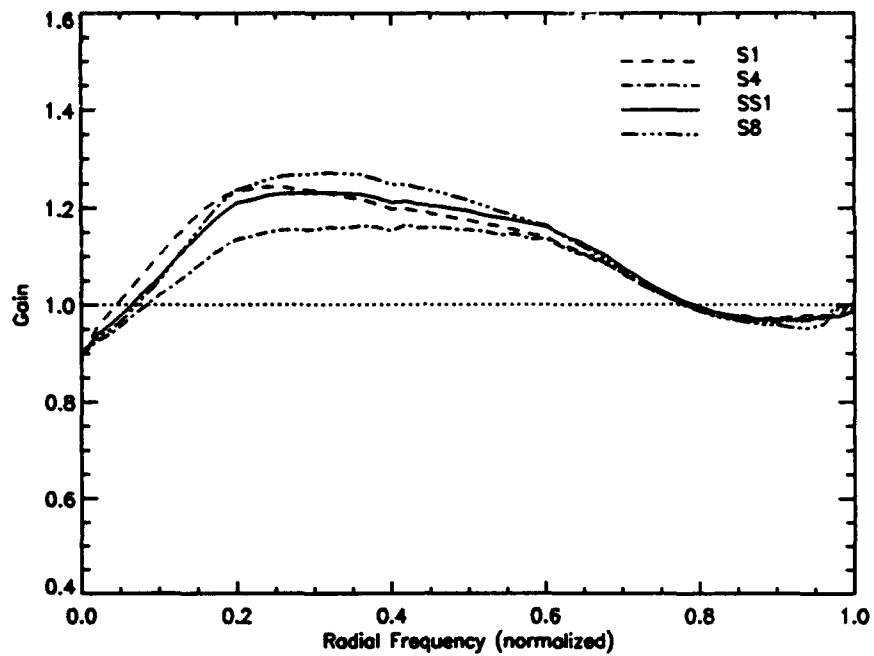


Figure B.43 Gain Curves, Experiment 5: Point source,  $r_o = 10\text{cm}$ ,  $m_v = +3$ ,  $\sigma^2 = 30$ , Selection rate = 80%

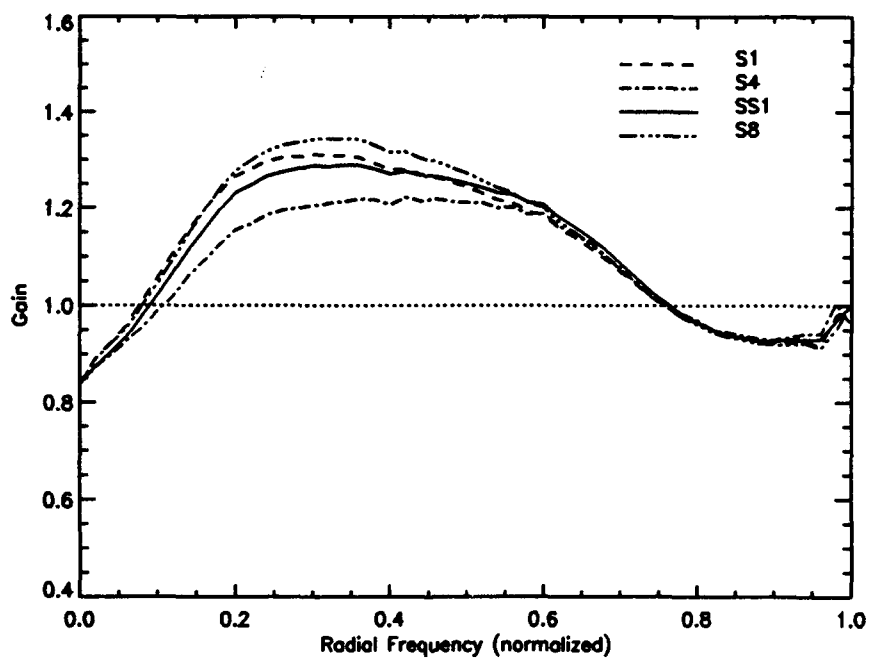


Figure B.44 Gain Curves, Experiment 5: Point source,  $r_o = 10\text{cm}$ ,  $m_v = +3$ ,  $\sigma^2 = 30$ , Selection rate = 70%

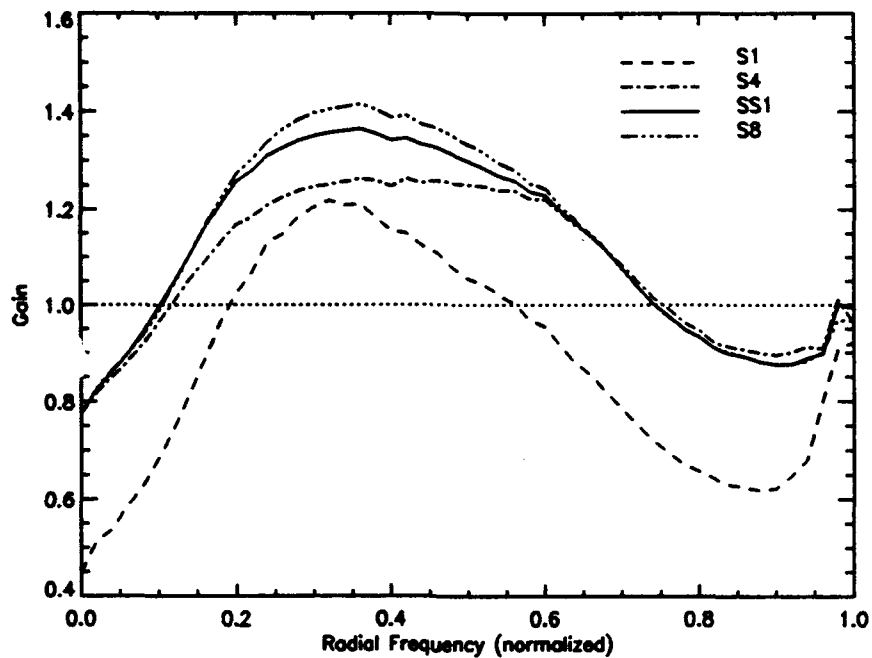


Figure B.45 Gain Curves, Experiment 5: Point source,  $r_o = 10\text{cm}$ ,  $m_v = +3$ ,  $\sigma^2 = 30$ , Selection rate = 60%

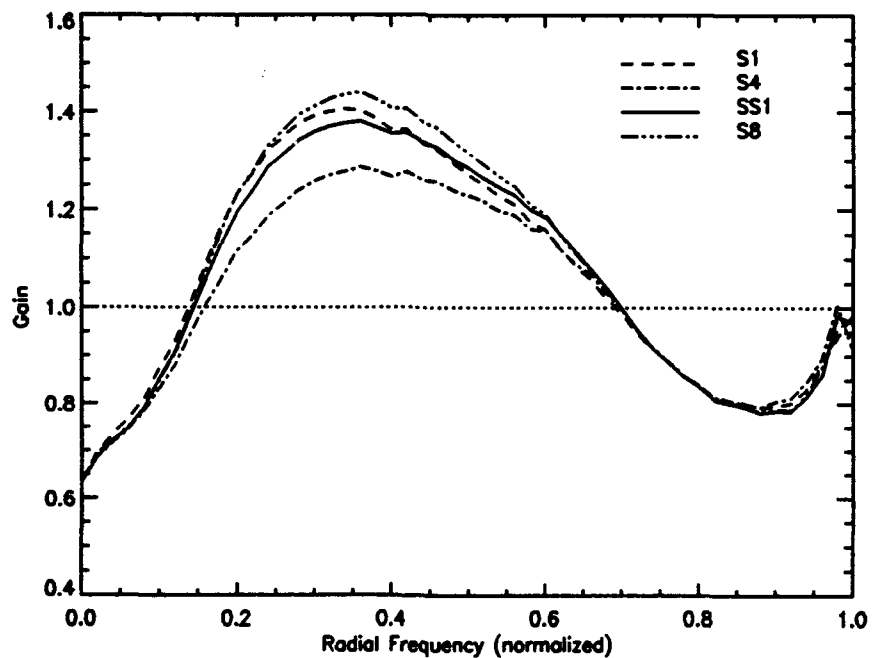


Figure B.46 Gain Curves, Experiment 5: Point source,  $r_o = 10\text{cm}$ ,  $m_v = +3$ ,  $\sigma^2 = 30$ , Selection rate = 40%

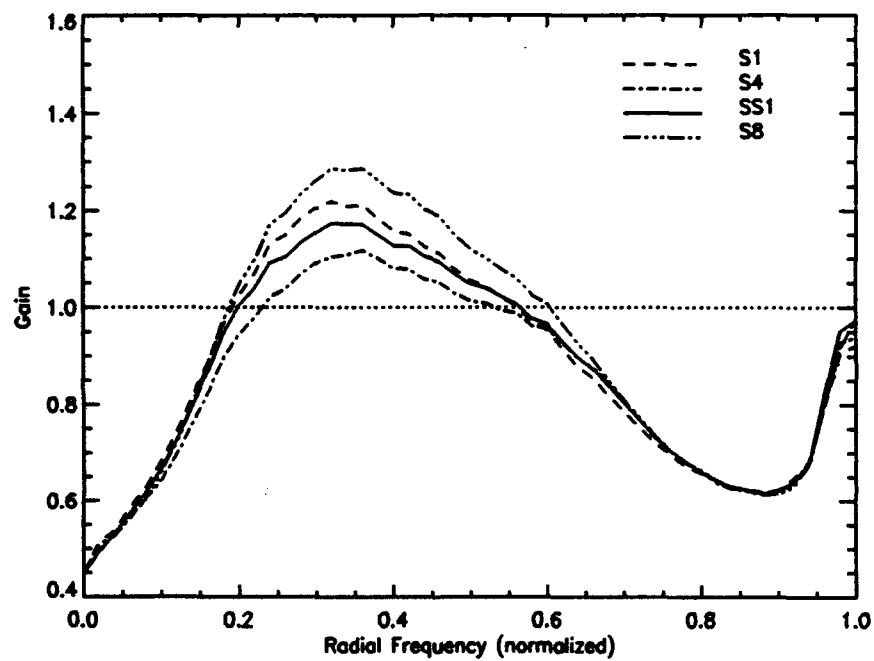


Figure B.47 Gain Curves, Experiment 5: Point source,  $r_o = 10\text{cm}$ ,  $m_v = +3$ ,  $\sigma^2 = 30$ , Selection rate = 20%

## Bibliography

1. AVCO Research Laboratory, Maui Operations. *AMOS User's Manual*. Technical Report AERLM 1176, Rev. 9, Griffiss AFB, NY 13441: Rome Air Development Center/OCSP, September 1990.
2. Biemond and others. "Iterative methods for image deblurring," *Proceedings of the IEEE*, 5:856-878 (May 1990).
3. Boyd, Robert W. *Radiometry and the Detection of Optical Radiation*. John Wiley and Sons, New York, 1983.
4. Cortegiani and others. "Probability of diffraction-limited images in infrared through turbulence - experimental results," *Proceedings of the ESO Conference on Scientific Importance of High Angular Resolution at Infrared and Optical Wavelengths, Garching*, 175-180 (March 1981).
5. Devaney and others. "Real-time image sharpening." *Diffraction-Limited Imaging with Very Large Telescopes* edited by Alloin and Mariotti, 369-378, Kluwer Academic Publishers, Dordrecht, The Netherlands, 1989.
6. Fogiel, M. *Numerical Analysis Problem Solver*. REA Publications, New York, 1983.
7. Fried, David L. "Statistics of a geometric representation of wavefront distortion," *Journal of the Optical Society of America*, 55(11):1427-1435 (November 1965).
8. Fried, David L. "Optical resolution through a randomly inhomogeneous medium for very long and very short exposures," *Journal of the Optical Society of America*, 56(10):1372-1379 (October 1966).
9. Fried, David L. "Probability of getting a lucky short-exposure image through turbulence," *Journal of the Optical Society of America*, 68(12):1651-1657 (December 1978).
10. Fuensalida and others. "Applications of image sharpening techniques," *Astronomy and Astrophysics*, 191:L13-L15 (1988).
11. Gonzalez and Woods. *Digital Image Processing*. Addison-Wesley Publishing Company, Reading, Massachusetts, 1992.
12. Goodman, Joseph W. *Introduction to Fourier Optics*. McGraw-Hill Book Company, San Francisco, 1968.
13. Goodman, Joseph W. *Statistical Optics*. Wiley-Interscience Publications, New York, 1985.
14. Hardy, John W. "Active optics: a new technology for the control of light," *Proceedings of the IEEE*, 66(6):651-697 (June 1978).

15. Hecht, Eugene. *Optics* (Second Edition). Addison-Wesley Publishing Company, Reading, Massachusetts, 1987.
16. Hequet and Coupinout. "Gain en resolution par superposition de poses courtes recentrees et selectionnees," *Journal of Optics (Paris)*, 16(1):21-26 (1985).
17. Idell and Webster. "Resolution limits for coherent optical imaging: signal-to-noise analysis in the spatial-frequency domain," *Journal of the Optical Society of America A*, 9(1):43-56 (1992).
18. James, M. L. *Applied Numerical Methods for Digital Computation* (Second Edition). Harper and Row, New York, 1977.
19. Labeyrie, A. "Attainment of diffraction limited resolution in large telescopes by fourier analyzing speckle patterns in star images," *Astronomy and Astrophysics*, 6:85-87 (1970).
20. Lathi, B. P. *Modern Digital and Analog Communication Systems*. Holt, Rinehart and Winston, New York, 1983.
21. Lohman and others. "Speckle masking in astronomy: triple correlation theory and applications," *Applied Optics*, 22(4):4028-4037 (December 1983).
22. Mahajan, Virenda N. "Strehl ratio for primary aberrations: some analytical results for circular and annular pupils," *Journal of the Optical Society of America*, 72(9):1258-1266 (September 1982).
23. Mannos and Sakrison. "The effects of a visual fidelity criterion on the encoding of images," *IEEE Transactions on Information Theory*, IT-20(4):525-536 (July 1974).
24. Marechal, A. "Etude des effets combines de la diffraction et des aberrations geometriques sur l'images d'un point lumineux," *Rev. d'Opt.*, 26:257-277 (1947).
25. Milton, A. F. "Charge transfer devices for infrared imaging." *Optical and Infrared Detectors* edited by R. J. Keyes, 197-228, Springer-Verlag, New York, 1977.
26. Muller and Buffington. "Real-time correction of atmospherically degraded telescope images through image sharpening," *Journal of the Optical Society of America*, 64(9):1200-1210 (September 1974).
27. Newton, Isaac. *Opticks*. Dover Publications, New York, 1952.
28. Nieto and others. "Photon-counting detectors in time-resolved imaging mode: image re-centering and selection algorithms," *Astronomy and Astrophysics*, 178:301-306 (1987).
29. Nill, Norman B. "A visual model weighted cosine transform for image compression and quality assessment," *IEEE Transactions on Communications*, COMM-33(6):551-557 (June 1985).
30. O'Neill, Edward L. *Introduction to Statistical Optics*. Addison-Wesley Publishing Company, Reading, Massachusetts, 1963.

31. Pierce, John R. *Symbols, Signals and Noise* (Second revised Edition). Dover Publications, New York, 1980.
32. Ridpath, Ian. *Universe Guide to Stars and Planets*. Universe Books, New York, 1984.
33. Roddier, F. "The effects of atmospheric turbulence in optical astronomy." *Progress in Optics 19*, edited by E. Wolf, 283-378, North-Holland-Amsterdam, 1981.
34. Roggeman and others. "Linear reconstruction of compensated images: theory and experimental results," *Applied Optics*, 31(35):7429-7441 (December 1992).
35. Roggeman and Matson. "Power spectrum and fourier phase spectrum estimation by using fully and partially compensating adaptive optics and bispectrum postprocessing," *Journal of the Optical Society of America A*, 19(9):1525-1535 (September 1992).
36. Roggeman and Meinhardt. "Image reconstruction by means of wavefront sensor measurements in closed-loop adaptive optics systems," *Journal of the Optical Society of America A*, 10(9):1996-2007 (September 1993).
37. Roggeman, Michael C. "Limited degree-of-freedom adaptive optics and image reconstruction," *Applied Optics*, 30(29):4227-4233 (October 1991).
38. Seyrafi and Hovanessian. *Introduction to Electro-Optical Imaging and Tracking Systems*. Artech House, Norwood, Massachusetts, 1993.
39. Wagner, Richard E. "Post-processing of imagery from active optics - some pitfalls." *Imaging Through the Atmosphere 75*, edited by James E. Wyant, 136-140, SPIE, Palos Verdes Estates, California, 1976.
40. Welsh and Gardner. "Performance analysis of adaptive-optics systems using laser guide stars and slope sensors," *Journal of the Optical Society of America A*, 6(12):1913-1923 (December 1989).

## *Vita*

Captain Craig A. Stoudt was born in Pottstown, Pennsylvania on September 20th, 1956. In 1974 he graduated from Sterling Regional High School in Somerdale, New Jersey, and then attended Temple University in Philadelphia, Pennsylvania from 1974 to 1976. In 1976 he enlisted in the United States Air Force. After graduating from the Basic Military Training School at Lackland Air Force Base, Texas, he was assigned duties as a medical laboratory technician. In 1982 Staff Sergeant Stoudt was selected to pursue a Bachelor of Science Degree in Electrical Engineering at New Mexico State University, Las Cruces, New Mexico, under the Airman Education and Commissioning Program. Upon graduation, he returned to Lackland Air Force Base to attend Officer Training School, where he received his commission in August of 1985. Second Lieutenant Stoudt then served as a supercomputer communications analyst at the Air Force Weapons Laboratory, Kirtland Air Force Base, New Mexico. In 1988 First Lieutenant Stoudt was reassigned to the 1843d Engineering Installation Group at Wheeler Air Force Base, Hawaii, where he served as a radio systems engineer. In May of 1992 Captain Stoudt was reassigned to the Air Force Institute of Technology to pursue a Master of Science Degree in Electrical Engineering, with a specialty in Electro-Optics. In January of 1994 Capt Stoudt reports to the 84th Radar Evaluation Squadron, Hill Air Force Base, Utah, where he will serve as a radar systems engineer.

Permanent address: 160 Cedarcroft Avenue  
Audubon, New Jersey 08103

# REPORT DOCUMENTATION PAGE

Form Approved  
OMB No. 0704-0188

Public reporting burden for this collection of information is estimated to average 1 hour per response, including the time for reviewing instructions, searching existing data sources, gathering and maintaining the data needed, and completing and reviewing the collection of information. Send comments regarding this burden estimate or any aspect of this collection of information, including suggestions for reducing this burden, to Washington Headquarters Service, Directorate for Information Operations and Reports, 1215 Jefferson Davis Highway, Suite 1204, Arlington, VA 22202-4302, and to the Office of Management and Budget, Paperwork Reduction Project (0704-0188), Washington, DC 20503.

<b>1. AGENCY USE ONLY (Leave blank)</b>		<b>2. REPORT DATE</b> December 1993	<b>3. REPORT TYPE AND DATES COVERED</b> Master's Thesis	
<b>4. TITLE AND SUBTITLE</b> Improved quality of reconstructed images through sifting of data in statistical image reconstruction			<b>5. FUNDING NUMBERS</b>	
<b>6. AUTHOR(S)</b> Craig A. Stoudt, Capt, USAF				
<b>7. PERFORMING ORGANIZATION NAME(S) AND ADDRESS(ES)</b> Air Force Institute of Technology, WPAFB OH 45433-6583			<b>8. PERFORMING ORGANIZATION REPORT NUMBER</b> AFIT/GEO/ENP/93D-03	
<b>9. SPONSORING/MONITORING AGENCY NAME(S) AND ADDRESS(ES)</b> Capt Andy Suzuki PL/LIMA, 535 Lipoa Pkwy, Suite 200 Kihei, HI 96753			<b>10. SPONSORING/MONITORING AGENCY REPORT NUMBER</b>	
<b>11. SUPPLEMENTARY NOTES</b>				
<b>12a. DISTRIBUTION/AVAILABILITY STATEMENT</b> Approved for Public Release; Distribution Unlimited			<b>12b. DISTRIBUTION CODE</b>	
<b>13. ABSTRACT (Maximum 200 words)</b>  <p style="text-align: center;"><b>Abstract</b></p> <p>The U.S. Air Force employs adaptive optics systems to produce images of exo-atmospheric objects. Typically, a large set of short exposure images are collected, re-centered to compensate for random image motion, averaged together to improve the signal to noise ratio, and then processed to form a reconstructed image. It is known that some short exposure images will be better than others, so some researchers have suggested that image quality can be improved by selecting a subset of the short exposure images according to some quality criterion, and then processing the average of this subset to form a single, high quality image. This thesis investigates the statistical implications of using frame selection as a post-processing technique to enhance images of exo-atmospheric objects measured by Air Force adaptive optics systems. The results demonstrate that frame selection narrows the optical system point spread function, which reduces image blurring, and increases the frequency spectrum signal to noise ratio, particularly in the mid-frequency range. For extended objects, the technique is light level dependent: for a 1 meter adaptive optics telescope, frame selection will yield an increase in signal to noise ratio for objects brighter than visual magnitude +2.3.</p>				
<b>14. SUBJECT TERMS</b> Frame Selection, Adaptive Optics, Image Processing			<b>15. NUMBER OF PAGES</b> 146	
			<b>16. PRICE CODE</b>	
<b>17. SECURITY CLASSIFICATION OF REPORT</b> UNCLASSIFIED	<b>18. SECURITY CLASSIFICATION OF THIS PAGE</b> UNCLASSIFIED	<b>19. SECURITY CLASSIFICATION OF ABSTRACT</b> UNCLASSIFIED	<b>20. LIMITATION OF ABSTRACT</b> UL	